CAPITAL UNIVERSITY OF SCIENCE AND TECHNOLOGY, ISLAMABAD

Nonlinear Electro-Magneto Marangoni Transport in Hybrid Nanofluid Flow with Relaxation and Reactive Effects

by

Aimen Qadir

A thesis submitted in partial fulfillment for the degree of Master of Philosophy

in the

Faculty of Computing
Department of Mathematics

2026

CERTIFICATE OF APPROVAL

Nonlinear Electro-Magneto Marangoni Transport in Hybrid Nanofluid Flow with Relaxation and Reactive Effects

by

Aimen Qadir

MMT241002

THESIS EXAMINING COMMITTEE

S. No.	Examiner	Name	Organization
(a)	External Examiner	Dr. Nabeela Kousar	AU, Islamabad
(b)	Internal Examiner	Dr. Sabeel Khan	CUST, Islamabad

Dr. Muhammad Sagheer
Thesis Supervisor
April, 2026

Dr. Muhammad Sagheer
Head
Dept. of Mathematics
April, 2026

Dr. M. Abdul Qadir
Dean
Faculty of Computing
April, 2026

Author's Declaration

I, **Aimen Qadir** hereby state that my MPhil thesis titled "**Nonlinear Electro-Magneto Marangoni Transport in Hybrid Nanofluid Flow with Relaxation and Reactive Effects**" is my own work and has not been submitted previously by me for taking any degree from Capital University of Science and Technology, Islamabad or anywhere else in the country/abroad.

At any time if my statement is found to be incorrect even after my graduation, the University has the right to withdraw my MPhil Degree.

Aimen Qadir

Registration No: MMT241002

Plagiarism Undertaking

I solemnly declare that research work presented in this thesis titled "**Nonlinear Electro-Magneto Marangoni Transport in Hybrid Nanofluid Flow with Relaxation and Reactive Effects**" is solely my research work with no significant contribution from any other person. Small contribution/help wherever taken has been duly acknowledged and that complete thesis has been written by me.

I understand the zero tolerance policy of the HEC and Capital University of Science and Technology towards plagiarism. Therefore, I as an author of the above titled thesis declare that no portion of my thesis has been plagiarized and any material used as reference is properly referred/cited.

I undertake that if I am found guilty of any formal plagiarism in the above titled thesis even after award of MPhil Degree, the University reserves the right to withdraw/revoke my MPhil degree and that HEC and the University have the right to publish my name on the HEC/University website on which names of students are placed who submitted plagiarized work.

Aimen Qadir

Registration No:MMT241002

Acknowledgement

In the name of Allah, the Most Gracious and the Most Merciful.

I would like to sincerely thank my supervisor, **Dr. Muhammad Sagheer**, for his guidance, support and encouragement throughout this research. His helpful advice and valuable suggestions made this work possible. I am truly grateful for his patience and for always guiding me in the right direction during this academic journey.

I am deeply thankful to my parents, **Abdul Qadir** and **Riffat Qadir**, for their endless prayers, love and sacrifices. Their belief in me has always given me strength and confidence. Whatever I have achieved today is because of their support and the values they taught me.

I also express my heartfelt appreciation to my sister **Anum Qadir** for always standing by my side with patience, understanding, and constant support. I am equally grateful to my dear friend **Sana Bibi**, whose motivation, positivity, and constant reassurance helped me stay focused and determined during the most challenging phases of this journey. Lastly, I sincerely appreciate my long-distance best friends, **Fatima Sehar** and **Hamna Aziz**, whose emotional support, sincere advice and constant availability brought me comfort and strength during difficult moments. Their encouragement and presence, even across distances, have meant more to me than I can truly express.

Abstract

Numerical investigation is conducted to examine Marangoni convective transport in hybrid nanofluids flowing over a permeable surface. The study explores the coupled behavior of momentum, heat and mass transfer under progressively enhanced physical conditions. The analysis begins with magnetic field effects and is subsequently extended to include an applied electric field, followed by the incorporation of non-inertial porous resistance and higher-order chemical reaction mechanisms. The governing boundary-layer equations incorporate thermal and solutal relaxation effects that account for finite heat and mass propagation. Using similarity transformations, the equations are reduced to ordinary differential form and solved numerically via a shooting method involving a fourth-order Runge–Kutta scheme in MATLAB. The impacts of electromagnetic forces, porous resistance, thermophoresis, Brownian motion, internal heat generation, Lewis and Prandtl numbers, activation energy and higher-order chemical reaction on velocity, temperature, and concentration fields are examined. The results indicate that electromagnetic forces significantly modify near-wall flow behavior, while higher-order chemical reactions and porous resistance strongly enhance mass transfer responses. Furthermore, the hybrid nanofluid exhibits greater sensitivity to combined transport mechanisms compared to the nanofluid. These findings deepen the understanding of Marangoni-driven hybrid nanofluid transport and offer useful guidance for the design of efficient thermal and reactive flow systems.

Contents

List of Figures

List of Tables

Abbreviations

BCs	Boundary conditions
HNF	Hybrid Nano Fluid
IVPs	Initial value problem
MHD	Magnetohydrodynamics
NF	Nano Fluid
ODEs	Ordinary differential equation
PDEs	Partial differential equation
RK-4	Range kutta order 4

Symbols

u, v	Velocity components
η	Similarity variable
T	Temperature
T_w	Wall temperature
T_∞	Ambient temperature
B_0	Magnetic field strebgth
E_0	Electric field strength
$\widetilde{\mu}$	Viscosity
$\widetilde{\sigma}$	Electrical conductivity
$\widetilde{K}$	Thermal conductivity
$\widetilde{\rho}\widetilde{C}_p$	Heat capacity
C	Concentration
C_w	Surface concentration
C_∞	Ambient concentration
k	Permeability
k^*	Absorption coefficient
q_r	Radiative heat flux
σ^*	Stefan Boltzmann constant
Λ_1	Relaxiation time constant
Λ_2	Solute time constant
e	Activation energy coefficient
M	Magnetic field parameter
E	Electric field parameter

K_1	Porosity paramter
Pr	Prandtl number
R	Radiation parameter
q	Heat source
D_B	Brownian motion
D_T	Thermophoresis motion
Nb	Brownian motion parameter
Nt	Thermophoresis motion parameter
Le	Lewis number
Γ	Chemical reaction parameter
δ	Thermal relaxation parameter
β	Solute time relaxation parameter
Q	Heat source parameter
ω	Non-Darcy flow coefficient
α	Temperature difference parameter
ε	Activation energy parameter
m	Fitted rate constant
F	Non-Darcy flow parameter
Nu_x	Local Nusselt number
Sh_x	Local Sherwood number
f(η)	Dimensionless velocity
$\theta(\eta)$	Dimensionless temperature
$\theta(\phi)$	Dimensionless concentration

Subscripts

p	Nanoparticle
nf	Nanofluid
hnf	Hybrid nanofluid

Chapter 1

Introduction

This chapter presents the background and context of the research problem. It highlights the central themes of the study and offers a brief summary of the framework of the thesis.

1.1 Background

Fluid flow and the transfer of heat and mass [1] are important in many engineering and scientific applications, such as energy systems, chemical processes, environmental technologies and biomedical devices. Understanding how fluids move and transfer heat and mass is essential for predicting system behavior and improving design performance.

Nanofluids were introduced to improve the thermal performance of conventional heat transfer fluids by suspending nanosized solid particles in a base liquid.

Numerous studies have shown that the presence of nanoparticles enhances thermal conductivity and convective heat transfer, mainly due to improved energy exchange and increased interaction between the fluid and solid phases [2–4].

Experimental and numerical investigations by Hayat et al. [5] further examined heat and flow characteristics of nanofluids containing carbon nanotubes, highlighting their superior thermal performance in comparison to conventional fluids.

In a related study, Karim et al. [6] carried out numerical simulations to explore nanofluid flow behavior over permeable geometries, demonstrating the strong influence of surface conditions and transport parameters on heat transfer rates.

Hybrid nanofluids were introduced as an advancement over conventional nanofluids by dispersing two or more different types of nanoparticles within a base fluid, with the aim of achieving superior thermal and transport performance. Early investigations by Suresh et al. [7] demonstrated that hybrid nanofluids exhibit higher thermal conductivity than single-component nanofluids due to combined effects of different nanoparticles. Devi and Devi [8] further showed that hybrid nanofluids significantly enhance convective heat transfer rates while maintaining acceptable flow stability.

More recent investigations demonstrate that hybrid nanofluids provide improved thermal transport and flow control in channels and stretching geometries, particularly under electromagnetic effects, making them suitable for advanced thermal systems [9–11]. Comprehensive reviews further confirm that the combined use of different nanoparticles enhances thermo-physical properties and expands the practical applicability of hybrid nanofluids in modern engineering applications [12].

Marangoni convection has been widely examined due to its strong influence on boundary layer flow and heat transfer induced by surface tension gradients. Christopher and Wang [13] investigated the role of the Prandtl number in Marangoni convection over a flat surface and showed that thermal diffusion plays a key role in shaping the temperature field. Early analytical investigations by Magyari and Chamkha [14] provided exact solutions for thermosolutal magnetohydrodynamic (MHD) Marangoni boundary layers, highlighting the strong coupling between magnetic forces and surface-tension-driven flow. Their work demonstrated that magnetic fields significantly modify velocity and thermal distributions by introducing Lorentz forces that oppose fluid motion.

Subsequent works incorporated thermal radiation and porous media into Marangoni convection models, with Al-Mdallal et al. [15] showing that radiation and magnetic inclination strongly affect heat transfer in hybrid nanofluids, while Aly and Ebaid [16] demonstrated that porous resistance critically controls MHD Marangoni transport under radiative conditions. Kalpana et al. [17] numerically analyzed Marangoni convective flow of two-phase MHD dusty nanofluids, showing that Brownian motion and thermophoresis significantly influence velocity, temperature and concentration fields. The flow and thermal behavior become strongly coupled, as random particle diffusion and thermally induced migration substantially modify both temperature and concentration fields. Brownian motion enhances energy transport through intensified particle collisions, whereas thermophoresis drives nanoparticles away from heated surfaces, thereby influencing thermal and solutal boundary layers [18, 19].

Most heat transfer studies are based on Fourier's law, but this approach assumes that heat travels instantly through a fluid, which is not always realistic. To overcome this limitation, the Cattaneo–Christov heat flux model was introduced to include thermal relaxation effects and provide a more accurate description of heat transport. Using this model, Khan et al. [20] numerically studied viscoelastic flow over an exponentially stretching surface and reported clear differences compared to classical Fourier-based results. In the context of Marangoni-driven nanofluid flows, Alharbi et al. [21] applied the Cattaneo–Christov heat flux model to investigate copper–water nanofluid heat transfer under slip conditions. Consequently, the Cattaneo–Christov heat flux model has been widely studied in MHD flows, hybrid nanofluids, and convective boundary conditions, demonstrating its broad applicability [22–24].

Chemical reaction effects have been widely incorporated into fluid flow models to control and enhance concentration distributions in heat and mass transfer processes. First-order reactions are commonly used to represent simple kinetics, leading to a reduction in concentration boundary layer thickness [25]. Hussain et al. [26] analyzed the effects of first-order chemical reaction and melting heat on hybrid nanofluid flow over a nonlinear curved stretching surface, considering shape factor influences. To describe more realistic behavior, higher-order chemical reactions

have also been introduced, capturing nonlinear kinetics and stronger coupling between concentration, flow and temperature fields. Mishra et al. [27] showed that chemical reaction and bio-active mixing strongly affect heat and mass transfer in hybrid nanofluid jet flow. These reactions significantly influence mass transfer rates and concentration profiles, particularly in nanofluid and MHD flows where diffusion, convection, and reaction mechanisms coexist [28, 29].

Despite significant progress in the study of nanofluid and hybrid nanofluid transport, a unified treatment of Marangoni convection coupled with electromagnetic forces, porous resistance, and reaction effects remains limited. Much of the existing work addresses these mechanisms independently, leaving their combined influence insufficiently explored. In response, this research presents a structured investigation of Al_2O_3 nanofluid and Cu-Al_2O_3 hybrid nanofluid systems by sequentially examining magnetic-field effects, extending to electric–magnetic interactions and finally incorporating non-inertial porous resistance and higher-order chemical reactions. The governing nonlinear boundary-layer equations are solved using an efficient numerical strategy based on the shooting method. Through this layered modeling approach, the study clarifies the coupled roles of momentum, thermal and concentration transport in surface-driven nanofluid flows. The results offer valuable physical insight and support the development of improved models for advanced thermal, electromagnetic and reactive flow applications.

1.2 Thesis Structure

The thesis is presented across five chapters to describe the work carried out.

Chapter 1 provides an overview of the research area and the motivation for the the work. It reviews previous studies related to nanofluids, hybrid nanofluids, Marangoni convection, electromagnetic effects, porous media, and chemical reaction mechanisms. The chapter also highlights the limitations of existing research and defines the objectives of the present study.

Chapter 2 investigates Marangoni-driven flow and heat transfer in a Cu-Al_2O_3 hybrid nanofluid across a permeable surface under the influence of a magnetic field. The model equations are established under relevant physical assumptions and expressed in dimensionless form using similarity variables. Numerical solutions are obtained using the shooting method based on a fourth-order Runge–Kutta scheme and the effects of key parameters on velocity and temperature profiles are discussed.

Chapter 3 builds upon the model developed in Chapter 2 by introducing additional heat and mass transport mechanisms. These include internal heat generation, Brownian motion, thermophoresis and the Cattaneo–Christov heat transport model A concentration equation is incorporated to examine mass transfer alongside thermal transport. The role of these mechanisms in shaping temperature and concentration distributions is analyzed, while surface heat and mass transfer characteristics are assessed using the Nusselt and Sherwood numbers.

Chapter 4 further extends the analysis by incorporating an applied electric field together with non-inertial porous resistance and higher-order chemical reaction effects. This chapter examines the simultaneous action of electric and magnetic fields on Marangoni-driven nanofluid and hybrid nanofluid flow, providing a deeper understanding of coupled electromagnetic transport mechanisms. Additional physical effects, including Darcy–Forchheimer porous resistance, Brownian motion and thermophoresis, are incorporated to capture realistic momentum, heat and mass transfer behavior. A comparative analysis is performed to examine the effects of the added mechanisms on flow behavior and surface transport rates.

Chapter 5 summarizes the main results of the thesis and discusses the key physical ical insights obtained from the numerical study.

The bibliography contains the full details of all references cited throughout this thesis.

Chapter 2

Numerical Investigation of Marangoni Convection in Hybrid Nanofluid Flow over a Permeable Surface

2.1 Introduction

A numerical analysis of Marangoni convection in a Cu–Al_2O_3/kerosene-oil hybrid nanofluid flowing along a permeable surface is carried out. The flow dynamics are has been assumed to be influenced by magnetic effects, a porous medium and radiative heat transfer. To carry out the analysis, the governing nonlinear partial differential equations are transformed into a system of dimensionless ordinary differential equations by applying appropriate transformations.

Numerical results are derived using the Runge–Kutta based shooting method, which helps us analyze how various key parameters affect the velocity and temperature distributions. This chapter offers a comprehensive explanation of the key findings and their significance on hybrid-nanofluid heat transfer, as described in Kumar et al. [30].

2.2 Physical Model

Consider a two-dimensional, laminar, steady, and incompressible Marangoni convective fluid flow over a permeable surface. The working fluid is modeled as a hybrid nanofluid consisting of copper and aluminum oxide ($Cu–Al_2O_3$) nanoparticles dispersed in kerosene oil. The coordinate system is defined such that the x-direction aligns with the flow, while the y-direction is taken perpendicular to the surface. A uniform magnetic field of intensity B_0 is applied in the y-direction. Furthermore, the effect of radiative heat transfer is incorporated through the radiative heat flux q_r. The surface tension is assumed to vary linearly with temperature and is represented as $\sigma = \sigma_0 - \gamma(T - T_\infty)$, where σ is the surface tension, σ_0 is the reference surface tension at temperature T_∞, and γ represents the surface tension gradient. This temperature-dependent variation in surface tension gives rise to Marangoni stresses along the surface, which drive the flow. The surface temperature is prescribed as $T_w = T_\infty + bx^2$, where T_w denotes the wall temperature and T_∞ represents the ambient fluid temperature. The governing equations of the present model are expressed in (2.1)–(2.3), while the boundary conditions are specified in (2.4).

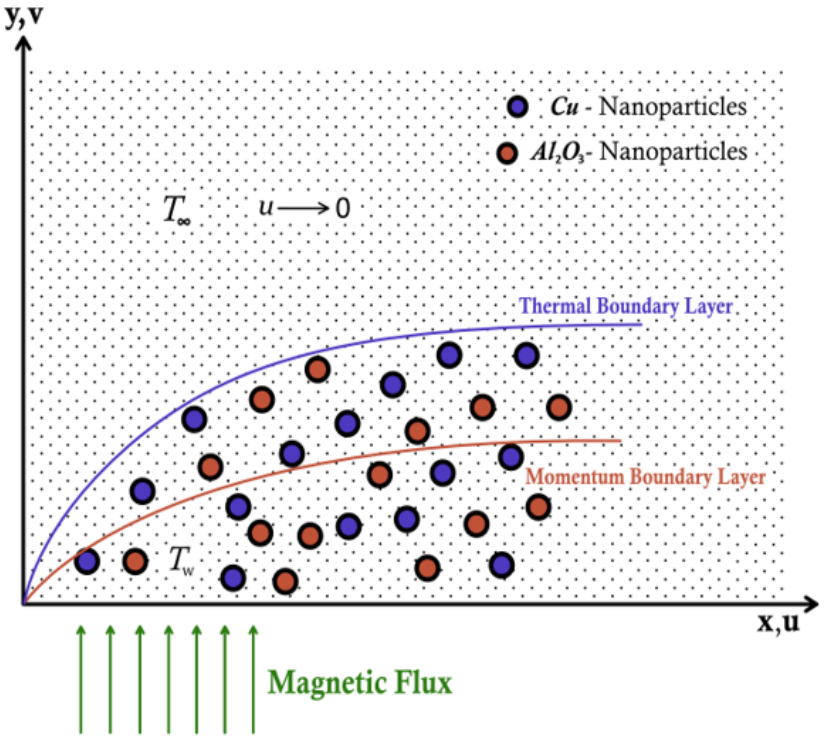

FIGURE 2.1: Physical representation of hybrid nanofluid flow

2.2.1 Mass Conservation

$$\frac{\partial \mathrm{u}}{\partial \mathrm{x}} + \frac{\partial \mathrm{v}}{\partial \mathrm{y}} = 0. \tag{2.1}$$

2.2.2 Momentum Equation

$$\mathrm{u}\frac{\partial \mathrm{u}}{\partial \mathrm{x}} + \mathrm{v}\frac{\partial \mathrm{u}}{\partial \mathrm{y}} + \frac{\widetilde{\sigma}_{hnf} B_0^2}{\widetilde{\rho}_{hnf}}\,\mathrm{u} + \frac{\widetilde{\mu}_{hnf}}{\widetilde{\rho}_{hnf}}\frac{\mathrm{u}}{k} = \frac{\widetilde{\mu}_{hnf}}{\widetilde{\rho}_{hnf}}\frac{\partial^2 \mathrm{u}}{\partial \mathrm{y}^2}. \tag{2.2}$$

2.2.3 Energy Equation

$$\mathrm{u}\frac{\partial \mathrm{T}}{\partial \mathrm{x}} + \mathrm{v}\frac{\partial \mathrm{T}}{\partial \mathrm{y}} + \frac{1}{(\widetilde{\rho C_p})_{hnf}}\left(\frac{\partial q_r}{\partial \mathrm{y}}\right) = \frac{\widetilde{K}_{hnf}}{(\widetilde{\rho C_p})_{hnf}}\frac{\partial^2 \mathrm{T}}{\partial \mathrm{y}^2}. \tag{2.3}$$

2.2.4 Boundary Conditions

$$\left.\begin{array}{lll} \mathrm{v} = \mathrm{v}_w, & \widetilde{\mu}_{hnf}\left(\dfrac{\partial \mathrm{u}}{\partial \mathrm{y}}\right) = \dfrac{\partial \sigma}{\partial \mathrm{T}}\dfrac{\partial \mathrm{T}}{\partial \mathrm{x}}, \quad \mathrm{T} = \mathrm{T}_\infty + b\mathrm{x}^2, & \text{at } \mathrm{y} = 0, \\ \mathrm{T} \to \mathrm{T}_\infty, & \mathrm{u} \to 0 \quad \text{as } \mathrm{y} \to \infty. & \end{array}\right\} \tag{2.4}$$

2.2.5 Formulation and Thermo-physical Characteristics

The thermo-physical parameters of both the HNF and NF are presented in Table 2.1 to facilitate an informative comparison.

TABLE 2.1: Thermo-physical values of kerosene oil and nanoparticles

Physical Properties	**Al_2O_3**	**Cu**	**Kerosene Oil**
$\widetilde{\rho}\left(\mathrm{kg/m^{-3}}\right)$	3970	8933	783
$\widetilde{C}_p\left(\mathrm{J/kg\,K}\right)$	765	385	2090
$\widetilde{K}\left(\mathrm{W/mK}\right)$	40	401	0.145
$\widetilde{\sigma}\left(\mathrm{s/m}\right)$	35×10^6	59.6×10^6	6×10^{-10}

2.3 Similarity Transformation and Non- dimensionalization of Mathematical Model

In this section, we present the non-dimensionalization process of the mathematical model that describe the behavior of our hybrid nanofluid. This approach involves the introduction of appropriate dimensionless variables and transformation parameters in order to reduce the complexity of the governing equations. By expressing the model in a dimensionless framework, the resulting analysis becomes easier to understand and interpret.

The system of equations is reduced to ODEs using the following similarity transformations:

$$\left.\begin{aligned} &\eta = \psi_1 \mathrm{y}, \qquad \xi = \psi_2 \mathrm{x}\, \mathrm{f}(\eta), \qquad \theta(\eta) = \frac{\mathrm{T}-\mathrm{T}_\infty}{\mathrm{T}_w - \mathrm{T}_\infty}, \qquad \mathrm{u} = \frac{\partial \xi}{\partial \mathrm{y}}, \\ &\psi_1 = \left(\frac{\gamma_0 \gamma b \widetilde{\rho}_f}{\widetilde{\mu}_f^2}\right)^{1/3}, \qquad \psi_2 = \left(\frac{\gamma_0 \gamma b \widetilde{\mu}_f}{\widetilde{\rho}_f^2}\right)^{1/3}, \qquad \mathrm{v} = -\frac{\partial \xi}{\partial \mathrm{y}}. \end{aligned}\right\} \tag{2.5}$$

The following derivatives are required in order to satisfy the mass conservation (2.1).

$$\begin{aligned} \mathrm{u} &= \frac{\partial \xi}{\partial \mathrm{y}} \\ &= \psi_2 \mathrm{x}\, \mathrm{f}'(\eta)\, \frac{\partial \eta}{\partial \mathrm{y}} \\ &= \psi_1 \psi_2 \mathrm{x}\, \mathrm{f}'(\eta). \end{aligned} \tag{2.6}$$

$$\begin{aligned} \mathrm{v} &= \frac{\partial \xi}{\partial \mathrm{x}} \\ &= -\psi_2 \mathrm{f}(\eta). \end{aligned} \tag{2.7}$$

$$\begin{aligned} \frac{\partial \mathrm{u}}{\partial \mathrm{x}} &= \frac{\partial}{\partial \mathrm{x}}\big(\psi_1 \psi_2 \mathrm{x}\, \mathrm{f}'(\eta)\big) \\ &= \psi_1 \psi_2 \mathrm{f}'(\eta). \end{aligned} \tag{2.8}$$

$$\begin{aligned} \frac{\partial \mathrm{v}}{\partial \mathrm{y}} &= \frac{\partial}{\partial \mathrm{y}}\big(-\psi_2\, \mathrm{f}(\eta)\big) \\ &= -\psi_1 \psi_2\, \mathrm{f}'(\eta). \end{aligned} \tag{2.9}$$

Using (2.8) and (2.9) in (2.1), we get:

$$\frac{\partial \mathrm{u}}{\partial \mathrm{x}} + \frac{\partial \mathrm{v}}{\partial \mathrm{y}} = \psi_1\psi_2 \mathrm{f}'(\eta) - \psi_1\psi_2 \mathrm{f}'(\eta)$$
$$= 0.$$

Therefore, (2.1) is satisfied identically.

Based on the literature reviewed, the thermophysical parameters of the hybrid nanofluids are provided in Table 2.2.

TABLE 2.2: Thermo-physical properties of hybridnanofluids [30].

Properties	**Hybrid Nanofluid**
Dynamic viscosity	$\widetilde{\mu}_{nf} = \frac{\widetilde{\mu}_f}{(1-\Phi_1)^{2.5}(1-\Phi_2)^{2.5}}$
Heat capacitance	$\frac{(\widetilde{\rho C}_p)_{hnf}}{(\widetilde{\rho C}_p)_f} = (1-\Phi_2)\big((1-\Phi_1) + \Phi_1\frac{(\widetilde{\rho C}_p)_{s_1}}{(\widetilde{\rho C}_p)_f}\big) + \Phi_2\frac{(\widetilde{\rho C}_p)_{s_2}}{(\widetilde{\rho C}_p)_f}$
Density	$\widetilde{\rho}_{hnf} = \widetilde{\rho}_f(1-\Phi_2)\big((1-\Phi_1) + \Phi_1(\frac{\widetilde{\rho}_{s_1}}{\widetilde{\rho}_f})\big) + \Phi_2\widetilde{\rho}_{s_2}$
Thermal conductivity	$\widetilde{K}_{hnf} = \widetilde{K}_{nf}\left[\frac{\widetilde{K}_{s_2}+(n-1)\widetilde{K}_{nf}-(n-1)\Phi_2(\widetilde{K}_{nf}-\widetilde{K}_{s_2})}{\widetilde{K}_{s_2}+(n-1)\widetilde{K}_{nf}+\Phi_2(\widetilde{K}_{nf}-\widetilde{K}_{s_2})}\right]$
	$\widetilde{K}_{nf} = \widetilde{K}_f\left[\frac{\widetilde{K}_{s_1}+(n-1)\widetilde{K}_f-(n-1)\Phi_1(\widetilde{K}_f-\widetilde{K}_{s_1})}{\widetilde{K}_{s_1}+(n-1)\widetilde{K}_f+\Phi_1(\widetilde{K}_f-\widetilde{K}_{s_1})}\right]$
Electrical conductivity	$\widetilde{\sigma}_{hnf} = \widetilde{\sigma}_{nf}\left[\frac{\widetilde{\sigma}_{s_2}(1+2\Phi_2)+2\widetilde{\sigma}_{bf}(1-\Phi_2)}{\widetilde{\sigma}_{s_2}(1-\Phi_2)+\widetilde{\sigma}_{bf}(2+\Phi_2)}\right]$
	with $\widetilde{\sigma}_{nf} = \widetilde{\sigma}_f\left[\frac{\widetilde{\sigma}_{s_1}(1+2\Phi_1)+2\widetilde{\sigma}_f(1-\Phi_1)}{\widetilde{\sigma}_{s_1}(1-\Phi_1)+\widetilde{\sigma}_f(2+\Phi_1)}\right]$

To simplify the non-dimensionalization process, the following expressions including the thermophysical parameters are represented by $P_i\,(i = 1, 2, 3, 4, 5)$.

$$P_1 = \frac{\widetilde{\mu}_{hnf}}{\widetilde{\mu}_f}, \quad P_2 = \frac{\widetilde{\rho}_{hnf}}{\widetilde{\rho}_f}, \quad P_3 = \frac{\widetilde{K}_{hnf}}{\widetilde{K}_f},$$

$$P_4 = \frac{\widetilde{\sigma}_{hnf}}{\widetilde{\sigma}_f}, \quad P_5 = \frac{(\widetilde{\rho c}_p)_{hnf}}{(\widetilde{\rho c}_p)_f}.$$

2.3.1 Non-dimensionalization of Momentum Equation

The derivatives needed for the dimensionless formulation of the governing momentum equation (2.2), are given below:

$$\frac{\partial \mathrm{u}}{\partial \mathrm{y}} = \psi_1^2 \psi_2 \mathrm{x}\, \mathrm{f}''(\eta). \tag{2.10}$$

$$\Rightarrow \quad \frac{\partial^2 \mathrm{u}}{\partial \mathrm{y}^2} = \psi_1^3 \psi_2 \mathrm{x}\, \mathrm{f}'''(\eta). \tag{2.11}$$

Substituting the results of equations (2.6), (2.7), (2.8), (2.10), and (2.11) into the momentum equation (2.2), it yields the following form.

$$(\psi_1\psi_2 \mathrm{x}\, \mathrm{f}')(\psi_1\psi_2 \mathrm{f}') + (-\psi_2 \mathrm{f})(\psi_1^2\psi_2 \mathrm{x}\, \mathrm{f}'') + \frac{\widetilde{\sigma}_{hnf} B_0^2}{\widetilde{\rho}_{hnf}} \psi_1\psi_2 x\, \mathrm{f}' + \frac{\widetilde{\mu}_{hnf}}{\widetilde{\rho}_{hnf}} \frac{\psi_1\psi_2 \mathrm{x}\, \mathrm{f}'}{k} = \frac{\widetilde{\mu}_{hnf}}{\widetilde{\rho}_{hnf}} \psi_1^3 \psi_2 \mathrm{x}\, \mathrm{f}'''.$$

$$\Rightarrow \quad \psi_1^2\psi_2^2 \mathrm{x}\, \mathrm{f}'^2 - \psi_1^2\psi_2^2 \mathrm{x}\, \mathrm{f}\, \mathrm{f}'' + \frac{\widetilde{\sigma}_{hnf} B_0^2}{\widetilde{\rho}_{hnf}} \psi_1\psi_2 \mathrm{x}\, \mathrm{f}' + \frac{\widetilde{\mu}_{hnf}}{\widetilde{\rho}_{hnf}} \frac{\psi_1\psi_2 \mathrm{x}\, \mathrm{f}'}{k} = \frac{\widetilde{\mu}_{hnf}}{\widetilde{\rho}_{hnf}} \psi_1^3 \psi_2 \mathrm{x}\, \mathrm{f}'''.$$

$$\Rightarrow \quad \psi_1^2\psi_2^2 \mathrm{x}\, (\mathrm{f}'^2 - \mathrm{f}\, \mathrm{f}'') = \frac{\widetilde{\mu}_{hnf}}{\widetilde{\rho}_{hnf}} \psi_1^3 \psi_2 \mathrm{x}\, \mathrm{f}''' - \frac{\widetilde{\sigma}_{hnf} B_0^2}{\widetilde{\rho}_{hnf}} \psi_1\psi_2 \mathrm{x}\, \mathrm{f}' - \frac{\widetilde{\mu}_{hnf}}{\widetilde{\rho}_{hnf}} \frac{\psi_1\psi_2 \mathrm{x}\, \mathrm{f}'}{k}.$$

$$\Rightarrow \quad \mathrm{f}'^2 - \mathrm{f}\, \mathrm{f}'' = \frac{\widetilde{\mu}_{hnf}}{\widetilde{\rho}_{hnf}} \frac{\psi_1}{\psi_2} \mathrm{f}''' - \frac{\widetilde{\sigma}_{hnf} B_0^2}{\widetilde{\rho}_{hnf}} \frac{\mathrm{f}'}{\psi_1\psi_2} - \frac{\widetilde{\mu}_{hnf}}{\widetilde{\rho}_{hnf}} \frac{\mathrm{f}'}{\psi_1\psi_2 k}.$$

$$\Rightarrow \quad \mathrm{f}'^2 - \mathrm{f}\, \mathrm{f}'' = \frac{\widetilde{\mu}_{hnf}/\widetilde{\mu}_f}{\widetilde{\rho}_{hnf}/\widetilde{\rho}_f} \mathrm{f}''' - \frac{\widetilde{\sigma}_{hnf}/\widetilde{\sigma}_f}{\widetilde{\rho}_{hnf}\widetilde{\rho}_f} \frac{\widetilde{\sigma}_f}{\widetilde{\rho}_f} \frac{B_0^2}{\psi_1\psi_2} \mathrm{f}' - \frac{\widetilde{\mu}_{hnf}/\widetilde{\mu}_f}{\widetilde{\rho}_{hnf}/\widetilde{\rho}_f} \frac{\widetilde{\mu}_f}{\widetilde{\rho}_f} \frac{\mathrm{f}'}{\psi_1\psi_2 k}.$$

$$\Rightarrow \quad \mathrm{f}'^2 - \mathrm{f}\, \mathrm{f}'' = \frac{P_1}{P_2} \mathrm{f}''' - \frac{P_4}{P_2} M\, \mathrm{f}' - \frac{P_1}{P_2} K_1\, \mathrm{f}'.$$

$$\Rightarrow \quad P_1\, \mathrm{f}''' + P_2\big(\mathrm{f}\, \mathrm{f}'' - \mathrm{f}'^2\big) - P_4\, M\, \mathrm{f}' - P_1\, K_1\, \mathrm{f}' = 0. \tag{2.12}$$

2.3.2 Non-dimensionalization of Energy Equation

In this section, we describe how the energy equation (2.3) is simplified by introducing the non-dimensional variables for the hybrid nanofluid model.

$$\theta = \frac{\mathrm{T} - \mathrm{T}_\infty}{\mathrm{T}_w - \mathrm{T}_\infty} \qquad .$$

$$\Rightarrow \quad \mathrm{T} = \theta\left(\mathrm{T}_w - \mathrm{T}_\infty\right) + \mathrm{T}_\infty.$$

$$\Rightarrow \quad \mathrm{T} = \theta\, b\mathrm{x}^2 + \mathrm{T}_\infty. \tag{2.13}$$

$$\Rightarrow \quad \frac{\partial \mathrm{T}}{\partial \mathrm{x}} = 2b\mathrm{x}\theta \tag{2.14}$$

$$\Rightarrow \quad \frac{\partial \mathrm{T}}{\partial \mathrm{y}} = \frac{\partial}{\partial \mathrm{y}}(b\mathrm{x}^2\theta + \mathrm{T}_\infty)$$

$$= b\mathrm{x}^2\psi_1\theta'. \tag{2.15}$$

$$\Rightarrow \quad \frac{\partial^2 \mathrm{T}}{\partial \mathrm{y}^2} = \frac{\partial}{\partial \mathrm{y}}(b\mathrm{x}^2\psi_1\theta')$$

$$= b\mathrm{x}^2\psi_1^2\theta''. \tag{2.16}$$

The expression for the radiative heat flux q_r is given by:

$$q_r = -\frac{4\sigma^*}{3k^*}\frac{\partial \mathrm{T}^4}{\partial \mathrm{y}}. \tag{2.17}$$

In this relation, σ^* represents the Stefan–Boltzmann parameter, whereas k^* corresponds to the mean absorption coefficient. When the temperature variation within the flow field is sufficiently small, the nonlinear term T^4 can be approximated by a Taylor series expansion around the point T_∞, which leads to the following expression:

$$\mathrm{T}^4 = \mathrm{T}_\infty^4 + 4\mathrm{T}_\infty^3(\mathrm{T} - \mathrm{T}_\infty) + 6\mathrm{T}_\infty^2(\mathrm{T} - \mathrm{T}_\infty)^2 + \cdots$$

Ignoring the higher-order effects, the following relation is obtained:

$$\mathrm{T}^4 = \mathrm{T}_\infty^4 + 4\mathrm{T}_\infty^3(\mathrm{T} - \mathrm{T}_\infty),$$

$$= 4\mathrm{T}_\infty^3\mathrm{T} - 3\mathrm{T}_\infty^4.$$

After replacing the expression for T^4 into (2.17), the following expression is obtained.

$$q_r = -\frac{4\sigma^*}{3k^*}\frac{\partial}{\partial \mathrm{y}}(4\mathrm{T}_\infty^3\mathrm{T} - 3\mathrm{T}_\infty^4)$$

$$= -\frac{4\sigma^*}{3k^*}4\mathrm{T}_\infty^3\frac{\partial \mathrm{T}}{\partial \mathrm{y}}$$

$$= -\frac{16\sigma^*}{3k^*}\mathrm{T}_\infty^3\frac{\partial \mathrm{T}}{\partial \mathrm{y}}. \tag{2.18}$$

$$\Rightarrow \frac{\partial q_r}{\partial y} = \frac{\partial}{\partial y}\left(-\frac{16\sigma^*}{3k^*}\mathrm{T}_\infty^3\frac{\partial \mathrm{T}}{\partial y}\right)$$

$$= -\frac{16\sigma^*}{3k^*}\mathrm{T}_\infty^3\frac{\partial^2 \mathrm{T}}{\partial \mathrm{y}^2}$$

$$= -\frac{16\sigma^*}{3k^*}\mathrm{T}_\infty^3 b\mathrm{x}^2\psi_1^2\theta''(\eta). \tag{2.19}$$

Using equations (2.6), (2.7), (2.14), (2.15), (2.16) and (2.19) into the energy equation (2.4), we obtain the following equation.

$$(\psi_1\psi_2 \mathrm{x}\,\mathrm{f}'(\eta))(2b\mathrm{x}\,\theta(\eta)) + (-\psi_2 f(\eta))(b\mathrm{x}^2\psi_1\theta'(\eta)) + \frac{1}{(\widetilde{\rho c_p})_{hnf}}\frac{16\sigma^*}{3k^*}\mathrm{T}_\infty^3\left(b\mathrm{x}^2\psi_1^2\theta''(\eta)\right)$$
$$= \frac{\widetilde{K}_{hnf}}{(\widetilde{\rho C_p})_{hnf}}\left(b\mathrm{x}^2\psi_1^2\theta''(\eta)\right).$$

$$\Rightarrow \quad 2\psi_1\psi_2 b\mathrm{x}^2\mathrm{f}'\,\theta - \psi_1\psi_2 b\mathrm{x}^2\,\mathrm{f}\,\theta + \frac{1}{(\widetilde{\rho c_p})_{hnf}}\frac{-16\sigma^*}{3k^*}\mathrm{T}_\infty^3 b\mathrm{x}^2\psi_1^2\theta'' = \frac{\widetilde{K}_{hnf}}{(\widetilde{\rho c_p})_{hnf}}b\mathrm{x}^2\psi_1^2\theta''(\eta).$$

$$\Rightarrow \quad 2\mathrm{f}'\,\theta - \mathrm{f}\,\theta' = \frac{\widetilde{K}_{hnf}}{(\widetilde{\rho c_p})_{hnf}}\frac{\psi_1\,\theta''}{\psi_2} + \frac{1}{(\widetilde{\rho c_p})_{hnf}}\frac{16\sigma^*}{3k^*}\,\mathrm{T}_\infty^3\frac{\psi_1\,\theta''}{\psi_2}.$$

$$\Rightarrow \quad 2\mathrm{f}'\,\theta - \mathrm{f}\,\theta' = \frac{1}{(\widetilde{\rho c_p})_{hnf}}\frac{\psi_1}{\psi_2}\left(\widetilde{K}_{hnf} + \frac{16\sigma^*}{3k^*}\,\mathrm{T}_\infty^3\right)\theta''.$$

$$\Rightarrow \quad 2\mathrm{f}'\,\theta - \mathrm{f}\,\theta' = \frac{1}{(\widetilde{\rho c_p})_{hnf}/(\widetilde{\rho c_p})_f}\frac{1}{(\widetilde{\rho c_p})_f}\frac{\widetilde{\rho}_f}{\widetilde{\mu}_f}\left(\frac{\widetilde{K}_{hnf}\,\widetilde{K}_f}{\widetilde{K}_f} + \frac{16\sigma^*}{3k^*}\,\mathrm{T}_\infty^3\right)\theta''.$$

$$\Rightarrow \quad 2\mathrm{f}'\,\theta - \mathrm{f}\,\theta' = \frac{1}{(\widetilde{\rho c_p})_{hnf}/(\widetilde{\rho c_p})_f}\frac{1}{(\widetilde{\rho c_p})_f}\frac{\widetilde{\rho}_f}{\widetilde{\mu}_f}\widetilde{K}_f\left(\frac{\widetilde{K}_{hnf}}{\widetilde{K}_f} + \frac{16\sigma^*}{3k^*\widetilde{K}_f}\,\mathrm{T}_\infty^3\right)\theta''.$$

$$\Rightarrow \quad 2\mathrm{f}'\,\theta - \mathrm{f}\,\theta' = \frac{1}{P_5 Pr}\left(P_3 + \frac{4R}{3}\right)\theta''.$$

$$\Rightarrow \quad \frac{1}{P_5 Pr}\left(P_3 + \frac{4R}{3}\right)\theta'' - 2\mathrm{f}'\,\theta + \mathrm{f}\,\theta' = 0. \tag{2.20}$$

The expressions for the parameters used in above equations are given below:

$$M = \frac{B_0^2\,\widetilde{\sigma}_f}{\widetilde{\rho}_f\,\psi_1\,\psi_2}, \quad K_1 = \frac{v_f}{\psi_1\psi_2 k},$$

$$Pr = \frac{(\widetilde{\rho c_p})_f\,\nu_f}{\widetilde{K}_f}, \quad R = \frac{4\sigma^*\mathrm{T}_\infty^3}{k^*\,\widetilde{K}_f}.$$

2.3.3 Non-dimensionalization of Boundary Condition

- $\mathrm{v} = \mathrm{v}_w, \qquad at \quad \mathrm{y} = 0.$

  $\Rightarrow \; -\psi_2 \mathrm{f}(\eta) = \psi_2 \mathrm{f}_w, \qquad at \quad \eta = 0.$

  $\Rightarrow \; \mathrm{f}(0) = \mathrm{f}_w.$

- $\mathrm{T} = \mathrm{T}_w = \mathrm{T}_\infty + b\mathrm{x}^2, \qquad at \quad \mathrm{y} = 0.$

  $\Rightarrow \; \theta(\mathrm{T}_w - \mathrm{T}_\infty) + \mathrm{T}_\infty = \mathrm{T}_\infty + b\mathrm{x}^2, \qquad at \quad \eta = 0.$

  $\Rightarrow \; \theta = \dfrac{b\mathrm{x}^2}{\mathrm{T}_w - \mathrm{T}_\infty}, \qquad at \quad \eta = 0.$

  $\Rightarrow \; \theta(0) = 1.$

- $\widetilde{\mu}_{hnf} \dfrac{\partial \mathrm{x}}{\partial \mathrm{y}} = \dfrac{\partial \gamma}{\partial \mathrm{T}} \dfrac{\partial \mathrm{T}}{\partial \mathrm{x}}, \qquad at \quad y = 0.$

  $\Rightarrow \; \widetilde{\mu}_{hnf} \psi_1^2 \psi_2 \mathrm{x}\, \mathrm{f}'' = -\bar{\gamma}\bar{\gamma_o} 2b\mathrm{x}\theta, \qquad at \quad \eta = 0.$

  $\Rightarrow \; \widetilde{\mu}_{hnf} \psi_1^2 \psi_2 \mathrm{x}\, \mathrm{f}'' = -\bar{\gamma}\bar{\gamma_o} 2b\mathrm{x}\theta, \qquad at \quad \eta = 0.$

  $\Rightarrow \; \dfrac{\widetilde{\mu}_{hnf}\widetilde{\mu}_f}{\widetilde{\mu}_f} \left(\dfrac{\gamma_o \bar{\gamma} b \widetilde{\mu}_f^{\frac{1}{3}} \mathrm{f}''(\eta)}{\widetilde{\mu}_f^{\frac{4}{3}}} \right) = (-\bar{\gamma}\bar{\gamma_o})(2b\theta(\eta)), \qquad at \quad \eta = 0.$

  $\Rightarrow \; P_1 \mathrm{f}''(0) = -2\theta(0), \qquad at \quad \eta = 0.$

  $\Rightarrow \; \mathrm{f}''(0) = -\dfrac{2}{P_1}.$

- $\mathrm{u} \longrightarrow 0 \qquad as \quad \mathrm{y} \longrightarrow \infty.$

  $\Rightarrow \; \psi_1 \psi_2 \mathrm{x}\, \mathrm{f}' \longrightarrow 0, \qquad as \quad \eta \longrightarrow \infty.$

  $\Rightarrow \; \mathrm{f}' \longrightarrow 0, \qquad as \quad \eta \longrightarrow \infty.$

- $\mathrm{T} \longrightarrow \mathrm{T}_\infty, \qquad as \quad \mathrm{y} \longrightarrow \infty.$

$\Rightarrow \ \mathrm{T}_\infty + \big(\mathrm{T}_w - \mathrm{T}_\infty\big)\theta \longrightarrow \mathrm{T}_\infty, \qquad as \quad \eta \longrightarrow \infty.$

$\Rightarrow \ \theta \longrightarrow 0, \qquad as \quad \eta \longrightarrow \infty.$

2.3.4 Non-dimensionalization of Nusselt Number

Nusselt number describes how much heat is carried away by convection compared to how much is conducted through the fluid at the surface.

Mathematically, the dimensional expression for the surface heat transfer parameter is:

$$Nu_x = \frac{\mathrm{x}\, q_w}{\widetilde{K}_f(\mathrm{T}_w - \mathrm{T}_\infty)},$$

where q_w denotes the total surface heat flux represented as:

$$q_w = -\widetilde{K}_{hnf}\left(\frac{\partial \mathrm{T}}{\partial \mathrm{y}}\right)_{\mathrm{y}=0} + (q_r)_{\mathrm{y}=0}.$$

The Nusselt number can be converted into its dimensionless form as:

$$Nu_x = \frac{\mathrm{x}}{\widetilde{K}_f(\mathrm{T}_w - \mathrm{T}_\infty)}\left(- \widetilde{K}_{hnf}\left(\frac{\partial \mathrm{T}}{\partial \mathrm{y}}\right)_{\mathrm{y}=0} + (q_r)_{\mathrm{y}=0}\right),$$

$$= \frac{\mathrm{x}}{\widetilde{K}_f(\mathrm{T}_w - \mathrm{T}_\infty)}\left(- \widetilde{K}_{hnf}\theta'(0)\psi_1(\mathrm{T}_w - \mathrm{T}_\infty) - \frac{16\sigma^*}{3k^*}\mathrm{T}_\infty^3(\mathrm{T}_w - \mathrm{T}_\infty)\psi_1\theta'(0)\right)$$

$$= \frac{\mathrm{x}(\mathrm{T}_w - \mathrm{T}_\infty)}{\widetilde{K}_f(\mathrm{T}_w - \mathrm{T}_\infty)}\left(- \widetilde{K}_{hnf} - \frac{16\sigma^*}{3k^*}\mathrm{T}_\infty^3\right)\theta'(0)\psi_1$$

$$= -\frac{\mathrm{x}}{\widetilde{K}_f}\left(\widetilde{K}_{hnf} + \frac{16\sigma^*}{3k^*}\mathrm{T}_\infty^3\right)$$

$$= -\left(\frac{\widetilde{K}_{hnf}}{\widetilde{K}_f} + \frac{4R}{3}\right)\mathrm{x}\psi_1\theta'(0). \tag{2.21}$$

2.4 Solution Framework

To obtain a solution of the ODE (2.12), the shooting approach is employed. Some new variables have been introduced, as below.

$$\mathrm{f}(\eta) = \widetilde{m}_1, \quad \mathrm{f}'(\eta) = \widetilde{m}_1' = \widetilde{m}_2, \quad \mathrm{f}''(\eta) = \widetilde{m}_2' = \widetilde{m}_3.$$

The momentum equation is transformed into an equivalent system of first-order ODEs.

$$\left.\begin{aligned} \widetilde{m}_1' &= \widetilde{m}_2, & \widetilde{m}_1(0) &= f_w, \\ \widetilde{m}_2' &= \widetilde{m}_3, & \widetilde{m}_2(0) &= r, \\ \widetilde{m}_3' &= \frac{P_2}{P_1}\left[\widetilde{m}_2^2 - \widetilde{m}_1\widetilde{m}_3\right] + \frac{P_4}{P_1}M\widetilde{m}_2 + K_1\widetilde{m}_2, & \widetilde{m}_3(0) &= -\frac{2}{P_1}. \end{aligned}\right\} \tag{2.22}$$

The computational domain is taken as $[0, \eta_\infty]$. In this work, $\eta_\infty = 5$ is chosen, since the numerical solution converges within this range. To implement the Runge–Kutta 4th-order (RK4) method, the missing condition specified as r must be chosen carefully, in such a way that:

$$\widetilde{m}_2\big(\eta_\infty, r\big) = 0.$$

By applying Newton's method, selection of r can be improved further. The iterative scheme of this method is given below:

$$r^{(n+1)} = r^{(n)} - \frac{\widetilde{m}_2\big(\eta_\infty, r^{(n)}\big)}{\big(\frac{\partial}{\partial r}\widetilde{m}_2\big(\eta_\infty, r\big)\big)^{(n)}}.$$

The following notations are introduced further, to compute $\frac{\partial}{\partial r}\widetilde{m}_2\big(\eta_\infty, r\big)$:

$$\frac{\partial \widetilde{m}_1}{\partial r} = \widetilde{m}_4, \quad \frac{\partial \widetilde{m}_2}{\partial r} = \widetilde{m}_5, \quad \frac{\partial \widetilde{m}_3}{\partial r} = \widetilde{m}_6.$$

The Newton iterative scheme takes the following form by using the above notations:

$$r^{(n+1)} = r^{(n)} - \frac{\widetilde{m}_2\big(\eta_\infty, r^{(n)}\big)}{\widetilde{m}_5\big(\eta_\infty, r\big)}.$$

Now differentiating the above system of three first order ODEs with respect to r, we get another system of ODEs, as follows:

$$\left.\begin{aligned} \widetilde{m}_4' &= \widetilde{m}_5, & \widetilde{m}_4(0) &= 0, \\ \widetilde{m}_5' &= \widetilde{m}_6, & \widetilde{m}_5(0) &= 1, \\ \widetilde{m}_6' &= \frac{P_3(2\widetilde{m}_2\widetilde{m}_5 - \widetilde{m}_1\widetilde{m}_6 - \widetilde{m}_4\widetilde{m}_3) + P_4\widetilde{m}\widetilde{m}_5}{P_1} & & \\ &\quad + K_1\widetilde{m}_2, & \widetilde{m}_6(0) &= 0. \end{aligned}\right\} \tag{2.23}$$

The IVPs mentioned in (2.22) and (2.23) will be solved by using RK4 method.

The stopping criteria for the Newton's technique is set as:

$$|\widetilde{m}_2\left(\eta_\infty, r\right)| < \epsilon,$$

In this study, ϵ is introduced as a small positive constant and is set equal to 10^{-9}. To numerically solve equation (2.20), the functions f and f$'$ are assumed to be known. The notations adopted for implementing the shooting procedure are listed below:

$$\theta'(\eta) = \widetilde{n}_1, \qquad \theta'(\eta) = \widetilde{n}_1' = \widetilde{n}_2.$$

The initial value problem for the energy equation is given as:

$$\left.\begin{aligned} \widetilde{n}_1' &= \widetilde{n}_2, & \widetilde{n}_1(0) &= 1, \\ \widetilde{n}_2' &= \frac{P_5 Pr(2\mathrm{f}'\widetilde{n}_1 - \mathrm{f}\widetilde{n}_2)}{P_5 + 4R/3}, & \widetilde{n}_2(0) &= s. \end{aligned}\right\} \tag{2.24}$$

The missing condition s must be chosen carefully to ensure that:

$$\widetilde{n}_2\big(\eta_\infty, s\big) = 0.$$

The value of s will be updated through Newton's method, which proceeds following the iterative relation presented below:

$$s^{(n+1)} = s^{(n)} - \frac{\widetilde{n}_2\big(\eta_\infty, s^{(n)}\big)}{\big(\frac{\partial}{\partial s}\widetilde{n}_2\big(\eta_\infty, s\big)\big)^{(n)}}.$$

To proceed further the following notations are introduced:

$$\frac{\partial \widetilde{n}_1}{\partial s} = \widetilde{n}_3, \qquad \frac{\partial \widetilde{n}_2}{\partial s} = \widetilde{n}_4.$$

The Newtons iterative scheme takes the following form:

$$s^{(n+1)} = s^{(n)} - \frac{\widetilde{n}_2\big(\eta_\infty, s^{(n)}\big)}{\widetilde{n}_4\big(\eta_\infty, s\big)}.$$

Differentiating (2.24) with respect to s leads to the following system of ODEs.

$$\left.\begin{aligned} \widetilde{n}_3' &= \widetilde{n}_4, & \widetilde{n}_1(0) &= 0, \\ \widetilde{n}_4' &= \frac{P_5 Pr(2\mathrm{f}'\widetilde{n}_3 - \mathrm{f}\widetilde{n}_4)}{P_5 + 4R/3}, & \widetilde{n}_2(0) &= 1. \end{aligned}\right\} \tag{2.25}$$

The Newton iteration proceeds until the following condition is met:

$$|\widetilde{n}_2\left(\eta_\infty, s\right)| < \epsilon.$$

2.5 Results and Discussion

This section examines the velocity and temperature profiles of the hybrid nanofluid. A discussion of the variation in the Nusselt number is then presented to provide insight into the flow behavior and thermal performance of the system. The influence of key governing parameters on the velocity and temperature distribution is clearly illustrated through graphical representations. Additionally, the resulting Nusselt number along with the missing boundary condition $\mathrm{f}'(0)$ and the corresponding validity interval for which the numerical solution is stable have been added in tabular form. An analysis of these profiles helps clarify the role of different parameters in shaping the flow behavior and thermal characteristics of the system.

2.5.1 Analysis of Computational Results

Table 2.3 summarizes the results of the missing condition f′(0) and local Nusselt number for the $Cu - Al_2O_3$/kerosene-oil hybrid nanofluid. The value of f′(0) is identified numerically using the shooting method and the interval (I_f) over which the numerical solution stays stable and convergent, is also presented. Variations in the flow behavior are examined by changing the key parameters M, ϕ_1, ϕ_2, K_1, and f_w.

TABLE 2.3: Variation of Nu_x, f′(0) and interval of validity I_f for different physical parameters.

M	ϕ_1	ϕ_2	K_1	f_w	Pr	R	Nu_x	f′(0)	I_f
0.5	0.02	0.02	0.5	0.5	21	1	7.29836	1.00715	[0.91, 3.31]
0							7.50571	1.09390	[1.00, 3.70]
0.3							7.37716	1.03967	[0.94, 3.47]
0.8							7.18928	0.96304	[0.87, 3.08]
1							7.12201	0.93636	[0.85, 2.94]
	0						7.52085	1.09369	[0.98, 3.65]
	0.01						7.40646	1.04853	[0.94, 3.50]
	0.03						7.19561	0.96990	[0.87, 3.21]
	0.1						6.57686	0.76398	[0.68, 2.63]
		0					7.45327	1.05453	[0.95, 3.40]
		0.01					7.37544	1.03047	[0.93, 3.35]
		0.03					7.22193	0.98453	[0.88, 3.28]
		0.1					6.70050	0.84243	[0.74, 3.19]
			0				7.50173	1.0922	[1.00, 3.73]
			0.3				7.37572	1.03907	[0.94, 3.49]
			0.8				7.19112	0.96378	[0.87, 3.11]
			1				7.12490	0.93750	[0.85, 2.94]
				-1			2.40369	1.52546	[1.52, 2.28]
				-0.5			3.21165	1.34856	[1.32, 2.57]
				0			4.76201	1.17365	[1.12, 2.93]
				1			10.63133	0.85633	[0.69, 3.75]
					10		4.21770	1.00715	[0.91, 3.31]
					15		5.67686	1.00715	[0.91, 3.31]
					25		8.33165	1.00715	[0.91, 3.31]
					30		9.58690	1.00715	[0.91, 3.31]
						1.5	6.09811	1.00715	[0.91, 3.31]
						2	5.28567	1.00715	[0.91, 3.31]
						2.5	4.69382	1.00715	[0.91, 3.31]
						3	4.24037	1.00715	[0.91, 3.31]

The results indicate that stronger magnetic effects lead to lower values of f′(0), as electromagnetic resistance acts against fluid motion near the surface. Likewise, greater nanoparticle presence reduces f′(0) by increasing the effective viscosity of the hybrid nanofluid, thereby limiting fluid mobility. The presence of higher permeability introduces additional drag within the porous medium, which further weakens the near-wall flow. In addition, as the suction/injection parameter f_w transitions from negative values to positive values, a clear decline in f′(0) is observed. Physically injection supports the boundary-layer motion by supplying fluid whereas, suction extracts fluid from the surface region, leading to a reduction in surface velocity.

The Nusselt number exhibits noticeable variation with changes in the governing parameters. A rise in the Prandtl number is associated with lower Nusselt number values, indicating weaker heat transfer at the surface. Stronger radiation effects, magnetic influence, higher nanoparticle volume fractions and greater permeability lead to diminish heat transfer at the wall. Together, these factors hinder heat transport and smooth out the temperature variations close to the surface.In contrast, larger values of f_w lead to higher Nusselt number due to thinning of the thermal boundary layer.

2.5.2 Velocity Profile

Figure 2.2 presents the impact of the magnetic parameter M on the velocity profile f′(η). It is evident that stronger magnetic effects lead to a reduction in the fluid velocity. This behavior is attributed to the electromagnetic resistance generated by the applied magnetic field, which acts in opposition to the flow direction. This opposing force limits fluid motion, leading to a decelerated flow and a diminished velocity profile.

The permeability parameter plays an important role in controlling the flow movement. It is observed that larger values of K_1 lead to a reduced momentum boundary layer. This is because porous medium offers greater resistance to the moving fluid, which limits its ability to pass freely through the pores. As a result, the flow

becomes weaker near the surface, leading to a lower velocity distribution. This trend is clearly depicted in Figure 2.3.

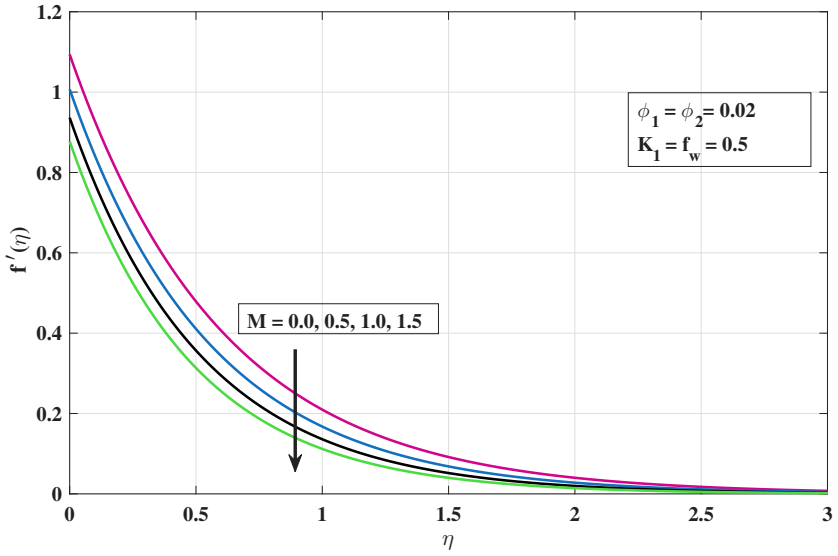

FIGURE 2.2: Impact of M on f′

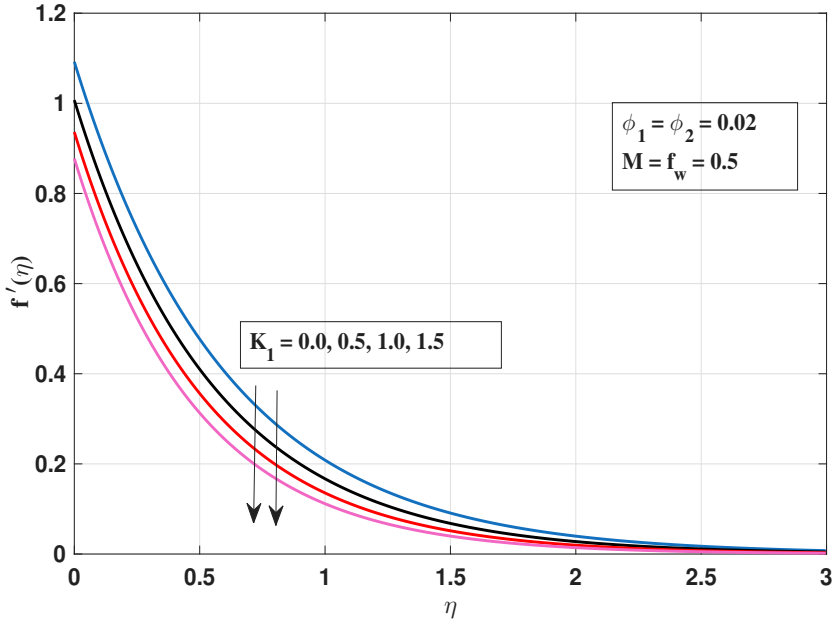

FIGURE 2.3: Impact of K_1 on f′

The velocity profile is found to decline as the wall mass transfer parameter f_w moves towards higher values. When fluid injection is applied, additional fluid enters the boundary layer, which supports the flow and maintains higher velocities near the surface. In contrast, suction withdraws fluid from the boundary layer, reducing the amount of fluid participating in the motion. This extraction weakens

the flow near the wall and leads to a noticeable reduction in velocity, as illustrated in Figure 2.4

The impact of nanoparticle volume fractions on the velocity distribution is illustrated in Figure 2.5. It is observed that larger values of ϕ_1 and ϕ_2 lead to a lower velocity profile. This behavior arises because the presence of additional nanoparticles increases the overall thickness and resistance of the hybrid mixture, which restricts its ability to move freely. As a result, the motion within the boundary layer becomes slower.

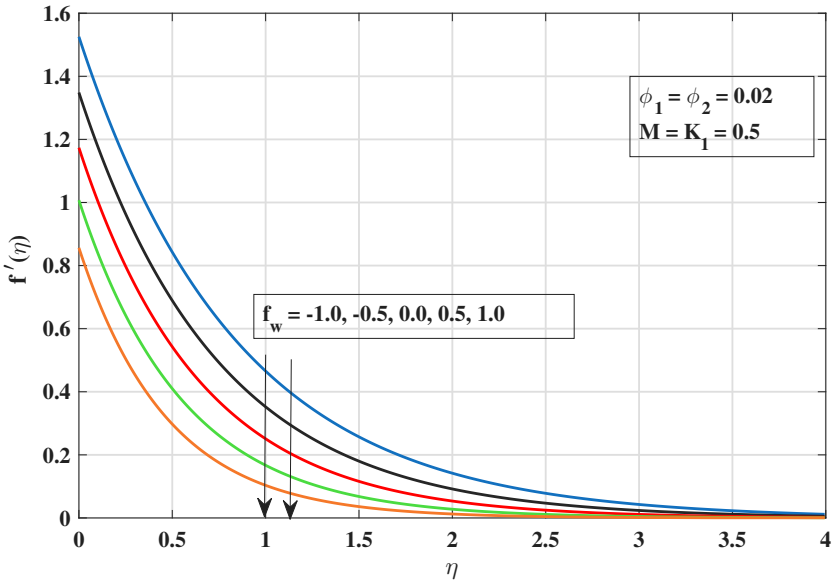

FIGURE 2.4: Impact of f_w on f

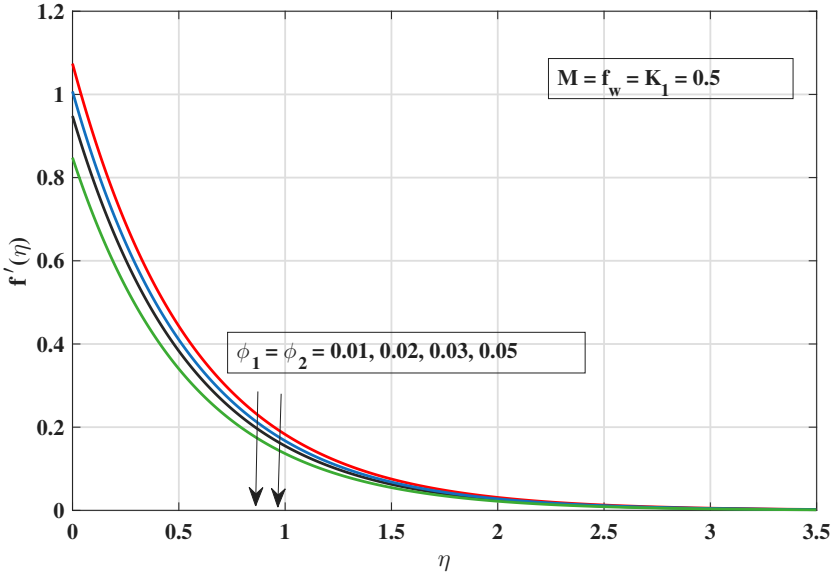

FIGURE 2.5: Impact of nanoparticle volume fractions on f'

2.5.3 Temperature Profile

Figures 2.6 to 2.8 present the behavior of the temperature profile $\theta(\eta)$ with respect to various physical parameters. It is observed in Figure 2.6 that there is a notable decrease in temperature corresponding to higher values of the Prandtl number.

The base fluid used in this study, kerosene oil, naturally has a high Prandtl value. This indicates that the fluid transfers heat slowly and retains most of the thermal energy near the surface. Consequently, the temperature declines more rapidly as the fluid moves away from the wall, leading to a reduced temperature profile.

The temperature distribution exhibits an upward trend for elevated values of the radiation parameter(R), as shown in Figure 2.7. This occurs because stronger radiation introduces additional thermal energy into the fluid. The continuous supply of radiative energy increases the thermal energy stored within the medium. Consequently, the temperature level rises throughout the flow region.

Figure 2.8 indicates that higher nanoparticle presence leads to an elevated temperature distribution. Since ϕ_1 and ϕ_2 possess higher thermal conductivity, they enable the fluid to carry and retain more heat. As a result, the overall temperature within the boundary layer rises.

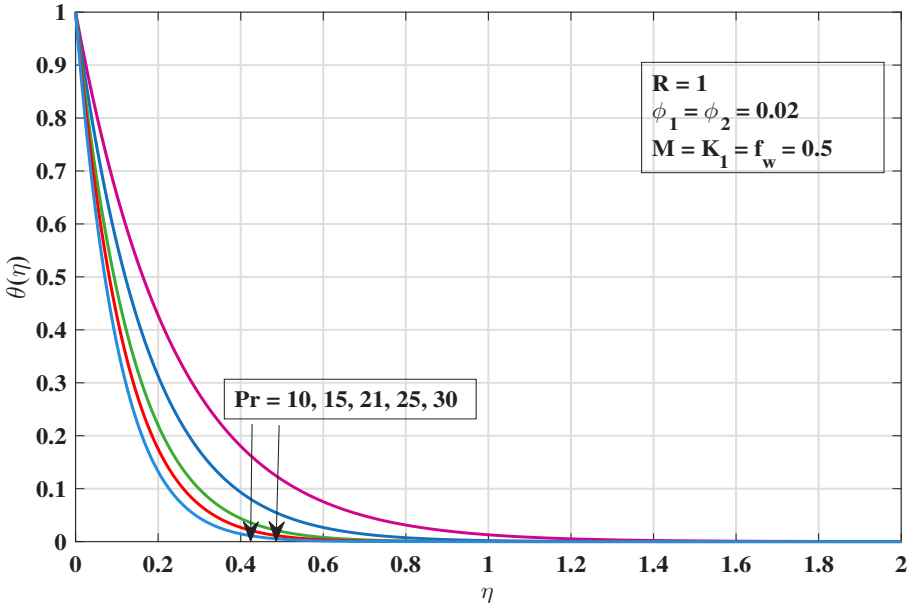

FIGURE 2.6: Influence of Pr on θ

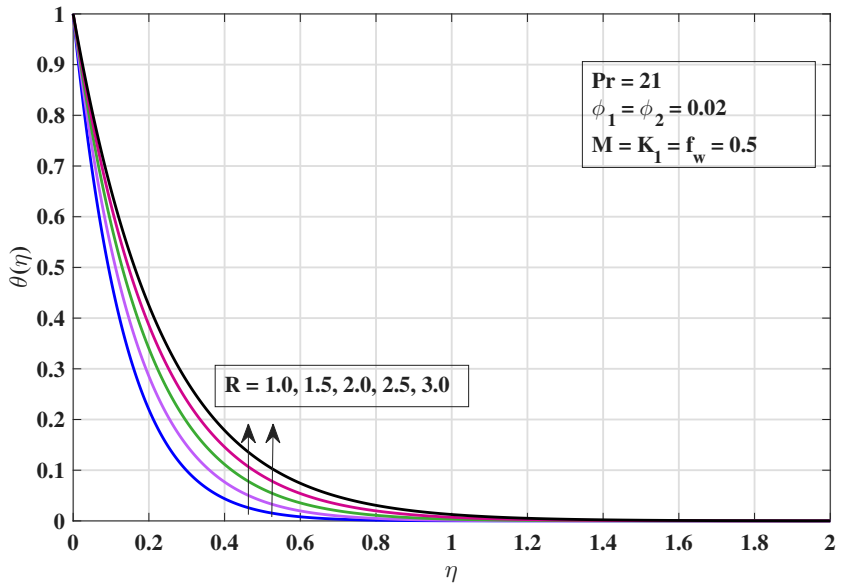

FIGURE 2.7: Influence of R on θ

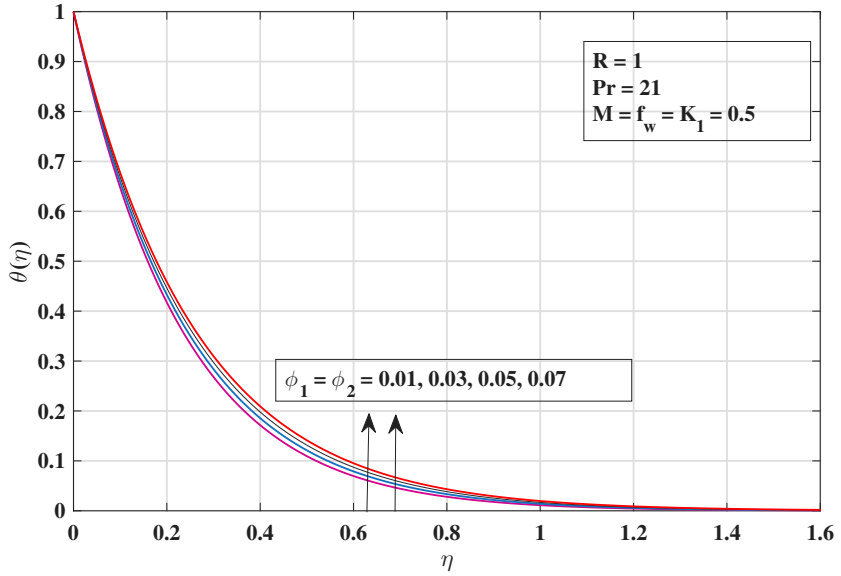

FIGURE 2.8: Influence of volume fractions on θ

Chapter 3

Marangoni MHD Flow with Relaxation Effects, Linear Reaction and Internal Heat Generation

3.1 Introduction

In Chapter 2, the Marangoni convective flow of a Cu–Al_2O_3/kerosene-oil hybrid nanofluid was analyzed considering fundamental transport mechanisms. In the present work, this model is further developed to include additional physical processes for a more complete description of the flow system. The momentum equation is preserved in the same form, whereas the energy equation is further enriched by incorporating internal heat generation, Brownian and thermophoresis motion, together with the Cattaneo–Christov heat flux model.

This approach accounts for finite thermal relaxation and provides a more accurate description of thermal transport in hybrid nanofluids. Furthermore, a concentration equation is introduced to account for mass diffusion effects with relaxation

characteristics, along with a first-order chemical reaction term enabling the inclusion of double-diffusive transport phenomenon. As a result, the coupled effects of heat and mass transport on Marangoni convection can be examined more thoroughly within the hybrid nanofluid framework.

3.2 Physical Model

In the current investigation, the laminar behavior of a viscous and incompressible hybrid nanofluid interacting with a porous surface is studied. The flow geometry is defined by aligning the x-direction with the fluid motion and the y-direction normal to the surface. Additionally, a uniform transverse magnetic field of magnitude B_o is applied. The temperature and concentration at the surface are denoted by T_w and C_w, respectively.

Far from the boundary, temperature and concentration settle to their ambient values, indicated by T_∞ and C_∞. Additional relations are incorporated to represent the influence of the applied physical mechanisms on mass transport within the boundary layer, as presented in equations (3.1) and (3.2)[25].

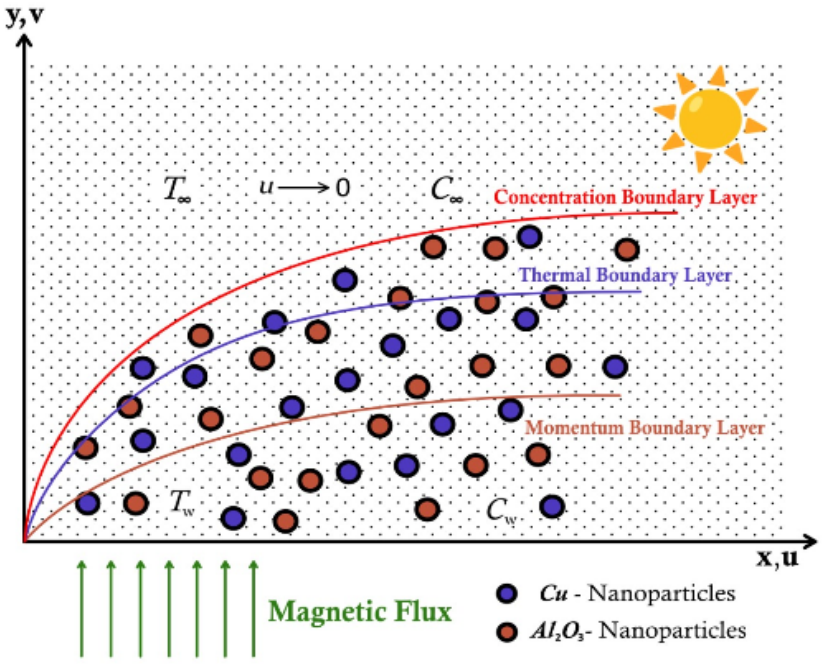

FIGURE 3.1: Flow Configuration

Energy Equation:

$$\mathrm{u}\frac{\partial \mathrm{T}}{\partial \mathrm{x}}+\mathrm{v}\frac{\partial \mathrm{T}}{\partial \mathrm{y}}+\lambda_1\left(\mathrm{u}\frac{\partial \mathrm{u}}{\partial \mathrm{v}}\frac{\partial \mathrm{T}}{\partial x}+\mathrm{v}\frac{\partial \mathrm{v}}{\partial \mathrm{y}}\frac{\partial \mathrm{T}}{\partial \mathrm{y}}+\mathrm{v}\frac{\partial \mathrm{u}}{\partial \mathrm{y}}\frac{\partial \mathrm{T}}{\partial \mathrm{x}}+2\mathrm{uv}\frac{\partial^2 \mathrm{T}}{\partial \mathrm{x}\partial \mathrm{y}}+\mathrm{u}^2\frac{\partial^2 \mathrm{T}}{\partial x^2}+\mathrm{v}^2\frac{\partial^2 \mathrm{T}}{\partial \mathrm{y}^2}\right)$$
$$+\frac{1}{(\widetilde{\rho}\widetilde{C}_p)_{hnf}}\left(\frac{\partial q_r}{\partial \mathrm{y}}\right)=\frac{\widetilde{K}_{hnf}}{(\widetilde{\rho}\widetilde{C}_p)_{hnf}}\frac{\partial^2 \mathrm{T}}{\partial \mathrm{y}^2}+\frac{\widetilde{\sigma}_{hnf}}{(\widetilde{\rho}\widetilde{C}_p)_{hnf}}B_0^2\mathrm{u}^2+\frac{\widetilde{\mu}_{hnf}}{(\widetilde{\rho}\widetilde{C}_p)_{hnf}}\frac{\mathrm{u}^2}{k}$$
$$+\frac{q}{(\widetilde{\rho}\widetilde{C}_p)_{hnf}}(\mathrm{T}-\mathrm{T}_\infty)+\tau\left(D_B\frac{\partial \mathrm{C}}{\partial \mathrm{y}}\frac{\partial \mathrm{T}}{\partial \mathrm{x}}+\frac{D_T}{\mathrm{T}_\infty}\left(\frac{\partial \mathrm{T}}{\partial \mathrm{y}}\right)^2\right). \tag{3.1}$$

Concentration Equation:

$$\mathrm{v}\frac{\partial \mathrm{C}}{\partial \mathrm{y}}+\mathrm{u}\frac{\partial \mathrm{C}}{\partial \mathrm{x}}+\lambda_2\left(\mathrm{u}\frac{\partial \mathrm{u}}{\partial \mathrm{v}}\frac{\partial \mathrm{C}}{\partial \mathrm{x}}+\mathrm{v}\frac{\partial \mathrm{v}}{\partial \mathrm{y}}\frac{\partial \mathrm{C}}{\partial \mathrm{y}}+\mathrm{v}\frac{\partial \mathrm{u}}{\partial \mathrm{y}}\frac{\partial \mathrm{C}}{\partial \mathrm{x}}+2\mathrm{uv}\frac{\partial^2 \mathrm{C}}{\partial \mathrm{x}\partial \mathrm{y}}+\mathrm{u}^2\frac{\partial^2 \mathrm{C}}{\partial \mathrm{x}^2}+\mathrm{v}^2\frac{\partial^2 \mathrm{C}}{\partial \mathrm{y}^2}\right)$$
$$=D_B\frac{\partial^2 \mathrm{C}}{\partial \mathrm{y}^2}+\frac{D_T}{\mathrm{T}_\infty}\frac{\partial^2 \mathrm{T}}{\partial \mathrm{y}^2}+K_r\left(\mathrm{C}_\infty-\mathrm{C}\right). \tag{3.2}$$

Boundary Conditions

$$\left.\begin{aligned}&\mathrm{v}=\mathrm{v}_w,\quad \widetilde{\mu}_{hnf}\left(\frac{\partial \mathrm{u}}{\partial \mathrm{y}}\right)=\frac{\partial \sigma}{\partial \mathrm{T}}\frac{\partial \mathrm{T}}{\partial \mathrm{x}},\\&\mathrm{T}=\mathrm{T}_\infty+b\mathrm{x}^2,\quad \mathrm{C}=\mathrm{C}_\infty+b\mathrm{x}^2 && \text{at } \mathrm{y}=0,\\&\mathrm{T}\to\mathrm{T}_\infty,\quad \mathrm{u}\to 0,\quad \mathrm{C}\to\mathrm{C}_\infty, && \text{as } \mathrm{y}\to\infty.\end{aligned}\right\} \tag{3.3}$$

3.3 Similarity Transformation and Non- dimensionalization of Mathematical Model

This section outlines the procedure used to scale the mathematical model into a dimensionless form. Appropriate nondimensional variables and parameters are introduced to simplify the governing relations. This approach enhances the physical interpretation and reduces the system to a set of ODEs through suitable similarity transformations.

$$\left.\begin{aligned}&\eta=\psi_1\mathrm{y},\quad \xi=\psi_2\mathrm{x}\,\mathrm{f}(\eta),\quad \theta(\eta)=\frac{\mathrm{T}-\mathrm{T}_\infty}{\mathrm{T}_w-\mathrm{T}_\infty},\quad \phi(\eta)=\frac{\mathrm{C}-\mathrm{C}_\infty}{\mathrm{C}_w-\mathrm{C}_\infty},\\&\mathrm{u}=\frac{\partial \xi}{\partial \mathrm{y}},\quad \psi_1=\left(\frac{\gamma_0\gamma b\widetilde{\rho}_f}{\widetilde{\mu}_f^2}\right)^{1/3},\quad \psi_2=\left(\frac{\gamma_0\gamma b\widetilde{\mu}_f}{\widetilde{\rho}_f^2}\right)^{1/3},\quad \mathrm{v}=-\frac{\partial \xi}{\partial \mathrm{y}}.\end{aligned}\right\} \tag{3.4}$$

The transformed ODEs involve a set of dimensionless parameters that describe the flow characteristics, heat transfer, and mass diffusion effects. These parameters are listed in the table below.

TABLE 3.1: Dimensionless parameters used in the transformed model

Symbol	**Name**	**Definition**
M	Magnetic field parameter	$M = \dfrac{B_0^2 \widetilde{\sigma}_f}{\widetilde{\rho}_f \psi_1 \psi_2}$
K_1	Porosity parameter	$K_1 = \dfrac{\nu_f}{\psi_1 \psi_2 k}$
Pr	Prandtl number	$Pr = \dfrac{(\widetilde{\rho c_p})_f \nu_f}{\widetilde{K}_f}$
R	Radiation parameter	$R = \dfrac{4\sigma^* \mathrm{T}_\infty^3}{k^* \widetilde{K}_f}$
E_c	Eckert number	$E_c = \dfrac{\psi_1^2 \psi_2^2 x^2}{(\widetilde{c}_p)_f (\mathrm{T}_w - \mathrm{T}_\infty)}$
Q	Heat source parameter	$Q = \dfrac{q}{\psi_1 \psi_2 (\widetilde{\rho c_p})_f}$
δ	Thermal relaxation parameter	$\delta = \lambda_1 \psi_1 \psi_2$
β	Solute relaxation time parameter	$\beta = \lambda_2 \psi_1 \psi_2$
Nb	Brownian motion parameter	$Nb = \dfrac{\tau D_B (\mathrm{T}_w - \mathrm{T}_\infty)}{\mathrm{T}_\infty}$
Nt	Thermophoresis parameter	$Nt = \dfrac{\tau D_T (\mathrm{C}_w - \mathrm{C}_\infty)}{v_f \mathrm{T}_\infty}$
Le	Lewis number	$Le = \dfrac{v_f}{D_B}$
Γ	Chemical reaction parameter	$\Gamma = \dfrac{Kr}{\psi_1 \psi_2}$

3.3.1 Non-dimensionalization of Energy Equation

This section focuses on the non-dimensional formulation of the energy equation (3.1). Along with the transformations introduced in Chapter 2, additional derivative expressions are required to carry out this procedure.

$$\frac{\partial^2 \mathrm{T}}{\partial \mathrm{x}^2} = \frac{\partial}{\partial \mathrm{x}} (2b\mathrm{x}\,\theta)$$

$$= 2b\,\theta. \tag{3.5}$$

$$\Rightarrow \frac{\partial^2 \mathrm{T}}{\partial \mathrm{x}\partial \mathrm{y}} = \frac{\partial}{\partial \mathrm{x}}(b\mathrm{x}^2\psi_1\theta')$$

$$= 2b\,\mathrm{x}\psi_1\theta'. \tag{3.6}$$

By substituting the derivatives given in Eqs. (2.6)–(2.10), (2.14)–(2.16), (2.19), (3.5) and (3.6) into (3.1), the following expression is obtained:

$$\begin{aligned}
&2\psi_1\psi_2 b\mathrm{x}^2\,\mathrm{f}'\theta - \psi_1\psi_2 b\mathrm{x}^2 f\theta' + \lambda_1\big[2\psi_1^2\psi_2^2 b\mathrm{x}^2\mathrm{f}'^2\theta + \psi_1^2\psi_2^2 b\mathrm{x}^2\mathrm{f}\,\mathrm{f}'\theta' - \psi_1^2\psi_2^2 b\mathrm{x}^2\mathrm{f}\,\mathrm{f}''\theta \\
&- 4\psi_1^2\psi_2^2 b\mathrm{x}^2\mathrm{f}\,\mathrm{f}'\theta' + 2\psi_1^2\psi_2^2 b\mathrm{x}^2\mathrm{f}'^2\theta + \psi_1^2\psi_2^2 b\mathrm{x}^2\mathrm{f}^2\theta''\big] + \frac{1}{(\widetilde{\rho C}_p)_{hnf}}\frac{16\sigma^*\mathrm{T}_\infty^3}{3k^*} b\mathrm{x}^2\psi_1^2\theta'' \\
&= \frac{\widetilde{K}_{hnf}}{(\widetilde{\rho C}_p)_{hnf}} b\mathrm{x}^2\psi_1^2\theta'' + \frac{\widetilde{\sigma}_{hnf}}{(\widetilde{\rho C}_p)_{hnf}} B_0^2\psi_1^2\psi_2^2\mathrm{x}^2\mathrm{f}'^2 + \frac{\widetilde{\mu}_{hnf}}{(\widetilde{\rho C}_p)_{hnf}}\frac{\psi_1^2\psi_2^2\mathrm{x}^2\mathrm{f}'^2}{k} \\
&+ \frac{q(\mathrm{T}_w - \mathrm{T}_\infty)\theta}{(\widetilde{\rho C}_p)_{hnf}} + \tau\left[D_B\psi_1^2 b\mathrm{x}^2\big(\mathrm{C}_w - \mathrm{C}_\infty\big)\phi'\theta' + \frac{D_T}{T_\infty} b^2\mathrm{x}^4\psi_1^2\theta'^2\right].
\end{aligned}$$

$$\begin{aligned}
\Rightarrow\ & 2\mathrm{f}'\theta - f\theta' + \lambda_1\psi_1\psi_2\big[4\mathrm{f}'^2\theta - 3\mathrm{f}\,\mathrm{f}'\theta' - 2\mathrm{f}\,\mathrm{f}''\theta + \mathrm{f}^2\theta''\big] \\
&= \frac{\widetilde{K}_{hnf}}{(\widetilde{\rho C}_p)_{hnf}}\frac{\psi_1}{\psi_2}\theta'' + \frac{1}{(\widetilde{\rho C}_p)_{hnf}}\frac{16\sigma^*\mathrm{T}_\infty^3}{3k^*}\frac{\psi_1}{\psi_2}\theta'' + \frac{\widetilde{\sigma}_{hnf}}{(\widetilde{\rho C}_p)_{hnf}}\frac{B_0^2\psi_1^2\psi_2^2\mathrm{x}^2\mathrm{f}'^2}{\psi_1\psi_2(\mathrm{T}_w - \mathrm{T}_\infty)} \\
&+ \frac{\widetilde{\mu}_{hnf}}{(\widetilde{\rho C}_p)_{hnf}}\frac{\psi_1^2\psi_2^2\mathrm{x}^2\mathrm{f}'^2}{k\psi_1\psi_2(T_w - T_\infty)} + \frac{q}{(\widetilde{\rho C}_p)_{hnf}}\frac{\theta}{\psi_1\psi_2} \\
&+ \tau\left[\frac{D_B\big(\mathrm{C}_w - \mathrm{C}_\infty\big)\psi_1}{\psi_2}\phi'\theta' + \frac{D_T}{\mathrm{T}_\infty}\frac{\psi_1}{\psi_2}(\mathrm{T}_w - \mathrm{T}_\infty)\theta'^2\right].
\end{aligned}$$

$$\begin{aligned}
\Rightarrow\ & 2\mathrm{f}'\theta - f\theta' + \delta\big[4\mathrm{f}'^2\theta - 3\mathrm{f}\,\mathrm{f}'\theta' - 2\mathrm{f}\,\mathrm{f}''\theta + \mathrm{f}^2\theta''\big] \\
&= \frac{1}{(\widetilde{\rho C}_p)_{hnf}/(\widetilde{\rho C}_p)_f}\frac{1}{(\widetilde{\rho C}_p)_f}\frac{\widetilde{\rho}_f}{\widetilde{\mu}_f}\widetilde{K}_f\left(\frac{\widetilde{K}_{hnf}}{\widetilde{K}_f} + \frac{16\sigma^*}{3k^*\widetilde{K}_f}\,\mathrm{T}_\infty^3\right)\theta'' \\
&+ \frac{\widetilde{\sigma}_{hnf}/\widetilde{\sigma}_f}{(\widetilde{\rho C}_p)_{hnf}/(\widetilde{\rho C}_p)_f}\frac{\widetilde{\sigma}_f}{(\widetilde{\rho C}_p)_f}\frac{B_0^2\psi_1^2\psi_2^2\mathrm{x}^2\mathrm{f}'^2}{\psi_1\psi_2(\mathrm{T}_w - \mathrm{T}_\infty)} \\
&+ \frac{\widetilde{\mu}_{hnf}/\widetilde{\mu}_f}{(\widetilde{\rho C}_p)_{hnf}/(\widetilde{\rho C}_p)_f}\frac{\widetilde{\mu}_f}{(\widetilde{\rho C}_p)_f}\frac{\psi_1^2\psi_2^2\mathrm{x}^2\mathrm{f}'^2}{k\psi_1\psi_2(T_w - T_\infty)} + \frac{\tau D_B\big(\mathrm{C}_w - \mathrm{C}_\infty\big)}{v_f}\phi'\theta' \\
&+ \frac{q}{(\widetilde{\rho C}_p)_{hnf}/(\widetilde{\rho C}_p)_f}\frac{1}{(\widetilde{\rho C}_p)_f}\frac{\theta}{\psi_1\psi_2} + \frac{\tau D_T}{\mathrm{T}_\infty}\frac{(\mathrm{T}_w - \mathrm{T}_\infty)}{v_f}\theta'^2.
\end{aligned}$$

$$\begin{aligned}
\Rightarrow\quad & 2\mathrm{f}'\theta - f\theta' + \delta\big[4\mathrm{f}'^2\theta - 3\mathrm{f}\,\mathrm{f}'\theta' - 2\mathrm{f}\,\mathrm{f}''\theta + \mathrm{f}^2\theta''\big] = \frac{1}{P_5 Pr}\left(P_3 + \frac{4R}{3}\right)\theta'' \\
&+ \frac{P_4}{P_5}ME_c\,\mathrm{f}'^2 + \frac{P_1}{P_5}K_1E_c\,\mathrm{f}'^2 + \frac{1}{P_5}Q\theta + N_b\,\phi'\theta' + N_t\,\theta'^2.
\end{aligned}$$

$$\Rightarrow \frac{1}{P_5 Pr}\left(P_3+\frac{4R}{3}\right)\theta''+\frac{E_c}{P_5}\left(P_4 M\,\mathrm{f}'^2+P_1\right)\mathrm{f}'^2+\frac{1}{P_5}Q\theta+N_b\,\phi'\theta'+N_t\,\theta'^2$$
$$-2\mathrm{f}'\theta\ +f\theta'-\delta\left[4\mathrm{f}'^2\theta-3\mathrm{f}\,\mathrm{f}'\theta'-2\mathrm{f}\,\mathrm{f}''\theta+\mathrm{f}^2\theta''\right]=0. \tag{3.7}$$

3.3.2 Non-dimensionalization of Concentration Equation

The present section focuses on constructing a dimensionless form of the concentration equation (3.2) relevant to the hybrid nanofluid system. The supporting derivative expressions are introduced next.

$$\phi(\eta)=\frac{\mathrm{C}-\mathrm{C}_\infty}{\mathrm{C}_w-\mathrm{C}_\infty}.$$
$$\Rightarrow \quad \mathrm{C}=\phi\left(\mathrm{C}_w-\mathrm{C}_\infty\right)+\mathrm{C}_\infty. \tag{3.8}$$
$$\Rightarrow \quad \frac{\partial \mathrm{C}}{\partial \mathrm{x}}=2b\mathrm{x}\phi. \tag{3.9}$$
$$\Rightarrow \quad \frac{\partial^2 \mathrm{C}}{\partial \mathrm{x}^2}=2b\phi. \tag{3.10}$$
$$\Rightarrow \quad \frac{\partial \mathrm{C}}{\partial \mathrm{y}}=b\mathrm{x}^2\psi_1\phi'. \tag{3.11}$$
$$\Rightarrow \quad \frac{\partial^2 \mathrm{C}}{\partial \mathrm{y}^2}=b\mathrm{x}^2\psi_1^2\phi''. \tag{3.12}$$
$$\Rightarrow \quad \frac{\partial^2 \mathrm{C}}{\partial \mathrm{x}\partial y}=2b\mathrm{x}\psi_1\phi'. \tag{3.13}$$

By inserting the partial derivatives given in Eqs. (3.9)–(3.13) into (3.2), the following expression is obtained:

$$-\psi_1\psi_2 b\mathrm{x}^2 f\phi'+2\psi_1\psi_2 b\mathrm{x}^2\,\mathrm{f}'\phi+\lambda_2\left[2\psi_1^2\psi_2^2 b\mathrm{x}^2\mathrm{f}'^2\phi+\psi_1^2\psi_2^2 b\mathrm{x}^2\mathrm{f}\,\mathrm{f}'\phi'\right.$$
$$\left.-2\psi_1^2\psi_2^2 b\mathrm{x}^2\mathrm{f}\,\mathrm{f}''\phi-4\psi_1^2\psi_2^2 b\mathrm{x}^2\mathrm{f}\,\mathrm{f}'\phi'+2\psi_1^2\psi_2^2 b\mathrm{x}^2\mathrm{f}'^2\phi+\psi_1^2\psi_2^2 b\mathrm{x}^2\mathrm{f}^2\phi''\right]$$
$$=D_B\psi_1^2 b\mathrm{x}^2\phi''+\frac{D_T}{\mathrm{T}_\infty}(\mathrm{T}_w-\mathrm{T}_\infty)\psi_1^2\theta''-K_r\left[\phi(\mathrm{C}_w-\mathrm{C}_\infty)+\mathrm{C}_\infty-\mathrm{C}_\infty\right].$$

$$\Rightarrow \quad -f\phi'+2\mathrm{f}'\phi+\frac{\lambda_2\psi_1^2\psi_2^2 b\mathrm{x}^2}{\psi_1\psi_2 b\mathrm{x}^2}\left[4\mathrm{f}'^2\phi-3\mathrm{f}\,\mathrm{f}'\phi'-2\mathrm{f}\,\mathrm{f}''\phi+\mathrm{f}^2\phi''\right]=\frac{D_B\psi_1^2 b\mathrm{x}^2}{\psi_1\psi_2 b\mathrm{x}^2}\phi''$$
$$+\frac{D_T}{\mathrm{T}_\infty}\frac{\psi_1^2(\mathrm{T}_w-\mathrm{T}_\infty)}{\psi_1\psi_2 b\mathrm{x}^2}\theta''-\frac{K_r(\mathrm{C}_w-\mathrm{C}_\infty)}{\psi_1\psi_2 b\mathrm{x}^2}\phi.$$

$$\Rightarrow \quad -f\phi' + 2\mathrm{f}'\phi + \lambda_2\psi_1\psi_2\big[4\mathrm{f}'^2\phi - 3\mathrm{f}\,\mathrm{f}'\phi' - 2\mathrm{f}\,\mathrm{f}''\phi + \mathrm{f}^2\phi''\big] = \frac{D_B\psi_1}{\psi_2}\phi'' + \frac{D_T}{T_\infty}\frac{\psi_1(\mathrm{T}_w - \mathrm{T}_\infty)}{\psi_2(\mathrm{C}_w - \mathrm{C}_\infty)}\theta'' - \frac{K_r}{\psi_1\psi_2}\phi.$$

$$\Rightarrow \quad -f\phi' + 2\mathrm{f}'\phi + \beta\big[4\mathrm{f}'^2\phi - 3\mathrm{f}\,\mathrm{f}'\phi' - 2\mathrm{f}\,\mathrm{f}''\phi + \mathrm{f}^2\phi''\big] = \frac{D_B}{v_f}\phi'' - \frac{K_r}{\psi_1\psi_2}\phi + \frac{D_T}{\mathrm{T}_\infty}\frac{(\mathrm{T}_w - \mathrm{T}_\infty)}{(\mathrm{C}_w - \mathrm{C}_\infty)}\frac{1}{v_f}\theta''.$$

$$\Rightarrow \quad -f\phi' + 2\mathrm{f}'\phi + \beta\big[4\mathrm{f}'^2\phi - 3\mathrm{f}\,\mathrm{f}'\phi' - 2\mathrm{f}\,\mathrm{f}''\phi + \mathrm{f}^2\phi''\big] = \frac{D_B}{v_f}\left[\phi'' - \frac{K_r}{\psi_1\psi_2}\frac{v_f}{D_B}\phi + \frac{D_T}{\mathrm{T}_\infty D_B}\frac{(\mathrm{T}_w - \mathrm{T}_\infty)}{(\mathrm{C}_w - \mathrm{C}_\infty)}\theta''\right].$$

$$\Rightarrow \quad -f\phi' + 2\mathrm{f}'\phi + \beta\big[4\mathrm{f}'^2\phi - 3\mathrm{f}\,\mathrm{f}'\phi' - 2\mathrm{f}\,\mathrm{f}''\phi + \mathrm{f}^2\phi''\big] = \frac{1}{Le}\left(\phi'' + \frac{N_t}{N_b}\theta'' - \Gamma Le\phi\right).$$

$$\Rightarrow \quad \phi'' + \frac{N_t}{N_b}\theta'' - \beta Le\big[4\mathrm{f}'^2\phi - 3\mathrm{f}\,\mathrm{f}'\phi' - 2\mathrm{f}\,\mathrm{f}''\phi + \mathrm{f}^2\phi''\big] - \Gamma Le\phi + Le\,\mathrm{f}\phi' - 2Le\,\mathrm{f}'\phi = 0. \tag{3.14}$$

3.3.3 Dimensionless form of Boundary Conditions

- $\mathrm{C} = \mathrm{C}_w = \mathrm{C}_\infty + b\mathrm{x}^2, \qquad at \quad \mathrm{y} = 0.$

  $\Rightarrow \quad \phi(\eta)(\mathrm{C}_w - \mathrm{C}_\infty) + \mathrm{C}_\infty = \mathrm{C}_\infty + b\mathrm{x}^2, \qquad at \quad \eta = 0.$

  $\Rightarrow \quad \phi = \dfrac{b\mathrm{x}^2}{\mathrm{C}_w - \mathrm{C}_\infty}, \qquad at \quad \eta = 0.$

  $\Rightarrow \quad \phi = 1, \qquad at \quad \eta = 0.$

- $\mathrm{C} \longrightarrow \mathrm{C}_\infty, \qquad as \quad \mathrm{y} \longrightarrow \infty.$

  $\Rightarrow \quad \mathrm{C}_\infty + \big(\mathrm{C}_w - \mathrm{C}_\infty\big)\phi \longrightarrow \mathrm{C}_\infty, \qquad as \quad \eta \longrightarrow \infty.$

  $\Rightarrow \quad \phi \longrightarrow 0, \qquad as \quad \eta \longrightarrow \infty.$

3.4 Solution Framework

The numerical solution of the coupled governing equations (3.7) and (3.14) is carried out using the shooting method combined with a fourth-order Runge–Kutta algorithm. The known values of f, f′, and f″ obtained earlier are employed within the computational procedure. To support the numerical implementation, the following notations are introduced.

$$\theta = \widetilde{z}_1, \qquad \theta' = \widetilde{z}_1' = \widetilde{z}_2, \qquad \phi = \widetilde{z}_3, \qquad \phi' = \widetilde{z}_3' = \widetilde{z}_4.$$

and

$$a_1 = \frac{1}{P_5 Pr}\left(P_3 + \frac{4R}{3} - \delta \mathrm{f}^2\right), \qquad a_2 = \frac{1}{1 - \beta Le \mathrm{f}^2}$$

The system of equations can be represented in the form of the following first-order coupled ODEs:

$$\begin{aligned}
&\widetilde{z}_1' = \widetilde{z}_2, && \widetilde{z}_1(0) = 1,\\
&\widetilde{z}_2' = \frac{-1}{a_1}\Bigg[\frac{Q}{P_5}\widetilde{z}_1 + N_b \widetilde{z}_2 \widetilde{z}_4 + N_t \widetilde{z}_2^2 - 2\mathrm{f}'\widetilde{z}_1 + \mathrm{f}\widetilde{z}_2 \\
&\qquad - \delta(4\mathrm{f}'^2\widetilde{z}_1 - 3\mathrm{f}\,\mathrm{f}'\widetilde{z}_2 - 2\mathrm{f}\,\mathrm{f}''\widetilde{z}_1) + \frac{E_c(P_4 M + P_1 K_1)}{P_5}\mathrm{f}'^2\Bigg], && \widetilde{z}_2(0) = \tilde{p},\\
&\widetilde{z}_3' = \widetilde{z}_4, && \widetilde{z}_3(0) = 1,\\
&\widetilde{z}_4' = a_2\Bigg[(\Gamma Le + 2Le\mathrm{f}')\widetilde{z}_3 - Le\mathrm{f}\widetilde{z}_4 - \frac{Nt}{Nb}\widetilde{z}_2' + \beta Le(4\mathrm{f}'^2 - 2\mathrm{f}\,\mathrm{f}'')\widetilde{z}_3 \\
&\qquad - 3Le\beta \mathrm{f}\,\mathrm{f}'\widetilde{z}_4\Bigg], && \widetilde{z}_4(0) = \tilde{q}.
\end{aligned}$$

To implement the fourth-order RK4 method for solving the above initial value problem, appropriate values of the unknown parameters $\tilde{p}$ and $\tilde{q}$ are required. These missing conditions are selected such that the numerical solution converges to the prescribed boundary conditions, which are expressed as:

$$\widetilde{z}_1(\eta_\infty, \tilde{p}, \tilde{q}) = 0, \qquad \widetilde{z}_3(\eta_\infty, \tilde{p}, \tilde{q}) = 0.$$

The resulting system of nonlinear algebraic equations is solved using Newton's iterative method, which is implemented according to the following computational

procedure.

$$\begin{bmatrix}\tilde{p}\\ \tilde{q}\end{bmatrix}^{(n+1)} = \begin{bmatrix}\tilde{p}\\ \tilde{q}\end{bmatrix}^{(n)} - \left(\begin{bmatrix}\frac{\partial \widetilde{z}_1}{\partial \tilde{p}} & \frac{\partial \widetilde{z}_1}{\partial \tilde{q}}\\ \frac{\partial \widetilde{z}_3}{\partial \tilde{p}} & \frac{\partial \widetilde{z}_3}{\partial \tilde{q}}\end{bmatrix}^{-1}\begin{bmatrix}\widetilde{z}_1\\ \widetilde{z}_3\end{bmatrix}\right)^{(n)}.$$

To proceed further the following new notations have been introduced:

$$\begin{aligned}&\frac{\partial \widetilde{z}_1}{\partial \tilde{p}} = \widetilde{z}_5, \quad \frac{\partial \widetilde{z}_2}{\partial \tilde{p}} = \widetilde{z}_6, \quad \frac{\partial \widetilde{z}_3}{\partial \tilde{p}} = \widetilde{z}_7, \quad \frac{\partial \widetilde{z}_4}{\partial \tilde{p}} = \widetilde{z}_8,\\ &\frac{\partial \widetilde{z}_1}{\partial \tilde{q}} = \widetilde{z}_9, \quad \frac{\partial \widetilde{z}_2}{\partial \tilde{q}} = \widetilde{z}_{10}, \quad \frac{\partial \widetilde{z}_3}{\partial \tilde{q}} = \widetilde{z}_{11}, \quad \frac{\partial \widetilde{z}_4}{\partial \tilde{q}} = \widetilde{z}_{12}.\end{aligned}$$

As a result of these new notations, the Newton's iterative scheme takes the following form:

$$\begin{bmatrix}\tilde{p}\\ \tilde{q}\end{bmatrix}^{(n+1)} = \begin{bmatrix}\tilde{p}\\ \tilde{q}\end{bmatrix}^{(n)} - \left(\begin{bmatrix}\widetilde{z}_5 & \widetilde{z}_9\\ \widetilde{z}_7 & \widetilde{z}_{11}\end{bmatrix}^{-1}\begin{bmatrix}\widetilde{z}_1\\ \widetilde{z}_3\end{bmatrix}\right)^{(n)}. \tag{3.15}$$

Differentiation with respect to $\tilde{p}$ and $\tilde{q}$ yields a corresponding system of ODEs.

$$\begin{aligned}
&\widetilde{z}_5' = \widetilde{z}_6, && \widetilde{z}_5(0) = 0,\\
&\widetilde{z}_6' = \frac{-1}{a_1}\Big[\frac{Q}{P_5}\widetilde{z}_5 + N_b(\widetilde{z}_2\widetilde{z}_8 + \widetilde{z}_6\widetilde{z}_4) + 2N_t\widetilde{z}_2\widetilde{z}_6 - 2\mathrm{f}'\widetilde{z}_5 + \mathrm{f}\widetilde{z}_6\\
&\qquad - \delta(4\mathrm{f}'^2\widetilde{z}_5 - 3\mathrm{f}\,\mathrm{f}'\widetilde{z}_6 - 2\mathrm{f}\,\mathrm{f}''\widetilde{z}_5)\Big], && \widetilde{z}_6(0) = 1,\\
&\widetilde{z}_7' = \widetilde{z}_8, && \widetilde{z}_7(0) = 0,\\
&\widetilde{z}_8' = a_2\Big[(\Gamma Le + 2Le\mathrm{f}')\widetilde{z}_7 - Le\mathrm{f}\widetilde{z}_8 - \frac{Nt}{Nb}\widetilde{z}_6' + \beta Le(4\mathrm{f}'^2 - 2\mathrm{f}\,\mathrm{f}'')\widetilde{z}_7\\
&\qquad - 3Le\beta\mathrm{f}\,\mathrm{f}'\widetilde{z}_8\Big], && \widetilde{z}_8(0) = 0,\\
&\widetilde{z}_9' = \widetilde{z}_{10}, && \widetilde{z}_9(0) = 0,\\
&\widetilde{z}_{10}' = \frac{-1}{a_1}\Big[\frac{Q}{P_5}\widetilde{z}_9 + N_b(\widetilde{z}_2\widetilde{z}_{12} + \widetilde{z}_{10}\widetilde{z}_4) + 2N_t\widetilde{z}_2\widetilde{z}_{10} - 2\mathrm{f}'\widetilde{z}_9 + \mathrm{f}\widetilde{z}_{10}\\
&\qquad - \delta(4\mathrm{f}'^2\widetilde{z}_9 - 3\mathrm{f}\,\mathrm{f}'\widetilde{z}_{10} - 2\mathrm{f}\,\mathrm{f}''\widetilde{z}_9)\Big], && \widetilde{z}_{10}(0) = 0,\\
&\widetilde{z}_{11}' = \widetilde{z}_{12}, && \widetilde{z}_{11}(0) = 0,\\
&\widetilde{z}_{12}' = a_2\Big[(\Gamma Le + 2Le\mathrm{f}')\widetilde{z}_{11} - Le\mathrm{f}\widetilde{z}_{12} - \frac{Nt}{Nb}\widetilde{z}_{10}' + \beta Le(4\mathrm{f}'^2 - 2\mathrm{f}\,\mathrm{f}'')\widetilde{z}_{11}\\
&\qquad - 3Le\beta\mathrm{f}\,\mathrm{f}'\widetilde{z}_12\Big], && \widetilde{z}_{12}(0) = 1.
\end{aligned}$$

Newton's iterative procedure is terminated when the following condition is satisfied:

$$max\left\{\left|\widetilde{z}_1\left(\eta_\infty, \tilde{p}, \tilde{q}\right)\right|, \left|\widetilde{z}_3\left(\eta_\infty, \tilde{p}, \tilde{q}\right)\right|\right\} < \epsilon.$$

where $\epsilon > 0$ is an arbitrarily small positive number and has been taken as 10^{-9}.

3.5 Results and Discussion

The computed solutions of the reduced ODE system highlight important nondimensional parameters that influence the flow structure. Graphs and numerical tables are employed to investigate how these parameters modify the temperature and concentration distributions.. A physical explanation is also presented to describe the role of each parameter in controlling heat and mass transport within the system, leading to a clearer understanding of the underlying transport processes.

3.5.1 Analysis of Computational Results

Tables 3.2 and 3.3 presents the numerical variation of the local Nusselt number and Sherwood number for different values of the governing parameters, while the remaining parameters are kept fixed. The table also reports the corresponding intervals of validity for the temperature and concentration profiles, which confirm the numerical stability of the obtained solutions.

The results in Table 3.2 show that raising the magnetic parameter by approximately 25–60% causes a 3–5.5% reduction in Nu_x, attributed to enhanced magnetic resistance to heat transfer near the surface, while Sh_x rises by about 5–7%. In contrast, a comparable variation in K_1 of roughly 25–67% leads to a 3.8–32.7% decrease in Nu_x and a 4.5–7.1% enhancement in Sh_x, as higher permeability promotes fluid penetration within the porous medium, weakens thermal gradients and strengthens concentration transport near the wall. From Table 3.3, it is evident that the heat generation parameter Q has a strong influence on surface heat transfer. Increasing Q from 0.2 to 1.5 leads to a 36.2% reduction in the Nu_x, while the

Sh_x increases by approximately 50–80%, indicating enhanced mass transfer. Similarly, varying the chemical reaction parameter Γ from 0.1 to 1.0 leads to an 18.9% decrease in the Nu_x, reflecting weakened surface heat transfer due to stronger reaction effects, while the Sh_x increases by approximately 46–81%.

Likewise, a 50% rise in the Lewis number Le results in a 16% reduction in the Nu_x, indicating weakened surface heat transfer. In contrast, the Sh_x increases by up to 89% and continues to rise with increasing Le, reflecting the growing dominance of diffusive transport.

TABLE 3.2: Variation of Nu_x and Sh_x along with the intervals of validity I_θ and I_ϕ for $N_t = N_b = 0.3$, $E_c = Q = 0.5$, $Le = 1$ and $\Gamma = 0.1$.

M	ϕ_1	ϕ_2	K_1	f_w	Pr	R	Nu_x	Sh_x	I_θ	I_ϕ
0.5	0.02	0.02	0.5	0.5	21	1	3.60165	-1.23874	[-4.43, -1.30]	[1.20, 1.50]
0							3.99923	-1.42359	[-4.00, -1.80]	[0.31, 0.71]
0.3							3.74913	-1.30662	[-4.30, -1.70]	[1.00, 1.70]
0.8							3.40443	-1.14906	[-4.00, -1.00]	[0.80, 2.20]
1							3.28658	-1.09595	[-4.00, -1.00]	[0.96, 3.28]
	0						3.71729	-1.19700	[-4.20, -1.96]	[0.80, 1.90]
	0.01						3.65876	-1.22093	[-4.27, -1.80]	[0.90, 2.04]
	0.03						3.54575	-1.25120	[-4.09, -1.25]	[0.80, 2.01]
	0.05						3.43686	- 1.26261	[-4.28, -1.00]	[1.20, 2.68]
		0					3.70387	-1.27163	[-3.98, -2.08]	[0.49, 2.63]
		0.01					3.65254	-1.25565	[-4.10, -2.20]	[0.70, 3.10]
		0.03					3.55118	-1.22095	[-4.00, -2.10]	[0.65, 3.39]
		0.1					3.20763	-1.07661	[-4.20, -2.00]	[1.18, 4.82]
			0				3.99131	-1.41985	[-4.20, -2.34]	[0.60, 1.91]
			0.3				3.74640	-1.30536	[-4.10, -2.00]	[0.64, 2.23]
			0.8				3.40770	-1.15053	[-4.40, -2.10]	[1.29, 4.33]
			1				3.29158	-1.09820	[-4.00, -1.20]	[0.83, 3.60]
				-0.2			1.53945	0.57857	[-4.10, -2.00]	[0.60, 2.83]
				0			1.87048	0.33218	[-3.80, -1.80]	[1.63, 3.88]
				0.3			2.68260	-0.36560	[-4.00, -2.50]	[1.15, 5.23]
				0.7			5.18623	-2.85759	[-4.54, -2.40]	[0.70, 2.79]
					10		2.84890	-0.52880	[-4.10, -1.00]	[0.56, 6.42]
					17		3.86934	-1.495324	[-4.25, -2.00]	[0.99, 1.72]
					20		4.24831	-1.86144	[-3.80, -2.40]	[0.43, 1.21]
						1.5	3.13747	-0.79864	[-4.20, -1.00]	[0.79, 4.00]
						2	2.80266	-0.48587	[-4.30, -1.10]	[0.83, 7.00]
						2.5	2.54488	-0.24832	[-4.00, -1.00]	[0.31, 9.42]
						3	2.33745	-0.05961	[-4.20, -0.50]	[0.51, 10.79]

TABLE 3.3: Variation of Nu_x, Sh_x along with interval of validity I_θ and I_ϕ, when $M = K_1 = f_w = 0.5, \phi_1 = \phi_2 = 0.02$ and $Pr = 21$

Q	E_c	N_t	N_b	Γ	Le	Nu_x	Sh_x	I_θ	I_ϕ
0.5	0.5	0.3	0.3	0.1	1	3.60165	-1.23874	[-4.43, -1.30]	[1.20, 1.50]
0.2						3.87491	-1.50502	[-4.13, -3.53]	[0.99, 2.60]
1						3.09148	-0.74440	[-4.00, -2.00]	[0.47, 25.97]
1.5						2.47337	-0.15120	[-4.00, -2.00]	[0.38, 3.22]
	0					4.17532	-1.79011	[-4.42, -2.04]	[0.99, 2.02]
	0.3					3.83207	-1.46025	[-4.27, -2.50]	[0.90, 3.53]
	0.7					3.36995	-1.01594	[-4.23, -2.10]	[1.00, 3.53]
		0.1				4.24166	0.58246	[-6.01, -1.00]	[-1.77, 16.01]
		0.2				3.90476	-0.41995	[-4.50, -2.00]	[-0.56, 6.73]
		0.4				3.33093	-1.90665	[-3.60, -2.40]	[1.48, 2.31]
			0.1			4.83249	-10.96874	[-3.52, -1.20]	[1.00, 20.10]
			0.4			3.09024	-0.10333	[-4.10, -2.29]	[0.41, 1.52]
			0.5			2.64613	0.53626	[-4.30, -2.98]	[0.37, 1.40]
				0.5		3.33388	-0.66338	[-4.43, -2.30]	[0.94, 4.87]
				1		3.09855	-0.12524	[-4.10, -2.70]	[0.18, 2.92]
				1.5		2.92187	0.30316	[-4.34, -2.50]	[0.10, 1.39]
					1.5	2.99238	-0.13071	[-4.35, -2.90]	[0.98, 2.05]
					2	2.58626	1.22577	[-4.30, -3.10]	[0.78, 1.58]
					2.5	2.29450	2.16794	[-4.30, -3.20]	[0.70, 1.49]

3.5.2 Temperature Profile

Figures 3.2 to 3.7 depict the variation of temperature distribution $\theta(\eta)$ under different physical parameters for the hybrid nanofluid (Cu–Al_2O_3/kerosene oil) with volume fraction $\phi_1 + \phi_2 = 0.04$ and the Al_2O_3/kerosene oil nanofluid. In all cases, the hybrid fluid shows comparatively higher temperature distributions, confirming improved thermal performance.

Figure 3.2 shows that the temperature profile rises due to enhanced viscous dissipation, which converts the kinetic energy of the flow into thermal energy. As

a consequence, additional heat is produced within the fluid domain, thereby increasing the temperature throughout the boundary layer.

The effect of internal heat generation on the temperature profile is shown in Figure 3.3. Higher values of Q supply additional thermal energy within the fluid, leading to an overall rise in temperature throughout the boundary layer. As a result, the temperature decays more gradually away from the surface due to the presence of internally generated heat.

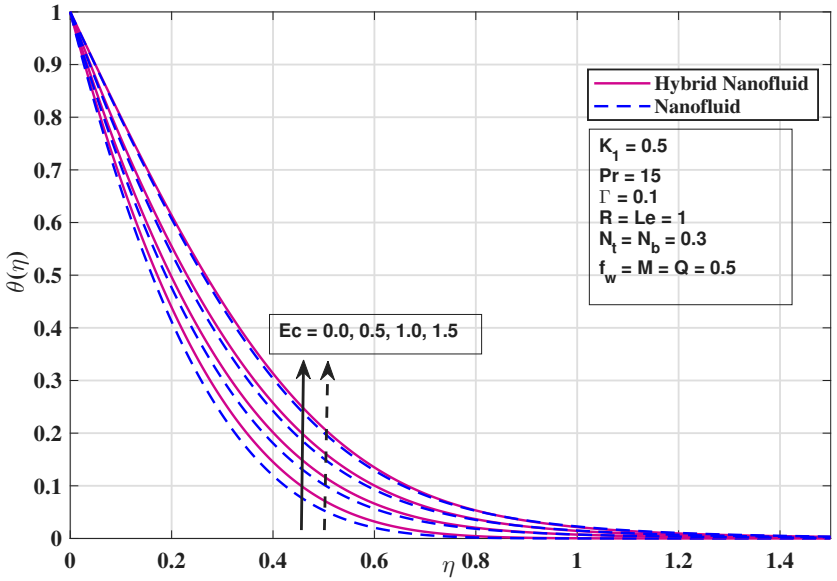

FIGURE 3.2: Variation of E_c on θ

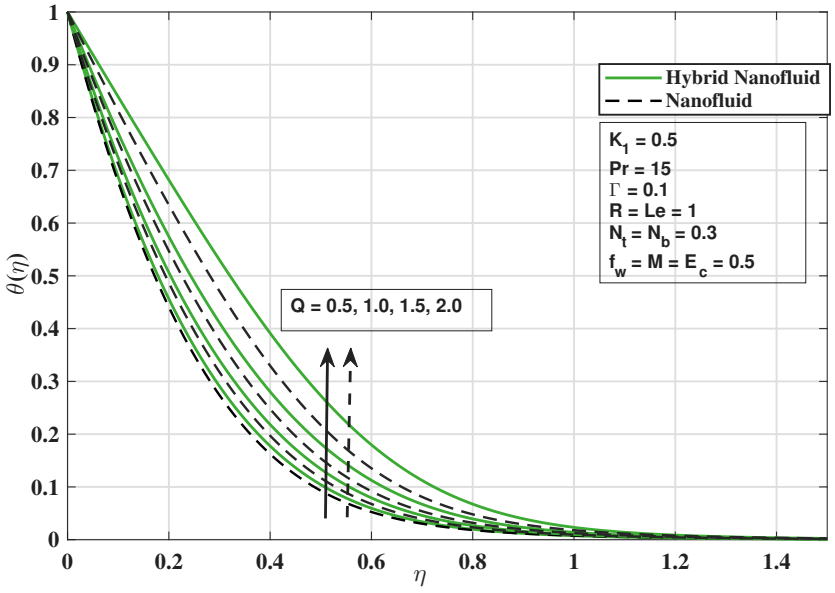

FIGURE 3.3: Variation of Q on θ

In Figure 3.4, it is evident that an enhancement in N_t parameter causes rise in temperature throughout the boundary layer. Physically, thermophoresis causes nanoparticles to migrate from regions of higher temperature near the wall toward cooler regions away from the surface. This movement of nanoparticles carries thermal energy into the fluid, leading to an accumulation of heat within the boundary layer. The fluid therefore maintains higher thermal energy, producing a stronger temperature distribution.

Figure 3.5 shows that increasing parameter N_b leads to higher temperature distribution. This is because stronger random motion of nanoparticles enhances energy transfer within the fluid. As a result, more heat is retained within the boundary layer, causing an overall rise in the temperature profile.

In Figure 3.6 the temperature field is found to decline with increasing Prandtl number. This trend arises because higher Prandtl values correspond to lower thermal diffusivity, limiting the spread of heat from the surface into the fluid. Consequently, the thermal boundary layer contracts, resulting in reduced temperatures throughout the flow region.

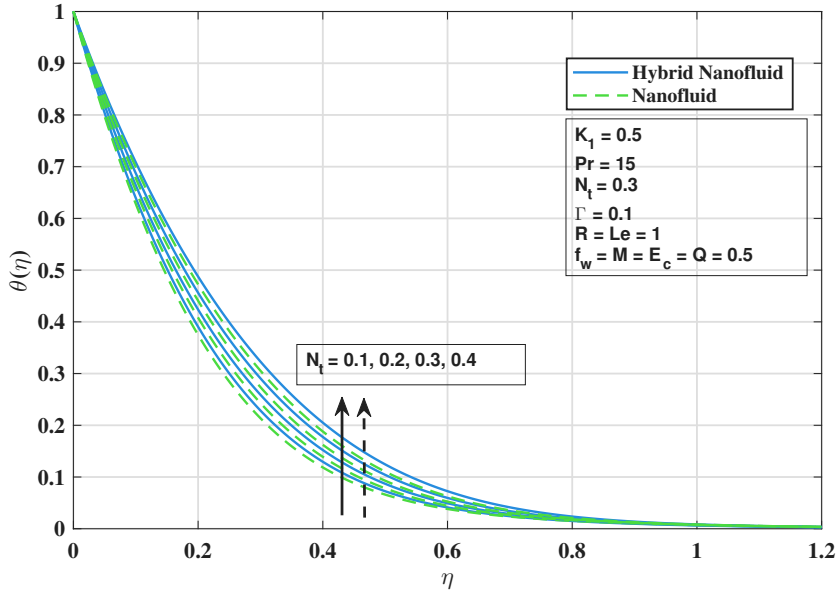

FIGURE 3.4: Variation of N_t on θ

Figure 3.7 illustrates the influence of the Al_2O_3 on the temperature profile $\theta(\eta)$.

It is observed that increasing ϕ_1 leads to higher temperature levels for both the nanofluid and the hybrid nanofluid. This behavior arises because the addition of Al_2O_3 nanoparticles enhances the effective thermal conductivity, enabling the fluid to store and transport more heat. In the hybrid nanofluid case, where the copper volume fraction is fixed at $\phi_2 = 0.01$, the temperature profile remains slightly higher than that of the single-component nanofluid, demonstrating the improved thermal performance due to the combined nanoparticle effect.

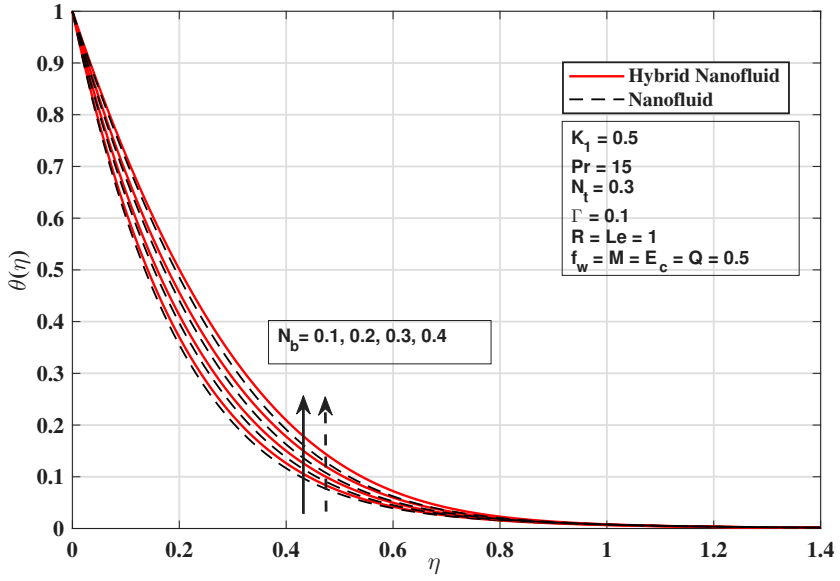

FIGURE 3.5: Variation of N_b on θ

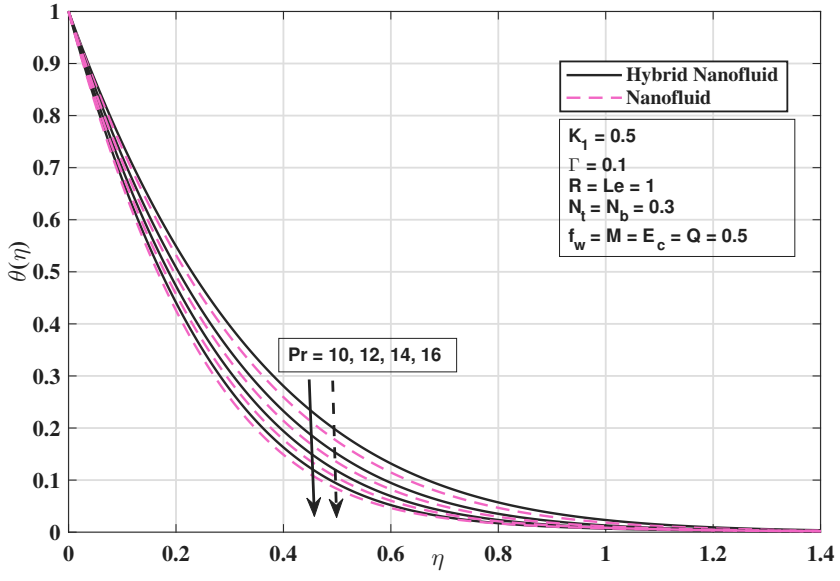

FIGURE 3.6: Variation of Pr on θ

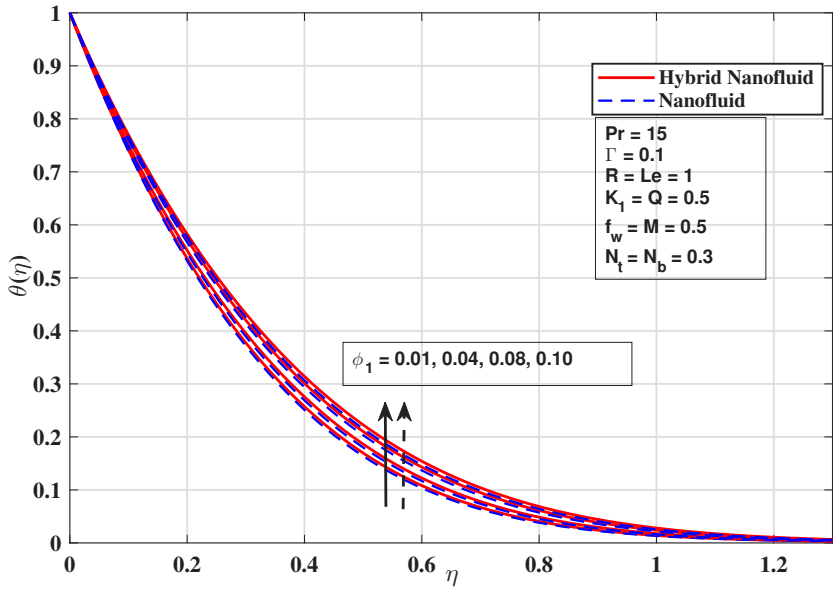

FIGURE 3.7: Variation of ϕ_1 on θ

3.5.3 Concentration Profile

Figure 3.8 shows that increasing the Lewis number reduces the concentration profile for both fluids due to weakened mass diffusion. This restricts the spread of nanoparticles within the boundary layer, leading to reduced concentration of suspended particles throughout the fluid domain.

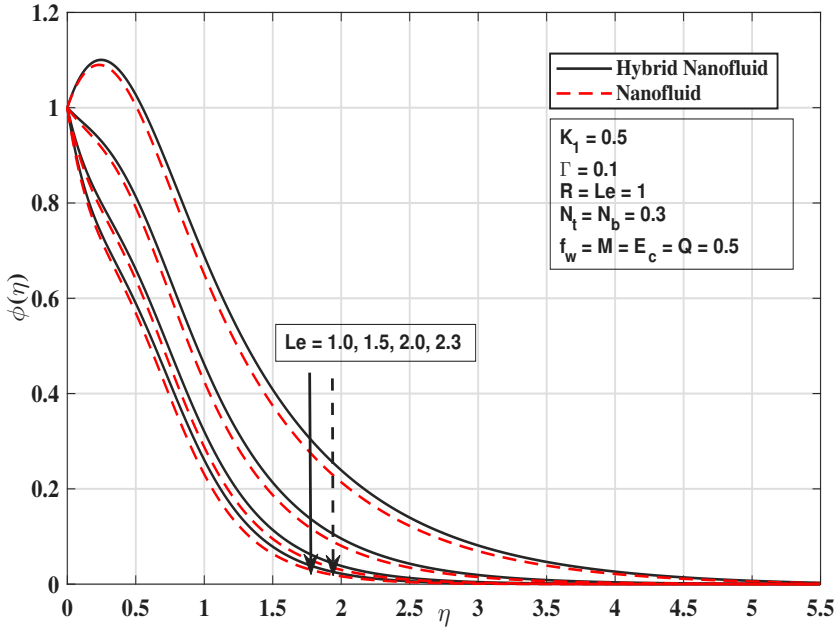

FIGURE 3.8: Variation of Le on $\phi(\eta)$

As shown in Figure 3.9, higher values of the chemical reaction parameter Γ lead to a faster decline in the concentration profile. This occurs because stronger chemical reactions accelerate nanoparticles depletion near the wall, resulting in lower concentration values across the fluid domain.

As N_t increases, nanoparticles are driven away from the heated surface toward cooler regions, leading to higher concentration levels within the boundary layer. This enhances mass transport and causes the concentration profile $\phi(\eta)$ to decay more slowly with η, as illustrated in the Figure 3.10.

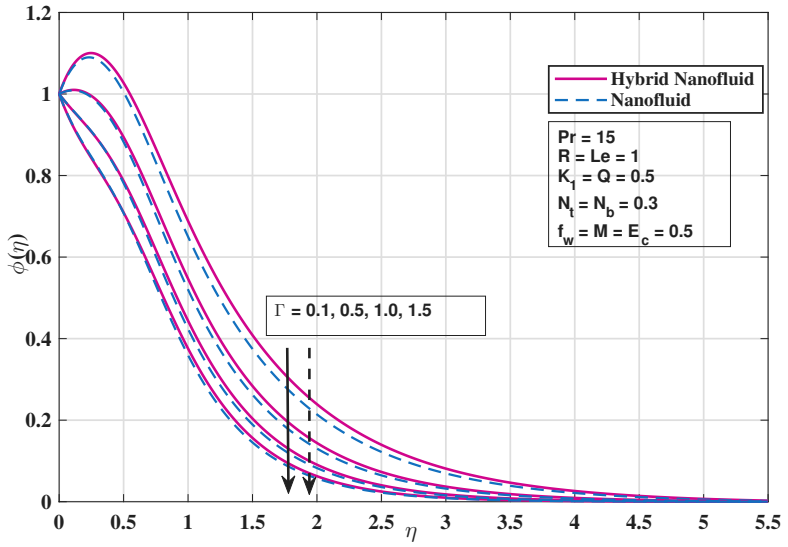

FIGURE 3.9: Variation of Γ on $\phi(\eta)$

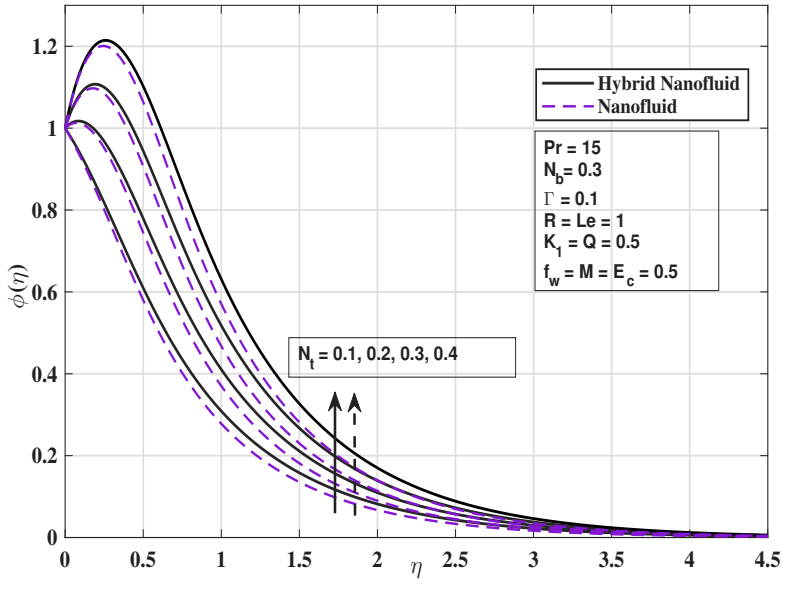

FIGURE 3.10: Variation of N_t on $\phi(\eta)$

Figure 3.11 presents the effect of parameter N_b on the concentration profile. As N_b increases, the random movement of nanoparticles becomes more intense, which enhances their diffusion away from the surface. This redistribution lowers the concentration near the wall and causes the profile to decay more rapidly across the flow region.

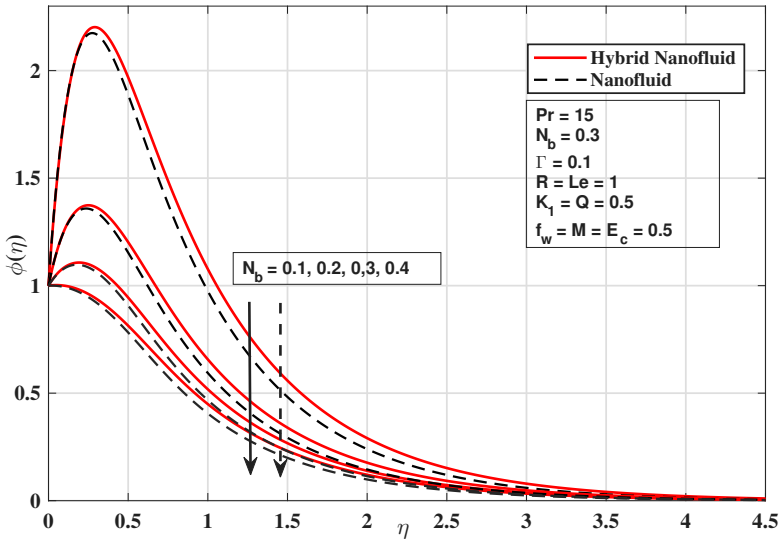

FIGURE 3.11: Variation of N_b on $\phi(\eta)$

Chapter 4

Electro-Magneto Marangoni Flow with Non-Darcy Forchheimer Resistance and Higher Order Reaction Effects

4.1 Introduction

The present chapter extends the model developed in Chapter 3 by incorporating additional physical effects to achieve a more comprehensive description of the transport processes in the hybrid nanofluid system.

The formulation is augmented by introducing the effect of an applied electric field together with Non-Darcy Forchheimer to represent both viscous and inertial resistance within the porous medium. The concentration equation is further refined by including a higher-order chemical reaction term.

These modifications enable a more detailed assessment of the combined electromagnetic thermal and diffusion phenomenon influencing Marangoni-driven hybrid nanofluid flow.

4.2 Physical Model

In the present formulation, a uniform electric field aligned with the magnetic field is incorporated along with non-inertial effects and a higher-order chemical reaction, while all geometric and material properties are retained from the previous chapter.

The combined electromagnetic action modifies the momentum and transport mechanisms through electric forcing and magnetic damping, whereas non-inertial effects influence the flow resistance.

The higher-order chemical reaction strengthens the coupling between concentration, temperature and velocity fields. The modified governing equations are given in equations (4.1)–(4.2), with boundary conditions adopted from (3.3)[31, 32].

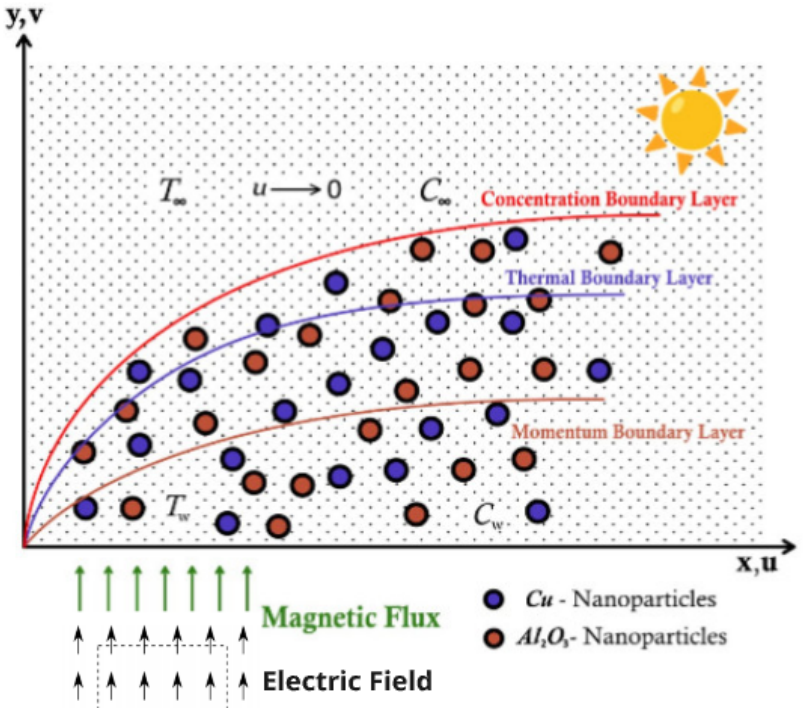

FIGURE 4.1: Flow Configuration

4.2.1 Momentum Equation

$$\mathrm{u}\frac{\partial \mathrm{u}}{\partial \mathrm{x}} + \mathrm{v}\frac{\partial \mathrm{u}}{\partial \mathrm{y}} + \frac{\widetilde{\sigma}_{hnf}}{\widetilde{\rho}_{hnf}} B_0(B_0\mathrm{u} - E_0) + \frac{\widetilde{\mu}_{hnf}}{\widetilde{\rho}_{hnf}}\frac{\mathrm{u}}{k}$$

$$= \frac{\mu_{hnf}}{\rho_{hnf}}\frac{\partial^2 \mathrm{u}}{\partial \mathrm{y}^2} - \frac{\omega}{\sqrt{k}}\mathrm{u}^2. \tag{4.1}$$

4.2.2 Energy Equation

$$\mathrm{u}\frac{\partial \mathrm{T}}{\partial \mathrm{x}}+\mathrm{v}\frac{\partial \mathrm{T}}{\partial \mathrm{y}}+\lambda_1\left(\mathrm{u}\frac{\partial \mathrm{u}}{\partial \mathrm{v}}\frac{\partial \mathrm{T}}{\partial \mathrm{x}}+\mathrm{v}\frac{\partial \mathrm{v}}{\partial \mathrm{y}}\frac{\partial \mathrm{T}}{\partial \mathrm{y}}+\mathrm{v}\frac{\partial \mathrm{u}}{\partial \mathrm{y}}\frac{\partial \mathrm{T}}{\partial \mathrm{x}}+2\mathrm{uv}\frac{\partial^2 \mathrm{T}}{\partial \mathrm{x}\partial \mathrm{y}}+\mathrm{u}^2\frac{\partial^2 \mathrm{T}}{\partial x^2}+\mathrm{v}^2\frac{\partial^2 \mathrm{T}}{\partial \mathrm{y}^2}\right)$$
$$+\frac{1}{(\widetilde{\rho}\widetilde{C_p})_{hnf}}\left(\frac{\partial q_r}{\partial \mathrm{y}}\right)=\frac{\widetilde{K}_{hnf}}{(\widetilde{\rho}\widetilde{C_p})_{hnf}}\frac{\partial^2 \mathrm{T}}{\partial \mathrm{y}^2}+\frac{\widetilde{\sigma}_{hnf}}{(\widetilde{\rho}\widetilde{C_p})_{hnf}}(B_0^2\mathrm{u}^2-E_0^2)+\frac{\widetilde{\mu}_{hnf}}{(\widetilde{\rho}\widetilde{C_p})_{hnf}}\frac{\mathrm{u}^2}{k}$$
$$+\frac{\widetilde{\mu}_{hnf}}{(\widetilde{\rho}\widetilde{C_p})_{hnf}}\left(\frac{\partial \mathrm{u}}{\partial \mathrm{y}}\right)^2+\frac{q}{(\widetilde{\rho}\widetilde{C_p})_{hnf}}(\mathrm{T}-\mathrm{T}_\infty)+\tau\left(D_B\frac{\partial \mathrm{C}}{\partial \mathrm{y}}\frac{\partial \mathrm{T}}{\partial \mathrm{x}}+\frac{D_T}{\mathrm{T}_\infty}\left(\frac{\partial \mathrm{T}}{\partial \mathrm{y}}\right)^2\right)$$
$$+\frac{\widetilde{\rho}_{hnf}}{(\widetilde{\rho}\widetilde{C_p})_{hnf}}\frac{\omega}{\sqrt{k}}\mathrm{u}^3. \tag{4.2}$$

4.2.3 Concentration Equation

$$\mathrm{v}\frac{\partial \mathrm{C}}{\partial \mathrm{y}}+\mathrm{u}\frac{\partial \mathrm{C}}{\partial \mathrm{x}}+\lambda_2\left(\mathrm{u}\frac{\partial \mathrm{u}}{\partial \mathrm{v}}\frac{\partial \mathrm{C}}{\partial \mathrm{x}}+\mathrm{v}\frac{\partial \mathrm{v}}{\partial \mathrm{y}}\frac{\partial \mathrm{C}}{\partial \mathrm{y}}+\mathrm{v}\frac{\partial \mathrm{u}}{\partial \mathrm{y}}\frac{\partial \mathrm{C}}{\partial \mathrm{x}}+2\mathrm{uv}\frac{\partial^2 \mathrm{C}}{\partial \mathrm{x}\partial \mathrm{y}}+\mathrm{u}^2\frac{\partial^2 \mathrm{C}}{\partial x^2}+\mathrm{v}^2\frac{\partial^2 \mathrm{C}}{\partial \mathrm{y}^2}\right)$$
$$=D_B\frac{\partial^2 \mathrm{C}}{\partial \mathrm{y}^2}+\frac{D_T}{\mathrm{T}_\infty}\frac{\partial^2 \mathrm{T}}{\partial \mathrm{y}^2}-K_r^2\left(\frac{\mathrm{T}}{T_\infty}\right)^m(\mathrm{C}-\mathrm{C}_\infty)\,exp\left(\frac{-e}{k\mathrm{T}}\right). \tag{4.3}$$

4.3 Non-dimensionalization of Model

To derive the dimensionless formulation, the same similarity transformations introduced in Chapter 3 are adopted.

Through these transformations, the original mathematical relations describing the flow and transport processes are systematically reduced to a coupled system of ordinary differential equations.

4.3.1 Non-dimensionalization of Momentum Equation

Applying the results obtained from (2.6), (2.7), (2.8), (2.10), and (2.11) into the equation (4.1) leads to the following expression:

$$(\psi_1\psi_2\mathrm{x}\,\mathrm{f}')(\psi_1\psi_2\mathrm{f}') + (-\psi_2\mathrm{f})(\psi_1^2\psi_2\mathrm{x}\,\mathrm{f}'') + \frac{\widetilde{\sigma}_{hnf}}{\widetilde{\rho}_{hnf}}(B_0^2\psi_1\psi_2\mathrm{x}\mathrm{f}' - E_0B_0) + \frac{\widetilde{\mu}_{hnf}}{\widetilde{\rho}_{hnf}}\frac{\psi_1\psi_2\mathrm{x}\,\mathrm{f}'}{k} = \frac{\widetilde{\mu}_{hnf}}{\widetilde{\rho}_{hnf}}\psi_1^3\psi_2\mathrm{x}\,\mathrm{f}''' - \frac{\omega}{\sqrt{k}}(\psi_1\psi_2\mathrm{x}\mathrm{f}')^2.$$

$$\Rightarrow \quad \psi_1^2\psi_2^2\mathrm{x}\,\mathrm{f}'^2 - \psi_1^2\psi_2^2\mathrm{x}\,\mathrm{f}\,\mathrm{f}'' + \frac{\widetilde{\sigma}_{hnf}}{\widetilde{\rho}_{hnf}}(B_0^2\psi_1\psi_2\mathrm{x}\mathrm{f}' - E_0B_0) + \frac{\widetilde{\mu}_{hnf}}{\widetilde{\rho}_{hnf}}\frac{\psi_1\psi_2\mathrm{x}\,\mathrm{f}'}{k} = \frac{\widetilde{\mu}_{hnf}}{\widetilde{\rho}_{hnf}}\psi_1^3\psi_2\mathrm{x}\,\mathrm{f}''' - \frac{\omega}{\sqrt{k}}\psi_1^2\psi_2^2\mathrm{x}^2\mathrm{f}'^2.$$

$$\Rightarrow \quad \psi_1^2\psi_2^2\mathrm{x}\,(\mathrm{f}'^2 - \mathrm{f}\,\mathrm{f}'') = \frac{\widetilde{\mu}_{hnf}}{\widetilde{\rho}_{hnf}}\psi_1^3\psi_2\mathrm{x}\,\mathrm{f}''' - \frac{\widetilde{\sigma}_{hnf}}{\widetilde{\rho}_{hnf}}(B_0^2\psi_1\psi_2\mathrm{x}\mathrm{f}' - E_0B_0) - \frac{\widetilde{\mu}_{hnf}}{\widetilde{\rho}_{hnf}}\frac{\psi_1\psi_2\mathrm{x}\,\mathrm{f}'}{k} - \frac{\omega}{\sqrt{k}}\psi_1^2\psi_2^2\mathrm{x}^2\mathrm{f}'^2.$$

$$\Rightarrow \quad \mathrm{f}'^2 - \mathrm{f}\,\mathrm{f}'' = \frac{\widetilde{\mu}_{hnf}}{\widetilde{\rho}_{hnf}}\frac{\psi_1}{\psi_2}\,\mathrm{f}''' - \frac{\widetilde{\sigma}_{hnf}}{\widetilde{\rho}_{hnf}}\frac{B_0^2}{\psi_1\psi_2}\left(\mathrm{f}' - \frac{E_0}{B_0\psi_1\psi_2\mathrm{x}}\right) - \frac{\widetilde{\mu}_{hnf}}{\widetilde{\rho}_{hnf}}\frac{\mathrm{f}'}{\psi_1\psi_2 k} - \frac{\omega}{\sqrt{k}}\mathrm{x}\mathrm{f}'^2.$$

$$\Rightarrow \quad \mathrm{f}'^2 - \mathrm{f}\,\mathrm{f}'' = \frac{\widetilde{\mu}_{hnf}/\widetilde{\mu}_f}{\widetilde{\rho}_{hnf}/\widetilde{\rho}_f}\,\mathrm{f}''' - \frac{\widetilde{\sigma}_{hnf}/\widetilde{\sigma}_f}{\widetilde{\rho}_{hnf}\widetilde{\rho}_f}\frac{\widetilde{\sigma}_f}{\widetilde{\rho}_f}\frac{B_0^2}{\psi_1\psi_2}\left(\mathrm{f}' - \frac{E_0}{B_0\psi_1\psi_2\mathrm{x}}\right) - \frac{\omega}{\sqrt{k}}\mathrm{x}\mathrm{f}'^2 - \frac{\widetilde{\mu}_{hnf}/\widetilde{\mu}_f}{\widetilde{\rho}_{hnf}/\widetilde{\rho}_f}\frac{\widetilde{\mu}_f}{\widetilde{\rho}_f}\frac{\mathrm{f}'}{\psi_1\psi_2 k}.$$

$$\Rightarrow \quad \mathrm{f}'^2 - \mathrm{f}\,\mathrm{f}'' = \frac{P_1}{P_2}\,\mathrm{f}''' - \frac{P_4}{P_2}\,M(\mathrm{f}' - E) - F\mathrm{f}'^2 - \frac{P_1}{P_2}\,K_1\,\mathrm{f}'. \tag{4.4}$$

$$\Rightarrow \quad P_1\,\mathrm{f}''' + P_2\big(\mathrm{f}\,\mathrm{f}'' - \mathrm{f}'^2\big) - P_4\,M(\mathrm{f}' - E) - P_1\,K_1\,\mathrm{f}' - P_2F\mathrm{f}'^2 = 0. \tag{4.5}$$

4.3.2 Non-dimensionalization of Energy Equation

On inserting the expressions from equations (2.6)–(2.10), (2.14)–(2.16), (2.19), (3.5) and (3.6) into (4.2), the resulting equation can be written as:

$$
\begin{aligned}
&2\psi_1\psi_2 b\mathrm{x}^2\,\mathrm{f}'\theta - \psi_1\psi_2 b\mathrm{x}^2 f\theta' + \lambda_1\big[2\psi_1^2\psi_2^2 b\mathrm{x}^2\mathrm{f}'^2\theta + \psi_1^2\psi_2^2 b\mathrm{x}^2\mathrm{f}\,\mathrm{f}'\theta' - \psi_1^2\psi_2^2 b\mathrm{x}^2\mathrm{f}\,\mathrm{f}''\theta \\
&- 4\psi_1^2\psi_2^2 b\mathrm{x}^2\mathrm{f}\,\mathrm{f}'\theta' + 2\psi_1^2\psi_2^2 b\mathrm{x}^2\mathrm{f}'^2\theta + \psi_1^2\psi_2^2 b\mathrm{x}^2\mathrm{f}^2\theta''\big] + \frac{1}{(\widetilde{\rho}\widetilde{C_p})_{hnf}}\frac{16\sigma^*\mathrm{T}_\infty^3}{3k^*} b\mathrm{x}^2\psi_1^2\theta'' \\
&= \frac{\widetilde{K}_{hnf}}{(\widetilde{\rho}\widetilde{C_p})_{hnf}} b\mathrm{x}^2\psi_1^2\theta'' + \frac{\widetilde{\sigma}_{hnf}}{(\widetilde{\rho}\widetilde{C_p})_{hnf}}\left(B_0^2\psi_1^2\psi_2^2\mathrm{x}^2\mathrm{f}'^2 - E_0^2\right) + \frac{\widetilde{\mu}_{hnf}}{(\widetilde{\rho}\widetilde{C_p})_{hnf}}\frac{\psi_1^2\psi_2^2\mathrm{x}^2\mathrm{f}'^2}{k} \\
&+ \frac{q(\mathrm{T}_w - \mathrm{T}_\infty)\theta}{(\widetilde{\rho}\widetilde{C_p})_{hnf}} + \tau\left[D_B\psi_1^2 b\mathrm{x}^2\big(\mathrm{C}_w - \mathrm{C}_\infty\big)\phi'\theta' + \frac{D_T}{\mathrm{T}_\infty} b^2\mathrm{x}^4\psi_1^2\theta'^2\right] \\
&+ \frac{\widetilde{\mu}_{hnf}}{(\widetilde{\rho}\widetilde{C_p})_{hnf}}\psi_1^4\psi_2^2\mathrm{x}^2\mathrm{f}''^2 + \frac{\widetilde{\rho}_{hnf}}{(\widetilde{\rho}\widetilde{C_p})_{hnf}}\frac{\omega}{\sqrt{k}}\psi_1^3\psi_2^3\mathrm{x}^3\mathrm{f}'^3.
\end{aligned}
$$

$$
\begin{aligned}
\Rightarrow\ & 2\mathrm{f}'\theta - f\theta' + \lambda_1\psi_1\psi_2\big[4\mathrm{f}'^2\theta - 3\mathrm{f}\,\mathrm{f}'\theta' - 2\mathrm{f}\,\mathrm{f}''\theta + \mathrm{f}^2\theta''\big] = \frac{\widetilde{K}_{hnf}}{(\widetilde{\rho}\widetilde{C_p})_{hnf}}\frac{\psi_1}{\psi_2}\theta'' \\
&+ \frac{1}{(\widetilde{\rho}\widetilde{C_p})_{hnf}}\frac{16\sigma^*\mathrm{T}_\infty^3}{3k^*}\frac{\psi_1}{\psi_2}\theta'' + \frac{\widetilde{\sigma}_{hnf}}{(\widetilde{\rho}\widetilde{C_p})_{hnf}}\frac{1}{\psi_1\psi_2(T_w - T_\infty)}\left(B_0^2\psi_1^2\psi_2^2\mathrm{x}^2\mathrm{f}'^2 - E_0^2\right) + \\
&\frac{\widetilde{\mu}_{hnf}}{(\widetilde{\rho}\widetilde{C_p})_{hnf}}\frac{\psi_1^2\psi_2^2\mathrm{x}^2\mathrm{f}'^2}{k\psi_1\psi_2(\mathrm{T}_w - \mathrm{T}_\infty)} + \frac{q}{(\widetilde{\rho}\widetilde{C_p})_{hnf}}\frac{\theta}{\psi_1\psi_2} + \tau\left[\frac{D_B\big(\mathrm{C}_w - \mathrm{C}_\infty\big)\psi_1}{\psi_2}\phi'\theta'\right. \\
&\left.+ \frac{D_T}{\mathrm{T}_\infty}\frac{\psi_1}{\psi_2}(\mathrm{T}_w - \mathrm{T}_\infty)\theta'^2\right] + \frac{\widetilde{\mu}_{hnf}}{(\widetilde{\rho}\widetilde{C_p})_{hnf}}\frac{\psi_1^4\psi_2^2\mathrm{x}^2\mathrm{f}''^2}{\psi_1\psi_2(\mathrm{T}_w - \mathrm{T}_\infty)} \\
&+ \frac{\widetilde{\rho}_{hnf}}{(\widetilde{\rho}\widetilde{C_p})_{hnf}}\frac{\omega}{\sqrt{k}}\frac{\psi_1^3\psi_2^3\mathrm{x}^3\mathrm{f}'^3}{\psi_1\psi_2(\mathrm{T}_w - \mathrm{T}_\infty)}.
\end{aligned}
$$

$$
\begin{aligned}
\Rightarrow\ & 2\mathrm{f}'\theta - f\theta' + \delta\big[4\mathrm{f}'^2\theta - 3\mathrm{f}\,\mathrm{f}'\theta' - 2\mathrm{f}\,\mathrm{f}''\theta + \mathrm{f}^2\theta''\big] = \frac{1}{P_5 Pr}\left(P_3 + \frac{4R}{3}\right)\theta'' \\
&+ \frac{P_4}{P_5} M E_c(\mathrm{f}'^2 - E^2) + \frac{P_1}{P_5} E_c(K_1\mathrm{f}'^2 + \mathrm{f}''^2) + \frac{1}{P_5}(Q\theta + P_2 E_c F\mathrm{f}'^3) \\
&+ N_b\,\phi'\theta' + N_t\,\theta'^2.
\end{aligned}
$$

$$
\begin{aligned}
\Rightarrow\ & \frac{1}{P_5 Pr}\left(P_3 + \frac{4R}{3}\right)\theta'' + \frac{P_4}{P_5} M E_c(\mathrm{f}'^2 - E^2) + \frac{P_1}{P_5} E_c(K_1\mathrm{f}'^2 + \mathrm{f}''^2) + N_b\,\phi'\theta' \\
&+ N_t\,\theta'^2 + \frac{1}{P_5}(Q\theta + P_2 E_c F\mathrm{f}'^3) - 2\mathrm{f}'\theta\ + f\theta' - \delta\big[4\mathrm{f}'^2\theta - 3\mathrm{f}\,\mathrm{f}'\theta' - 2\mathrm{f}\,\mathrm{f}''\theta \\
&+ \mathrm{f}^2\theta''\big] = 0. \qquad (4.6)
\end{aligned}
$$

4.3.3 Non-dimensionalization of Concentration Equation

By substituting the partial derivatives given in Eqs. (3.9)–(3.13) into (4.3), the following equation is obtained:

$$
\begin{aligned}
&-\psi_1\psi_2 b\mathrm{x}^2 f\phi' + 2\psi_1\psi_2 b\mathrm{x}^2\,\mathrm{f}'\phi + \lambda_2\big[2\psi_1^2\psi_2^2 b\mathrm{x}^2\mathrm{f}'^2\phi + \psi_1^2\psi_2^2 b\mathrm{x}^2\mathrm{f}\,\mathrm{f}'\phi' - \\
&2\psi_1^2\psi_2^2 b\mathrm{x}^2\mathrm{f}\,\mathrm{f}''\phi - 4\psi_1^2\psi_2^2 b\mathrm{x}^2\mathrm{f}\,\mathrm{f}'\phi' + 2\psi_1^2\psi_2^2 b\mathrm{x}^2\mathrm{f}'^2\phi + \psi_1^2\psi_2^2 b\mathrm{x}^2\mathrm{f}^2\phi''\big] = D_B\psi_1^2 b\mathrm{x}^2\phi'' \\
&+ \frac{D_T}{T_\infty}(T_w - T_\infty)\psi_1^2\theta'' - K_r^2\left(1 + \frac{(T_w - T_\infty)\theta}{T_\infty}\right)^m \phi(C_w - C_\infty) \\
&exp\left(\frac{-e}{k(T_\infty + (T_w - T_\infty)\theta)}\right).
\end{aligned}
$$

$$
\begin{aligned}
\Rightarrow\quad & -f\phi' + 2\mathrm{f}'\phi + \lambda_2\psi_1\psi_2\big[4\mathrm{f}'^2\phi - 3\mathrm{f}\,\mathrm{f}'\phi' - 2\mathrm{f}\,\mathrm{f}''\phi + \mathrm{f}^2\phi''\big] = \frac{D_B\psi_1}{\psi_2}\phi'' \\
&+ \frac{D_T}{T_\infty}\frac{\psi_1(T_w - T_\infty)}{\psi_2(C_w - C_\infty)}\theta'' - \frac{K_r^2(1+\alpha\theta)^m}{\psi_1\psi_2(T_w - T_\infty)}\phi(C_w - C_\infty)exp\left(\frac{-e}{kT_\infty(1+\alpha\theta)}\right).
\end{aligned}
$$

$$
\begin{aligned}
\Rightarrow\quad & -f\phi' + 2\mathrm{f}'\phi + \beta\big[4\mathrm{f}'^2\phi - 3\mathrm{f}\,\mathrm{f}'\phi' - 2\mathrm{f}\,\mathrm{f}''\phi + \mathrm{f}^2\phi''\big] = \frac{D_B}{v_f}\Bigg[\phi'' - \Gamma(1+\alpha\theta)^m \\
&exp\left(\frac{-\varepsilon}{1+\alpha\theta}\right)\frac{v_f}{D_B}\phi + \frac{D_T}{T_\infty D_B}\frac{(T_w - T_\infty)}{(C_w - C_\infty)}\theta''\Bigg].
\end{aligned}
$$

$$
\begin{aligned}
\Rightarrow\quad & -f\phi' + 2\mathrm{f}'\phi + \beta\big[4\mathrm{f}'^2\phi - 3\mathrm{f}\,\mathrm{f}'\phi' - 2\mathrm{f}\,\mathrm{f}''\phi + \mathrm{f}^2\phi''\big] \\
&= \frac{1}{Le}\left(\phi'' + \frac{N_t}{N_b}\theta'' - \Gamma(1+\alpha\theta)exp\left(\frac{-\varepsilon}{1+\alpha\theta}\right)Le\phi\right).
\end{aligned}
$$

$$
\begin{aligned}
\Rightarrow\quad & \phi'' + \frac{N_t}{N_b}\theta'' - \beta Le\Big[4(\mathrm{f}')^2\phi - 3\mathrm{f}\,\mathrm{f}'\phi' - 2\mathrm{f}\,\mathrm{f}''\phi + \mathrm{f}^2\phi''\Big] \\
&- \Gamma Le(1+\alpha\theta)\exp\Big(\frac{-\varepsilon}{1+\alpha\theta}\Big)\phi + Le\,\mathrm{f}\phi' - 2Le\,\mathrm{f}'\phi. \qquad (4.7)
\end{aligned}
$$

The mathematical expressions corresponding to the parameters involved in the above equations are listed below.

$$
F = \frac{\omega \mathrm{x}}{\sqrt{k}}, \quad E = \frac{E_0}{B_0\psi_1\psi_2\mathrm{x}},
$$

$$
\alpha = \frac{\mathrm{T}_w - \mathrm{T}_\infty}{\mathrm{T}_\infty}, \quad \varepsilon = \frac{-e}{k\mathrm{T}_\infty}.
$$

4.4 Solution Framework

A numerical solution of equation (4.5) is obtained via the shooting scheme, for which the following notations are employed.

$$\mathrm{f} = m_1, \quad \mathrm{f}' = m_1' = m_2, \quad \mathrm{f}'' = m_2' = m_3,$$
$$\frac{\partial m_1}{\partial \mathrm{p}} = m_4, \quad \frac{\partial m_2}{\partial \mathrm{p}} = m_5, \quad \frac{\partial m_3}{\partial \mathrm{p}} = m_6.$$

The momentum equation is transformed into first-order ODEs, described below:

$$\left.\begin{aligned} m_1' &= m_2, & m_1(0) &= f_w, \\ m_2' &= m_3, & m_2(0) &= \mathrm{p}, \\ m_3' &= \frac{P_2}{P_1}\left[m_2^2(F+1) - m_1 m_3\right] + \frac{P_4}{P_1} M(m_2 - E) & & \\ &\quad + K_1 m_2, & m_3(0) &= \frac{-2}{P_1} \end{aligned}\right\} \tag{4.8}$$

Implementation of the RK4 scheme depends on assigning a suitable initial guess for the unknown p such that:

$$m_2\big(\eta_\infty, \mathrm{p}\big) = 0.$$

To achieve an improved approximation of p, Newton's iterative technique is utilized. The formulation of iteration process is given below.

$$\mathrm{p}^{(n+1)} = \mathrm{p}^{(n)} - \frac{m_2\big(\eta_\infty, \mathrm{p}^{(n)}\big)}{m_5\big(\eta_\infty, \mathrm{p}\big)}.$$

Differentiating (4.8) with respect to p, a new system of equations is obtained:

$$\left.\begin{aligned} m_4' &= m_5, & m_4(0) &= 0, \\ m_5' &= m_6, & m_5(0) &= 1, \\ m_6' &= \frac{P_2(2m_2 m_5(F+1) - m_1 m_6 - m_4 m_3) + P_4 M m_5}{P_1} & & \\ &\quad + K_1 m_5, & m_6(0) &= 0. \end{aligned}\right\} \tag{4.9}$$

The IVPs mentioned in (4.8) and (4.9) will be solved by using RK4 method. The stopping criteria for the Newton's technique is set as:

$$|m_2\left(\eta_\infty, \mathrm{p}\right)| < \epsilon.$$

While solving coupled equations (4.6) and (4.7) numerically, f, f' and f'' are treated as known functions. The notations employed for the implementation of shooting algorithm, are given below:

$$\begin{aligned}
&\theta = h_1, \quad \theta' = h_2 \quad \phi = h_3, \quad \phi' = h_4,\\
&\frac{\partial h_1}{\partial \mathrm{q}} = h_5, \qquad \frac{\partial h_2}{\partial \mathrm{q}} = h_6, \qquad \frac{\partial h_3}{\partial \mathrm{q}} = h_7, \qquad \frac{\partial h_4}{\partial \mathrm{q}} = h_8,\\
&\frac{\partial h_1}{\partial \tilde{\mathrm{s}}} = h_9, \qquad \frac{\partial h_2}{\partial \tilde{\mathrm{s}}} = h_{10}, \qquad \frac{\partial h_3}{\partial \tilde{\mathrm{s}}} = h_{11}, \qquad \frac{\partial h_4}{\partial \tilde{\mathrm{s}}} = h_{12}.
\end{aligned}$$

and

$$\begin{aligned}
a_3 = &\Bigg[m\alpha h_5(1+\alpha h_1)^{m-1}\exp\left(\frac{-\varepsilon}{1+\alpha h_1}\right)h_3 + \varepsilon\alpha h_5 h_3 \exp\left(\frac{-\varepsilon}{1+\alpha h_1}\right)\\
&(1+\alpha h_1)^{m-2} + (1+\alpha h_1)^m \exp\left(\frac{-\varepsilon}{1+\alpha h_1}\right)h_7\Bigg],\\
a_4 = &\Bigg[m\alpha h_9(1+\alpha h_1)^{m-1}\exp\left(\frac{-\varepsilon}{1+\alpha h_1}\right)h_3 + \varepsilon\alpha h_9 h_3 \exp\left(\frac{-\varepsilon}{1+\alpha h_1}\right)\\
&(1+\alpha h_1)^{m-2} + (1+\alpha h_1)^m \exp\left(\frac{-\varepsilon}{1+\alpha h_1}\right)h_{11}\Bigg],
\end{aligned}$$

$$\begin{aligned}
h_1' &= h_2, && h_1(0) = 1,\\
h_2' &= \frac{-1}{a_1}\Bigg[\frac{1}{P_5}(Qh_1 + E_c F \mathrm{f}'^3) + N_b h_2 h_4 + N_t h_2^2 - 2\mathrm{f}' h_1 + \mathrm{f} h_2\\
&\quad - \delta(4\mathrm{f}'^2\widetilde{z}_1 - 3\mathrm{f}\,\mathrm{f}'\widetilde{z}_2 - 2\mathrm{f}\,\mathrm{f}''\widetilde{z}_1) + \frac{P_1 E_c(K_1\mathrm{f}'^2 + \mathrm{f}'')}{P_5}\\
&\quad + \frac{P_4 M E_c(\mathrm{f}'^2 - E^2)}{P_5}\Bigg], && h_2(0) = \mathrm{q},\\
h_3' &= h_4, && h_3(0) = 1,\\
h_4' &= a_2\Bigg[(\Gamma Le(1+\alpha\theta)^m \exp\Big(\frac{-\varepsilon}{1+\alpha h_1}\Big) + 2Le\mathrm{f}')h_3 - Le\mathrm{f}h_4\\
&\quad - \frac{Nt}{Nb}h_2' + \beta Le(4\mathrm{f}'^2 - 2\mathrm{f}\,\mathrm{f}'')h_3 - 3Le\beta\mathrm{f}\,\mathrm{f}'h_4\Bigg], && h_4(0) = \tilde{\mathrm{s}}.
\end{aligned}$$

Appropriate values of q and $\tilde{\mathrm{s}}$ are identified to achieve convergence of the numerical solution in accordance with the imposed boundary conditions.

$$h_1\big(\eta_\infty, \mathrm{q}, \tilde{\mathrm{s}}\big) = 0, \qquad h_3\big(\eta_\infty, \mathrm{q}, \tilde{\mathrm{s}}\big) = 0.$$

The obtained nonlinear algebraic equations are resolved using Newton's method, written in the following form.

$$\begin{bmatrix} \mathrm{q} \\ \tilde{\mathrm{s}} \end{bmatrix}^{(n+1)} = \begin{bmatrix} \mathrm{q} \\ \tilde{\mathrm{s}} \end{bmatrix}^{(n)} - \left(\begin{bmatrix} h_5 & h_9 \\ h_7 & h_{11} \end{bmatrix}^{-1} \begin{bmatrix} h_1 \\ h_3 \end{bmatrix} \right)^{(n)}. \tag{4.10}$$

Differentiation with respect to q and $\tilde{\mathrm{s}}$ yields another system of ODEs.

$$\begin{aligned}
&h_5' = h_6, && h_5(0) = 0,\\
&h_6' = \frac{-1}{a_1}\Bigg[\frac{Q}{P_5}h_5 + N_b(h_2h_8 + h_6h_4) + 2N_th_2h_6 - 2\mathrm{f}'h_5 + \mathrm{f}h_6\\
&\quad - \delta(4\mathrm{f}'^2h_5 - 3\mathrm{f}\,\mathrm{f}'h_6 - 2\mathrm{f}\,\mathrm{f}''h_5)\Bigg], && h_6(0) = 1,\\
&h_7' = h_8, && h_7(0) = 0,\\
&h_8' = a_2\Bigg[\Gamma Lea_3 + 2Le\mathrm{f}'h_7 - Le\mathrm{f}h_8 - \frac{Nt}{Nb}h_6' + \beta Le(4\mathrm{f}'^2 - 2\mathrm{f}\,\mathrm{f}'')h_7\\
&\quad - 3Le\beta\mathrm{f}\,\mathrm{f}'h_8\Bigg], && h_8(0) = 0,
\end{aligned}$$

$$\begin{aligned}
&h_9' = h_{10}, && h_9(0) = 0,\\
&h_{10}' = \frac{-1}{a_1}\Bigg[\frac{Q}{P_5}h_9 + N_b(h_2h_{12} + h_{10}h_4) + 2N_th_2h_{10} - 2\mathrm{f}'h_9 + \mathrm{f}h_{10}\\
&\quad - \delta(4\mathrm{f}'^2h_9 - 3\mathrm{f}\,\mathrm{f}'h_{10} - 2\mathrm{f}\,\mathrm{f}''h_9)\Bigg], && h_{10}(0) = 0,\\
&h_{11}' = h_{12}, && h_{11}(0) = 0,\\
&h_{12}' = a_2\Bigg[\Gamma Lea_4 + 2Le\mathrm{f}'h_{11} - Le\mathrm{f}h_{12} - \frac{Nt}{Nb}h_{10}' + \beta Le(4\mathrm{f}'^2 - 2\mathrm{f}\,\mathrm{f}'')h_{11}\\
&\quad - 3Le\beta\mathrm{f}\,\mathrm{f}'h_{12}\Bigg], && h_{12}(0) = 1.
\end{aligned}$$

The stopping criteria for Newton's technique are as follows.

$$max\left\{\left|h_1\big(\eta_\infty, \mathrm{q}, \tilde{\mathrm{s}}\big)\right|, \left|h_3\big(\eta_\infty, \mathrm{q}, \tilde{\mathrm{s}}\big)\right|\right\} < \epsilon.$$

4.5 Results and Discussion

An evaluation is carried out to determine how the electric field modifies the flow structure and associated heat and mass transfer behavior. The effects of key governing parameters on momentum, heat and mass transfer are illustrated through graphical results. The corresponding Nusselt and Sherwood numbers are reported in tabular form. These results provide insight into the role of electromagnetic interactions in shaping the flow, thermal and concentration behavior of the system.

4.5.1 Analysis of Computational Results

Table 4.1 summarizes the variation of Nu_x and Sh_x under the combined action of electric and magnetic fields. The applied electric field promotes transport processes within the boundary layer, while the remaining governing parameters regulate the resulting heat and mass transfer behavior.

An increase in the magnetic parameter M leads to a reduction of about 9% in Nu_x, as magnetic damping slows the flow and weakens the temperature gradient at the wall. In contrast, Sh_x rises by nearly 18%, reflecting intensified mass transfer near the surface. Similarly, varying K_1 from 0.3 to 1.0 produces noticeable changes in surface transport characteristics. Greater permeability allows fluid to move more freely through the porous medium, which diminishes near-wall heat transfer and results in an approximate 12.2% decrease in Nu_x. At the same time, the modified flow field promotes stronger concentration transport toward the surface, leading to an increase of nearly 16% in Sh_x.

When Q varies from 0.2 to 1.5, Nu_x experiences nearly a 22% reduction owing to the additional thermal energy introduced within the boundary layer, which diminishes the wall temperature gradient. Correspondingly, Sh_x rises by about 67.7%, since the internal heat generation promotes mass transport near the surface.

When Γ increases from 0.1 to 1, Nu_x decreases by about 13.1%, indicating reduced heat transfer at the surface due to intensified reaction activity within the boundary layer. Over the same range, the Sherwood number Sh_x increases by nearly

91.5%, reflecting stronger mass transfer as reaction effects sharpen concentration gradients near the wall.

A rise in parameter Le, causes the Nu_x to decline by approximately 16%, signifying a reduction in heat transfer effectiveness at the wall. In contrast, Sh_x increases by nearly 51–139%, indicating a substantial enhancement in mass transfer as diffusion-related effects become more dominant in the concentration field.

TABLE 4.1: Variation of Nu_x and Sh_x for $E = 0.02$, $f_w = 0.5$ and $\phi_1, \phi_2 = 0.02$

M	K_1	Pr	R	Q	E_c	N_t	N_b	Γ	Le	Nu_x	Sh_x
0.5	0.5	15	1	0.5	0.5	0.3	0.3	0.1	1	3.60343	-1.14998
0.8										3.39911	-1.01509
1										3.27483	-0.93413
	0.3									3.75195	-1.21524
	0.8									3.40670	-1.06535
	1									3.29035	-1.01630
		10								2.87349	-0.46251
		12								3.18373	-0.75246
		16								3.73420	-1.27490
			1.5							3.15404	-0.72456
			2							2.82848	-0.42076
			2.5							2.57729	-0.18942
				0.2						3.86477	-1.40725
				1						3.16473	-0.70760
				1.5						3.00044	-0.45466
					0					4.18748	-1.71430
					0.3					3.83794	-1.37661
					0.7					3.36772	-0.92216
						0.1				4.27123	0.63587
						0.2				3.91916	-0.35246
						0.4				3.32243	-1.79172
							0.1			4.85961	-10.87451
							0.4			3.08422	-0.01899
							0.5			2.63510	0.61627
								0.5		3.35703	-0.61462
								1		3.13260	-0.09801
								1.5		2.96100	0.31976
									1.2	3.32930	-0.55774
									1.4	3.10114	-0.02803
									1.5	3.00078	0.21818

Tables 4.2 and 4.3 report the computed values of Nu_x and Sh_x for the extended formulation that accounts for the electric field, higher-order chemical reaction and

non-inertial effects. The results illustrate how the inclusion of these additional physical influences alters the thermal and concentration transport behavior at the surface.

A change in the magnetic parameter M from 0.5 to 1.0 causes Nu_x to drop by about 18.7%, whereas Sh_x shows a gain of nearly 26.3% in the extended formulation. Compared with the baseline results reported earlier, these shifts are more pronounced, indicating that the presence of higher-order chemical reaction and non-inertial effects strengthens the role of magnetic damping in shaping both heat and mass transfer behavior. When the parameter Q increases from 0.2 to 1.5, Nu_x decreases in the extended model, indicating that excessive internal heat generation weakens the surface heat transfer rate. In contrast, as Q increases from 0.2 to 0.5, Sh_x shows a marked increase, demonstrating that internal heating strengthens mass transfer by modifying the near-wall concentration distribution. Furthermore, Sh_x continues to increase with higher values of Q. Permeability effects governed by the parameter K_1 significantly influence surface transport characteristics. As K_1 varies from 0.3 to 1.0, Nu_x declines by about 25.2%, indicating weaker heat transfer at the wall due to modified flow penetration within the porous medium. Similarly, Sh_x increases by nearly 40%, showing enhanced mass transfer as fluid penetration strengthens concentration transport near the surface.

As the chemical reaction parameter Γ increases from 0.1 to 1.5, Nu_x decreases, indicating weakened heat transfer at the wall due to stronger reaction activity within the boundary layer, while Sh_x increases, reflecting enhanced mass transfer near the surface. Similarly, variations in the Lewis number Le from 1 to 2.5 lead to a noticeable reduction in Nu_x. In contrast, an increase in Le results in a significant enhancement in Sh_x, emphasizing the dominant influence of diffusion-related effects in augmenting mass transport within the boundary layer.

4.5.2 Velocity Profile

As depicted in Figure 4.2, increasing the parameter M leads to a noticeable decline in the velocity profile. This behavior is caused by the Lorentz force generated

TABLE 4.2: Variation of Nu_x and Sh_x for $E = 0.02$, $F = 0.2$, $f_w = 0.5$, $\phi_1 = \phi_2 = 0.02$, $\varepsilon = -0.4$, $\alpha = 0.8$ and $m = 0.6$

M	K_1	Pr	R	Q	E_c	N_t	N_b	Γ	Le	Nu_x	Sh_x
0.5	0.5	15	1	0.5	0.5	0.3	0.3	0.1	1	1.63065	0.62629
0.8										1.43943	0.73020
1										1.32550	0.79106
	0.3									1.77428	0.55372
	0.8									1.44001	0.72063
	1									1.32714	0.77531
		10								1.42634	0.79315
		17								1.68615	0.58108
		19								1.73119	0.54475
			1.5							1.51341	0.72218
			2							1.41133	0.80534
			2.5							1.32202	0.87751
				0.2						2.00503	0.26554
				1						0.90078	1.32680
				1.5						0.15577	2.06229
					0					4.15673	-1.81653
					0.3					2.65725	0.36695
					0.7					0.58201	1.64153
						0.1				2.07798	1.25356
						0.2				1.84157	0.87806
						0.4				1.44353	0.47448
							0.2			2.06355	-0.58095
							0.4			1.26154	1.18084
							0.5			0.95331	1.47628
								0.5		1.42562	1.7107
								1		1.26517	1.64783
								1.5		1.14998	2.02626
									1.5	1.23214	1.78785
									2	0.99608	2.70236
									2.5	0.83849	3.50375

by the magnetic field, which opposes the fluid motion. The applied electric field further enhances this opposing effect, while the Forchheimer resistance associated with the porous medium introduces additional drag, collectively reducing the flow velocity.

TABLE 4.3: Variation of Nu_x and Sh_x for $M = K_1 = f_w = Q = E_c = 0.5$, $Pr = 15$, $R = 1$, $N_t = N_b = 0.3$, $\Gamma = 0.1$ and $Le = 1$.

E	F	α	ε	Nu_x	Sh_x
0.02	0.2	-0.4	0.8	1.63065	0.62629
0.04				1.64057	0.63664
0.06				1.65257	0.64476
0.08				1.66608	0.65117
	0.4			1.53128	0.69009
	0.6			1.44217	0.74647
	0.8			1.36171	0.79664
		-0.3		1.62634	0.63674
		-0.2		1.62169	0.64801
		-0.1		1.61667	0.66018
			0.3	1.61986	0.64925
			0.5	1.61855	0.65375
			1	1.61545	0.66429

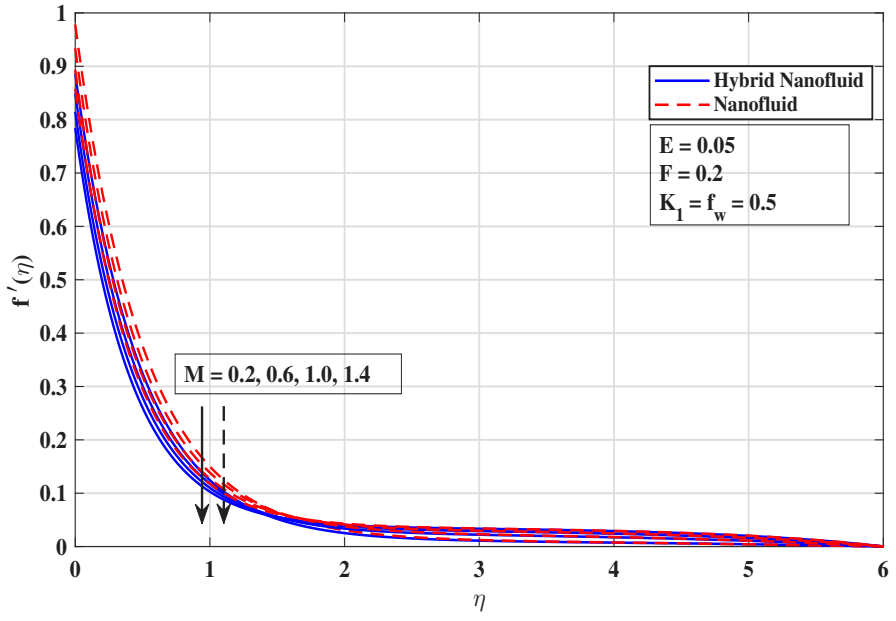

FIGURE 4.2: Influence of M on the velocity f'

The velocity profile decreases as the Forchheimer parameter F rises due to stronger resistance offered by the porous medium. This additional inertial drag slows down the fluid motion away from the surface. The hybrid nanofluid exhibits slightly lower velocities compared to the nanofluid because the presence of multiple nanoparticles enhances flow resistance. This variation is depicted in Figure 4.3.

Figure 4.4 shows that higher values of K_1 lead to a reduction in velocity because the porous medium offers greater resistance to the flow.

The hybrid nanofluid experiences a more noticeable decline than the nanofluid, indicating stronger drag effects due to the combined nanoparticle suspension under the applied electric field.

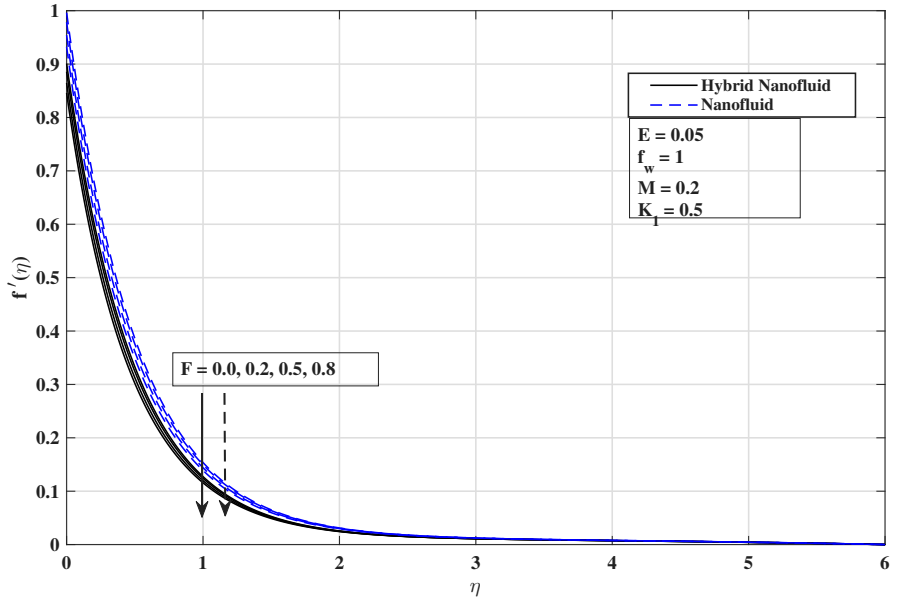

FIGURE 4.3: Influence of F on the velocity f'

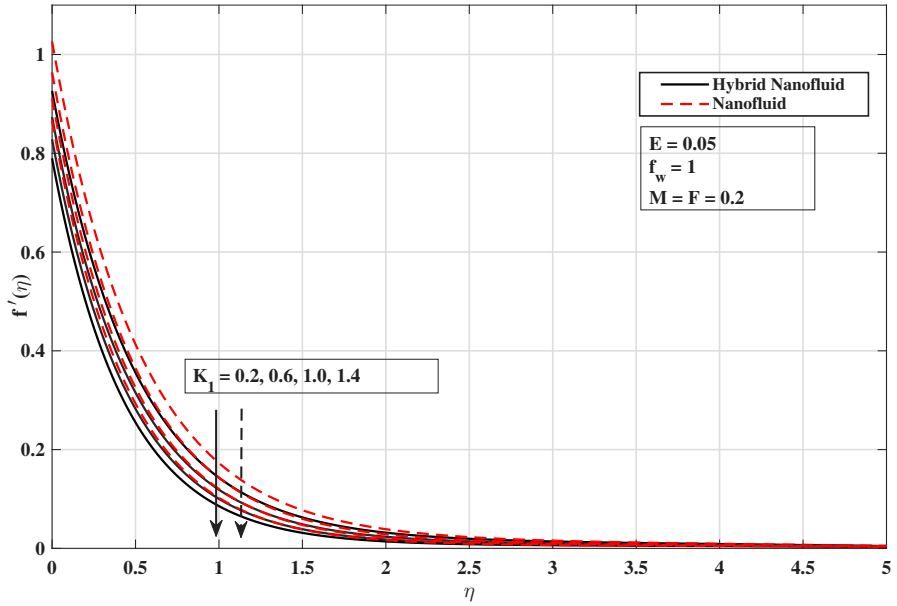

FIGURE 4.4: Influence of K_1 on the velocity f'

The velocity profiles show a progressive enhancement with stronger electric field influence due to the dominance of electrohydrodynamic body forces that accelerate the fluid motion. This electric force helps the fluid move more easily by weakening the effects of viscosity, magnetic resistance and drag caused by the porous medium. The hybrid nanofluid moves faster than the nanofluid because it conducts electricity better and transfers motion more effectively, which can be seen in the Figure 4.5. The velocity profiles are governed by the parameter f_w, which restricts momentum movement away from the surface and weakens the flow near the wall. The hybrid nanofluid loses velocity more rapidly than the nanofluid due to stronger particle interactions, as shown in the Figure 4.6.

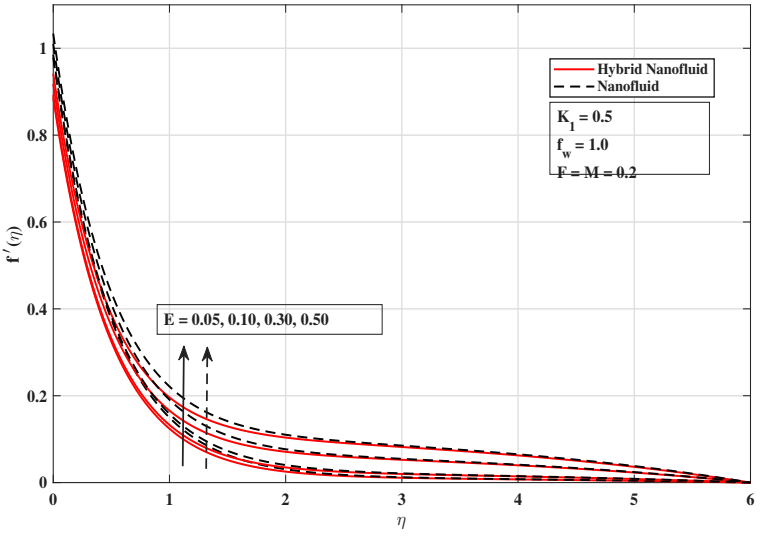

FIGURE 4.5: Influence of E on the velocity f'

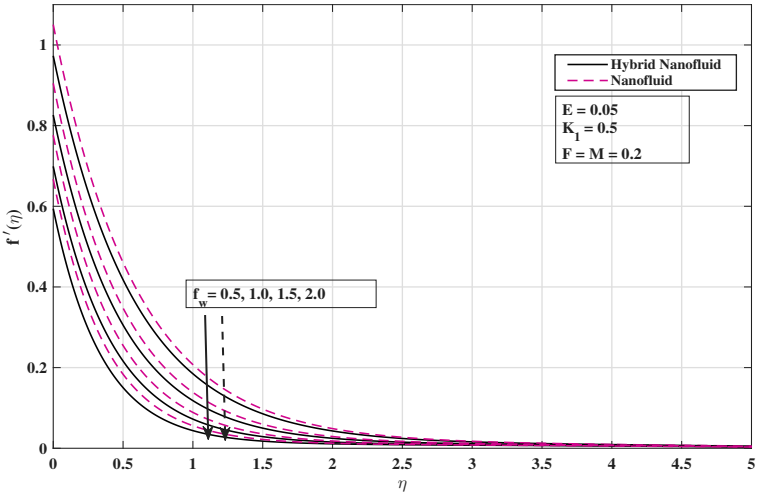

FIGURE 4.6: Influence of f_w on the velocity f'

4.5.3 Temperature Profile

The temperature profiles are affected by the electric field parameter E which makes the fluid move faster and carry heat away from the surface more effectively.

This improves heat transfer and causes the warm layer near the wall to become thinner, leading to lower temperatures close to the surface. Hence, the temperature profile settles to the ambient value more quickly away from the surface, as shown in Figure 4.7.

The temperature profiles are strongly influenced by the internal heat generation parameter Q, where larger values of Q add thermal energy within the fluid domain.

This additional heat raises the temperature inside the boundary layer and thickens the thermal region near the surface. Consequently, the fluid retains heat over a longer distance from the wall, as demonstrated in Figure 4.8.

As illustrated in Figure 4.9, larger values of N_t intensify the movement of heated nanoparticles from the wall toward cooler regions, which redistributes thermal energy within the boundary layer. Even under electric and magnetic effects, this process enhances the temperature field and broadens the thermal region.

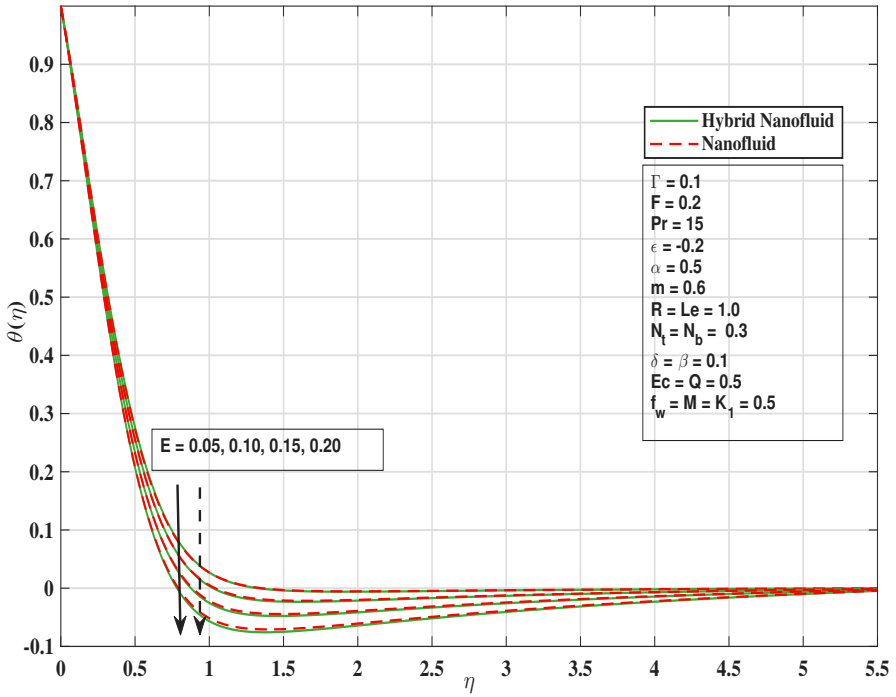

FIGURE 4.7: Impact of E on θ

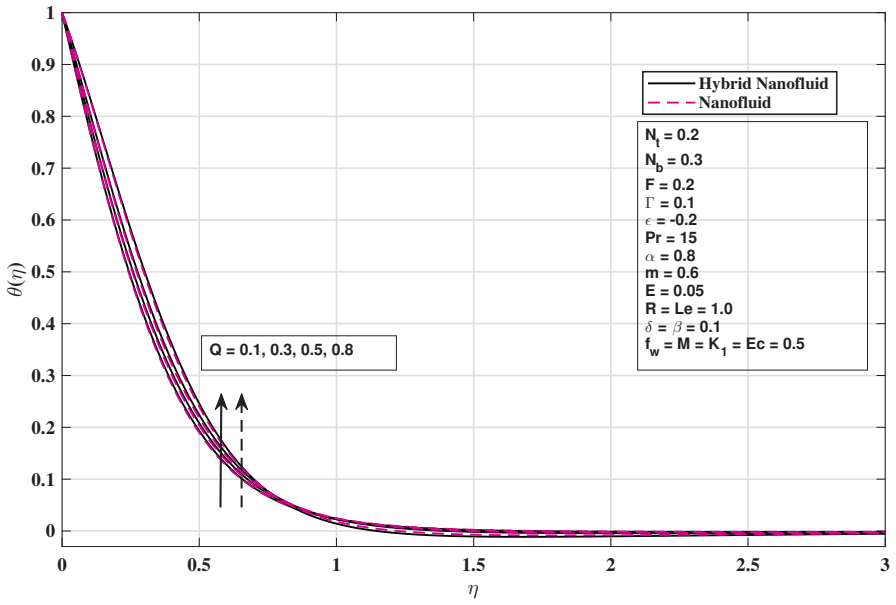

FIGURE 4.8: Impact of Q on θ

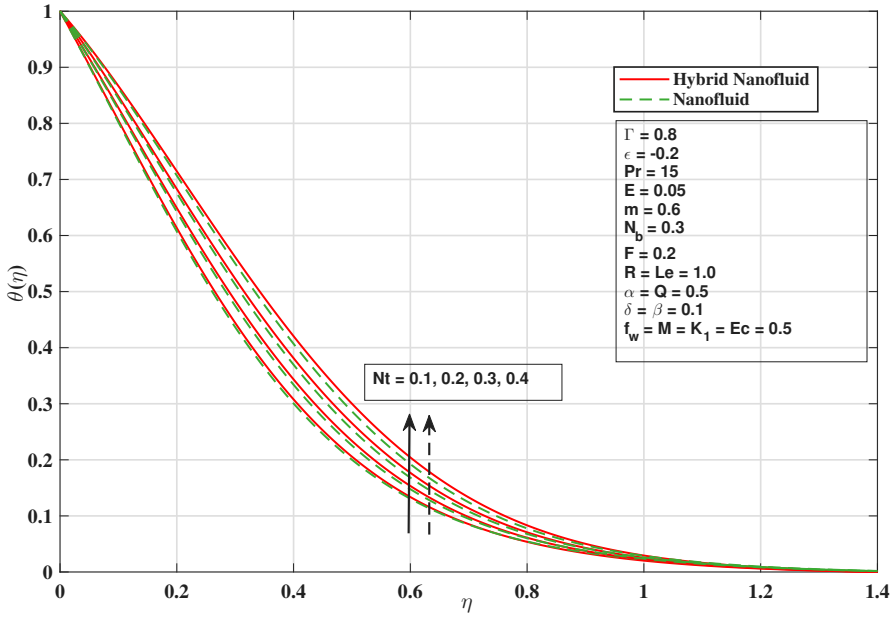

FIGURE 4.9: Impact of N_t on θ

Figure 4.10 shows that elevated values of N_b enhance the microscopic particle diffusion, allowing thermal energy to spread more effectively throughout the boundary layer. Under the influence of electric and magnetic fields, this diffusion mechanism strengthens the temperature field and extends the thermal region.

As E_c increases, thermal energy produced by the flow becomes more prominent, causing the temperature to spread farther away from the surface. This widens the

thermal boundary layer. The added heat within the flow causes the temperature to decay more slowly away from the wall, as reflected by Figure 4.11.

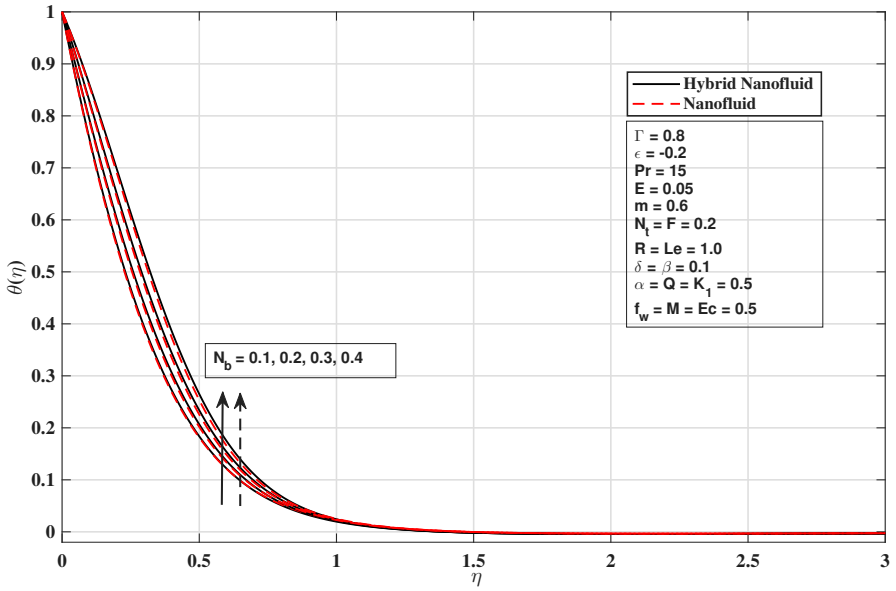

FIGURE 4.10: Impact of N_b on θ

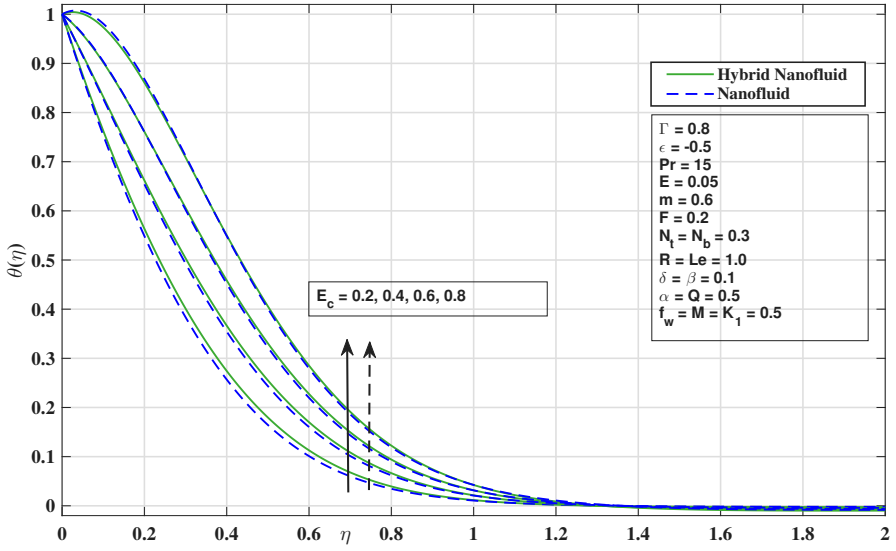

FIGURE 4.11: Impact of E_c on θ

4.5.4 Concentration Profile

Increasing the value of Γ intensifies the higher-order reaction, which consumes more of the diffusing component and reduces ϕ. A dominant chemical reaction

restricts diffusion away from the surface, leading to a thinner concentration boundary layer. This behavior is clearly seen in Figure 4.12.

The concentration profiles respond noticeably to changes in the Lewis number. A rise in values of Le limits the spread of mass within the boundary layer, leading to a faster decay of concentration away from the wall. This behavior results in a compressed concentration region, as depicted in Figure 4.13.

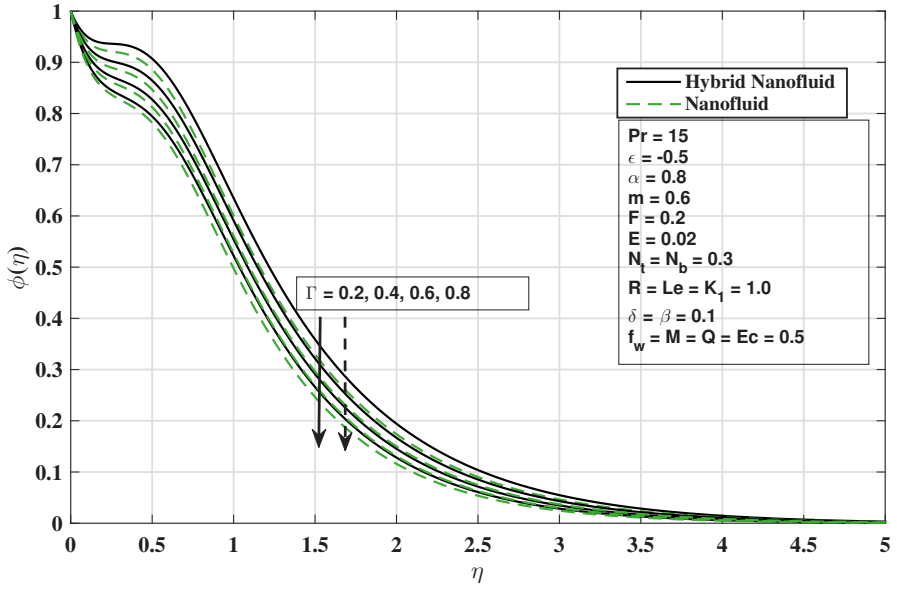

FIGURE 4.12: Impact of Γ on ϕ

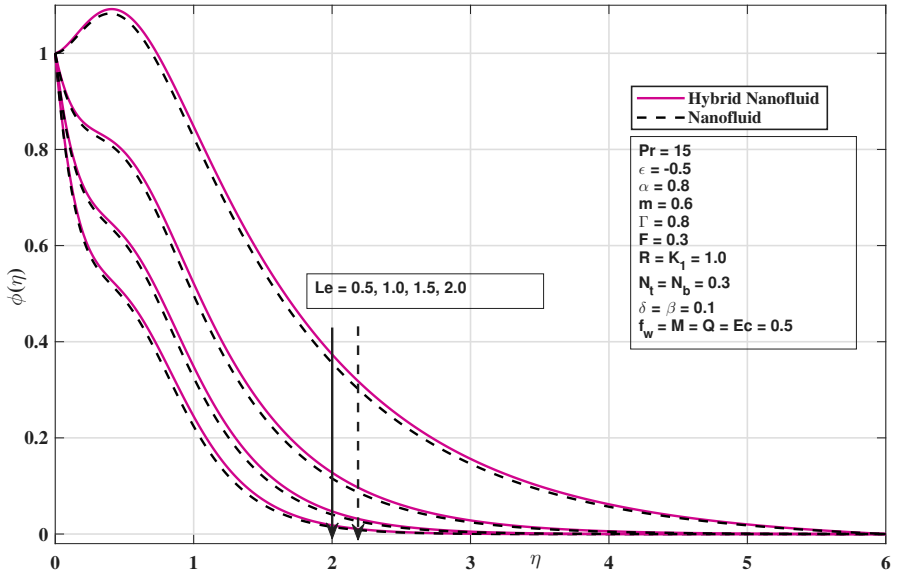

FIGURE 4.13: Impact of Le on ϕ

Figure 4.14 demonstrates that increasing the temperature difference parameter α corresponds to a hotter wall relative to the surrounding fluid. This supplies additional heat to the fluid near the surface, allowing the temperature to remain significant over a longer distance from the wall. Consequently, the thermal boundary layer becomes thicker.

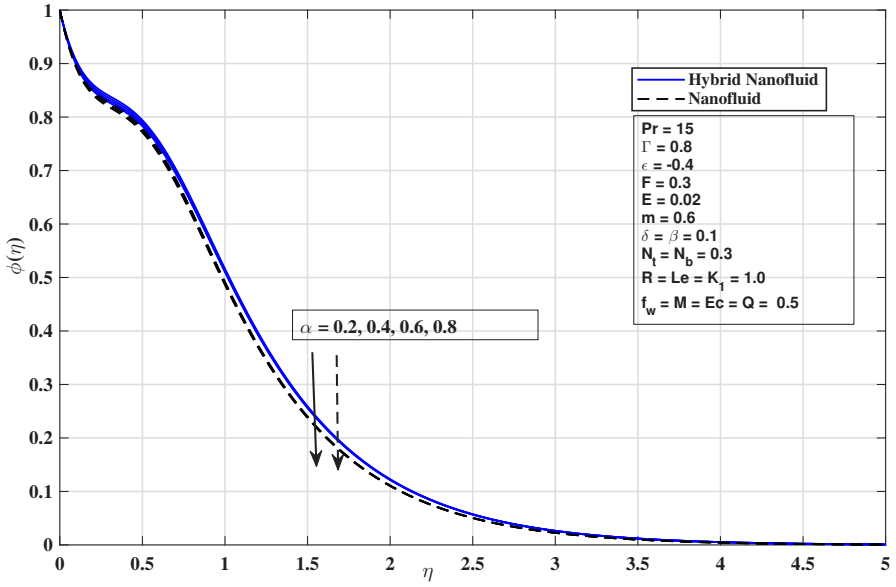

FIGURE 4.14: Impact of α on ϕ

It is evident from Figure 4.15 that how the activation energy parameter affects the concentration field. When ε is higher, the chemical reaction needs more energy to proceed, so the reaction becomes weaker. This slows the consumption of the diffusing component and allows higher concentration levels to persist within the boundary layer. Consequently, the concentration profile exhibits a more gradual decay away from the surface, as shown in the figure.

Figure 4.16 presents the response of ϕ to variations in N_t. An increase in N_t promotes particle migration along the temperature gradient away from the surface, which enhances mass transport within the boundary layer. As a result, the concentration persists over a larger distance from the wall, leading to a thicker concentration boundary layer.

Figure 4.17 highlights the role of N_t in shaping the concentration profile. With

stronger Brownian activity, particle interactions within the fluid become more active, which redistributes the concentration throughout the boundary layer. This redistribution allows the concentration to remain significant farther from the surface, leading to an expanded concentration layer, as seen in the figure.

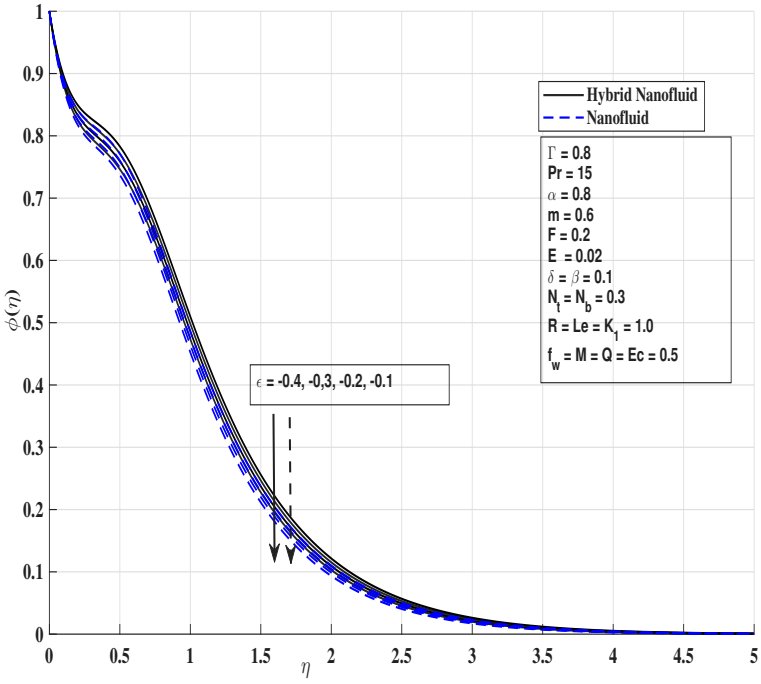

FIGURE 4.15: Impact of ε on θ

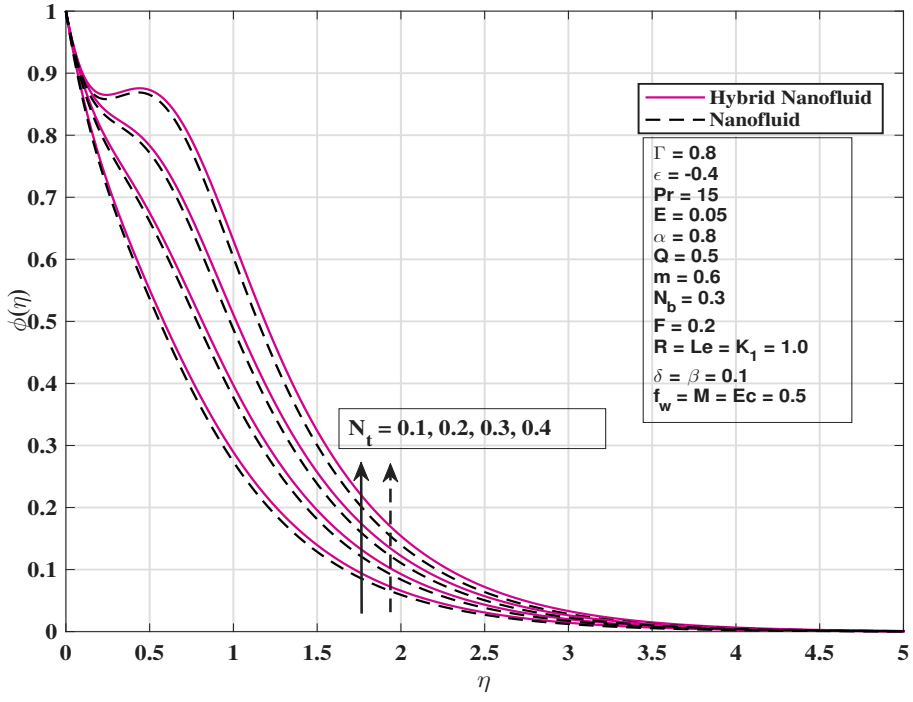

FIGURE 4.16: Impact of N_t on θ

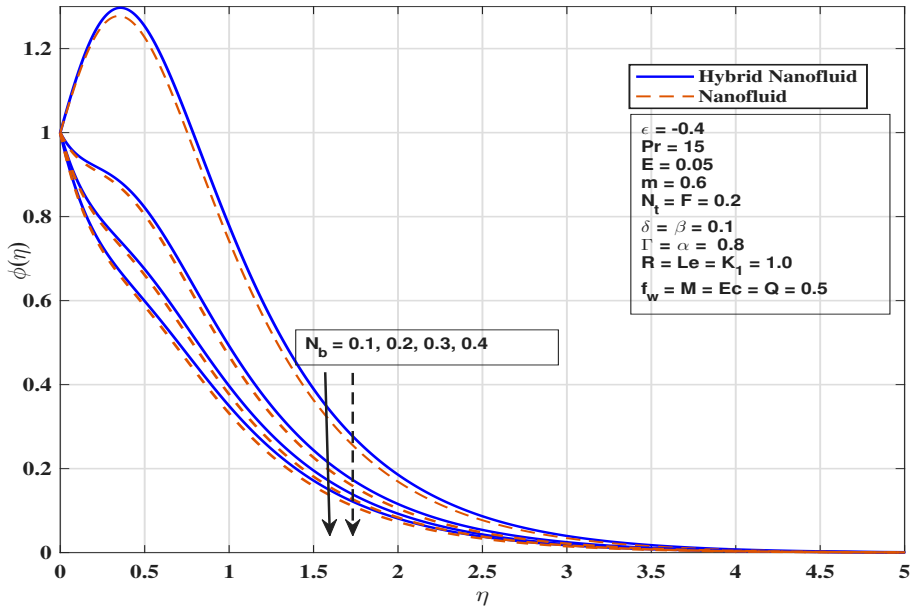

FIGURE 4.17: Impact of N_b on ϕ

Chapter 5

Conclusion

This study systematically examines the transport characteristics of Al_2O_3 nanofluid and Cu–Al_2O_3 hybrid nanofluid through three distinct computational cases. In Case 1, the flow behavior is analyzed under the influence of a magnetic field alone to establish baseline characteristics of velocity, temperature, and concentration distributions.

In Case 2, the analysis is extended to include the combined effects of electric and magnetic fields, allowing a clear assessment of electromagnetic influences on heat and mass transfer.

In Case 3, the model is further enriched by incorporating higher-order chemical reaction and non-Darcy–Forchheimer porous medium effects in the presence of an electric field, providing deeper insight into their impact on transport phenomena. This structured approach enables a comprehensive understanding of the underlying physical mechanisms governing the flow.

5.1 Case 1

i. Increasing the magnetic parameter to 25–60% results in a 3–5.5% reduction in Nu_x and an approximately 5–7% increase in Sh_x, due to magnetic damping effects near the wall.

ii. Varying the chemical reaction parameter Γ reduces Nu_x by 18.9% while increasing Sh_x by about 46–81%, indicating weakened surface heat transfer and enhanced mass transfer.

iii. Higher Prandtl number values suppress heat diffusion within the fluid, leading to a thinner thermal boundary layer and lower temperature distribution across the flow region.

iv. An increase in the Lewis number restricts mass diffusion, resulting in a reduced concentration profile and limited nanoparticle dispersion within the boundary layer for both fluids.

v. Internal heat generation maintains elevated temperature levels within the flow region, producing a thicker thermal boundary layer and a more gradual temperature decay away from the surface.

5.2 Case 2

i. The magnetic parameter M causes about a 9% decrease in Nu_x by weakening the wall temperature gradient through magnetic damping of the electrically driven flow, while Sh_x increases by nearly 18% due to enhanced mass transfer near the surface.

ii. The permeability parameter K_1 results in an approximate 12.2% reduction in Nu_x as near-wall heat transfer weakens, whereas Sh_x rises by about 16% because improved fluid penetration strengthens concentration transport.

iii. An increase in the chemical reaction parameter Γ weakens surface heat transfer by reducing thermal exchange near the wall, while mass transfer is enhanced due to steeper concentration gradients within the boundary layer.

iv. A higher Lewis number limits mass diffusion relative to thermal transport, suppressing heat transfer at the surface while intensifying concentration transport through diffusion-dominated mechanisms.

5.3 Case 3

i. Enhanced non-inertial resistance within the porous medium restricts fluid motion, resulting in a reduced velocity profile throughout the boundary layer.

ii. The inclusion of higher-order chemical reaction intensifies concentration gradients within the boundary layer, thereby enhancing mass transport responses across various physical parameters.

iii. An increase in activation energy parameter ε weakens the chemical reaction rate, allowing the concentration profile to persist farther into the boundary layer.

iv. A larger temperature difference parameter α strengthens wall heating, leading to elevated temperature levels and a thicker thermal boundary layer.

v. Thermophoresis (N_t) and Brownian motion (N_b) promote nanoparticle transport within the boundary layer, enhancing thermal energy redistribution and expanding the thermal region.

vi. Non-inertial resistance amplifies the influence of permeability, contributing to reduced heat transfer and enhanced mass transfer due to modified fluid motion within the porous medium.

Bibliography

[1] T. L. Bergman, A. S. Lavine, F. P. Incropera, and D. P. DeWitt, *Fundamentals of Heat and Mass Transfer*. Hoboken, NJ: John Wiley & Sons, 7 ed., 2011.

[2] J. Buongiorno, "Convective transport in nanofluids," *Journal of Heat Transfer*, vol. 128, no. 3, pp. 240–250, 2006.

[3] J. A. Eastman, S. U. S. Choi, S. Li, L. J. Thompson, and S. Lee, "Enhanced thermal conductivity through the development of nanofluids," in *MRS Online Proceedings Library (OPL)*, vol. 457, p. 3, 1996.

[4] Y. Xuan and Q. Li, "Heat transfer enhancement of nanofluids," *International Journal of Heat and Fluid Flow*, vol. 21, no. 1, pp. 58–64, 2000.

[5] T. Hayat, M. Qasim, and S. Mesloub, "MHD flow and heat transfer over permeable stretching sheet with slip conditions," *International Journal for Numerical Methods in Fluids*, vol. 66, no. 8, pp. 963–975, 2011.

[6] M. E. Karim, M. A. Alim, and M. S. Khan, "Numerical analysis of heat transfer and fluid flow over a permeable stretching surface," *Procedia Engineering*, vol. 56, pp. 547–553, 2013.

[7] S. Suresh, K. P. Venkitaraj, P. Selvakumar, and M. Chandrasekar, "Effect of Al_2O_3–Cu hybrid nanofluid in heat transfer," *Experimental Thermal and Fluid Science*, vol. 38, pp. 54–60, 2012.

[8] S. S. U. Devi and S. A. Devi, "Numerical investigation of hydromagnetic hybrid nanofluid flow," *Alexandria Engineering Journal*, vol. 55, pp. 1307–1316, 2016.

[9] T. Hayat, A. Razaq, S. A. Khan, and A. Alsaedi, "An induced magnetic field utilization for hybrid nanoliquid flow subject to entropy generation," *Journal of Magnetism and Magnetic Materials*, vol. 576, p. 170742, 2023.

[10] K. U. Rahman, Z. Mahmood, S. U. Khan, A. Ali, Z. Li, and I. E. A. Tili, "Enhanced thermal study in hybrid nanofluid flow in a channel motivated by graphene/Fe_3O_4 and Newtonian heating," *Results in Engineering*, vol. 21, p. 101772, 2024.

[11] A. Jan, M. Mushtaq, and M. Hussain, "Heat transfer enhancement of forced convection magnetized cross model ternary hybrid nanofluid flow over a stretching cylinder: non-similar analysis," *International Journal of Heat and Fluid Flow*, vol. 106, p. 109302, 2024.

[12] B. Singh and S. Sood, "Hybrid nanofluids preparation, thermo-physical properties, and applications: A review," *Hybrid Advances*, p. 100192, 2024.

[13] D. M. Christopher and B. X. Wang, "Prandtl number effects for Marangoni convection over a flat surface," *International Journal of Thermal Sciences*, vol. 40, pp. 564–570, 2001.

[14] E. Magyari and A. J. Chamkha, "Exact analytical results for the thermosolutal MHD Marangoni boundary layers," *International Journal of Thermal Sciences*, vol. 47, pp. 848–857, 2008.

[15] Q. M. Al-Mdallal, N. Al-Din, B. Ganga, and A. A. Hakeem, "Marangoni radiative effects of hybrid nanofluids flow past a permeable surface with inclined magnetic field," *Case Studies in Thermal Engineering*, vol. 17, p. 100571, 2019.

[16] E. H. Aly and A. Ebaid, "Exact analysis of the effect of heat transfer on MHD and radiation Marangoni boundary layer nanofluid flow past a surface embedded in a porous medium," *Journal of Molecular Liquids*, vol. 215, pp. 625–632, 2016.

[17] G. Kalpana, K. R. Madhura, and S. S. Iyengar, "Numerical computation on Marangoni convective flow of two-phase MHD dusty nanofluids under Brownian motion and thermophoresis effects," *Heat Transfer–Asian Research*, vol. 49, no. 1, pp. 626–650, 2020.

[18] E. E. Michaelides, "Brownian movement and thermophoresis of nanoparticles in liquids," *International Journal of Heat and Mass Transfer*, vol. 81, pp. 179–187, 2015.

[19] Z. Sabir, A. Ayub, J. L. G. Guirao, S. Bhatti, and S. Z. H. Shah, "The effects of activation energy and thermophoretic diffusion of nanoparticles on steady micropolar fluid along with Brownian motion," *Advances in Materials Science and Engineering*, vol. 2020, no. 1, p. 2010568, 2020.

[20] J. A. Khan, M. Mustafa, T. Hayat, and A. Alsaedi, "Numerical study of Cattaneo–Christov heat flux model for viscoelastic flow due to an exponentially stretching surface," *PLOS ONE*, vol. 10, no. 9, p. e0137363, 2015.

[21] K. A. M. Alharbi, M. N. Alshahrani, N. Ullah, N. M. Khan, M. Krawczuk, A. A. A. Mousa, and S. Ali, "Cattaneo–Christov heat flow model for copper–water nanofluid heat transfer under Marangoni convection and slip conditions," *Scientific Reports*, vol. 12, p. 5360, 2022.

[22] A. Salmi, H. A. Madkhali, B. Ali, M. Nawaz, S. O. Alharbi, and A. Alqahtani, "Numerical study of heat and mass transfer enhancement in Prandtl fluid MHD flow using Cattaneo–Christov heat flux theory," *Case Studies in Thermal Engineering*, vol. 33, p. 101949, 2022.

[23] K. Muhammad, T. Hayat, S. Momani, and S. Asghar, "FDM analysis for squeezed flow of hybrid nanofluid in presence of Cattaneo–Christov heat flux

and convective boundary condition," *Alexandria Engineering Journal*, vol. 61, no. 6, pp. 4719–4727, 2022.

[24] H. Waqas, U. Farooq, D. Liu, M. Imran, T. Muhammad, A. S. Alshomrani, and M. Umar, "Comparative analysis of hybrid nanofluids with Cattaneo–Christov heat flux model," *Case Studies in Thermal Engineering*, vol. 36, p. 102212, 2022.

[25] S. Khattak, M. Ahmed, M. N. Abrar, S. Uddin, M. Sagheer, and M. F. Javeed, "Numerical simulation of Cattaneo–Christov heat flux model in a porous media past a stretching sheet," *Waves in Random and Complex Media*, vol. 35, no. 1, pp. 1230–1249, 2025.

[26] Z. Hussain, S. Muhammad, and M. S. Anwar, "Effects of first-order chemical reaction and melting heat on hybrid nanoliquid flow over a nonlinear stretched curved surface with shape factors," *Journal of Thermal Analysis and Calorimetry*, 2022.

[27] N. K. Mishra, S. Anwar, P. Kumar, T. Seangwattana, M. Bilal, and A. Saeed, "Numerical investigation of chemically reacting jet flow of hybrid nanofluid under the significances of bio-active mixers and chemical reaction," *Results in Physics*, vol. 49, p. e17678, 2023.

[28] M. Qayyum, S. Afzal, S. T. Saeed, A. Akgül, and M. B. Riaz, "Unsteady hybrid nanofluid (Cu–UO_2/blood) with chemical reaction and non-linear thermal radiation through convective boundaries: An application to biomedicine," *Results in Physics*, vol. 48, p. e16578, 2023.

[29] M. Imran Asjad, N. Sarwar, B. Ali, S. Hussain, T. Sitthiwirattam, and J. Reunsumrit, "Impact of bioconvection and chemical reaction on MHD nanofluid flow due to exponential stretching sheet," *Symmetry*, vol. 13, no. 12, p. 2334, 2021.

[30] D. Kumar, P. Agrawal, P. K. Dadheech, and Q. Al-Mdallal, "Numerical study of Marangoni convective hybrid-nanofluids flow over a permeable stretching surface," *International Journal of Thermofluids*, vol. 23, p. 100750, 2024.

[31] S. Kumar, S. Choudhary, K. Kumari, A. Sharma, and P. Choudhary, "MHD Darcy–Forchheimer flow of SWCNT-H_2O nanofluid over a porous stretching sheet," *International Journal of Thermofluids*, vol. 26, p. 101064, 03 2025.

[32] M. Jawad, Z. Khan, E. Bonyah, and R. Jan, "Analysis of hybrid nanofluid stagnation point flow over a stretching surface with melting heat transfer," *Mathematical Problems in Engineering*, vol. 2022, 02 2022.